SCUOLA INTERNAZIONALE SUPERIORE DI STUDI AVANZATI

Particles acceleration with Magnetic Reconnection in large scale MHD simulations

Author:

MATTEO NURISSO

Supervisor:

PROF. ANNALISA CELOTTI
PROF. ANDREA MIGNONE

A thesis submitted in fulfillment of the requirements
for the degree of Philosophiæ Doctor in
ASTROPHYSICS & COSMOLOGY

December 2022

Contents

Abstract

Magnetic reconnection is a physical process in which a region with magnetic field lines of opposite directions rearranges its topology into a lower energy configuration. The process results in the conversion of the released energy to thermal and kinetic plasma energy, with the development of non-thermal spectra of accelerated particles, with possible important consequences for the emission processes from astrophysical environments with high values of the magnetic field.

The work presented in the thesis aims at developing a method to address the multi-scale problem of magnetic reconnection in large-scale relativistic magnetohydrodynamic numerical simulations. A sub-grid model based on prescriptions from simulations of the phenomenon at the kinetic level is presented.

I present a new algorithm for the identification and physical characterization of magnetic reconnection sites in 2D and 3D large scale relativistic magnetohydrodynamic numerical simulations. This has been implemented in the PLUTO code and tested in the cases of a single steady current sheet, a 2D jet and a 3D unstable plasma column. Its main features are: a) a computational demand which allows its use in large scale simulations; b) the capability to deal with complex 2D and 3D structures of the reconnection sites. In the performed simulations the algorithm identifies the computational cells that are part of a current sheet by a measure of the gradient of the magnetic field along different directions. Lagrangian particles, ensemble of real particles which follow the fluid and are described by their collective spectrum, are used to sample plasma parameters before they enter the reconnection sites that form during the evolution of the different configurations considered. Specifically, I perform an analysis of the distributions of the values of the magnetization σ and the thermal to magnetic pressure ratio β that according to particle-in-cell simulations control the properties of particles acceleration in magnetic reconnection regions. Despite the initial conditions of the simulations were not chosen "ad hoc", the 3D simulation returns results suitable for efficient particles acceleration to non-thermal particles distributions.

Subsequently I present a new algorithm for the spectra update of the Lagrangian particles that are found in a current sheet. The σ and β values sampled with the method previously described are used to characterize the final spectrum. Two different strategies for the spectra update are introduced. First a simple method that considers the energy of old spectra, the energy due to MR and update the spectra to the power-law predicted by the sub-grid model is presented. A more refined method,

able to consider additionally also the slope of the old spectra and the presence of multiples Lagrangian particles in the same computational cell, is introduced. I performed simulations of the 3D unstable plasma column with the second method, and I studied the distributions of the various quantities necessary to determine the post magnetic reconnection spectra: available energy and maximum energy. Then I focused on the temporal evolution of individual spectra, exploiting the full possibilities of the sub-grid model of following with time and spatial resolution the consequences on non-thermal particles of magnetic reconnection.

List of publications

The following thesis is the result of the scientific research that I carried out as a Ph.D. student in the Astrophysics & Cosmology Ph.D. course at SISSA, Trieste (Italy), under the supervision of Prof. Annalisa Celotti and Prof. Andrea Mignone (University of Turin), in collaboration with Gianluigi Bodo (INAF Turin) and with several people from SISSA as well as other different institutions. In particular, this thesis is based upon the following publications:

- M. Nurisso, A. Celotti, A. Mignone, G. Bodo
  Particles acceleration with Magnetic Reconnection in large scale MHD simulations: I. Current sheet identification and characterization
  Revised version submitted to MNRAS,

- M. Nurisso, A. Celotti, A. Mignone, G. Bodo
  Particles acceleration with Magnetic Reconnection in large scale MHD simulations: II. Spectra Update
  To be submitted to MNRAS,

List of Figures

1

Introduction

1.1 A background to motivate this work

1.1.1 Cosmic Rays

Cosmic rays (CRs) are defined as the radiation coming from outside the Earth's atmosphere. CRs are composed by ionized nuclei, about 90% of the observed flux is composed by protons, 9% of them are alpha particles and the rest are heavy nuclei. Electrons are also presents and they constitute $\sim 1\%$ of the cosmic radiation. They were discovered in 1909 and for long time they were thought to be originated from the radioactivity of the Earth. Only years later it was possible to establish their origin with experiments firstly from Victor Hess (Hess 1912) and then from Werner Kolhörster.

The CRs are nowadays observed with both ground (Atkins et al. 2004; Aharonian et al. 2007b; Archer et al. 2018; Abeysekara et al. 2019) and space (Adriani et al. 2011; Aguilar et al. 2015; Abdollahi et al. 2017; Aguilar et al. 2019) experiments. The observed flux extends for many orders of magnitude in energy from a few undreds of MeV to above 10^{20} eV, as shown in Fig. 1.1. The number flux can be described at first order by a power-law of index p:

$$\frac{dN}{dE} \propto E^{-p} \ .\tag{1.1}$$

The estimated mean value for the index p is $p \simeq 2.7$. If investigated in detail more features characterize the number flux. At low energies, for $E \lesssim 10^9$ eV, the number
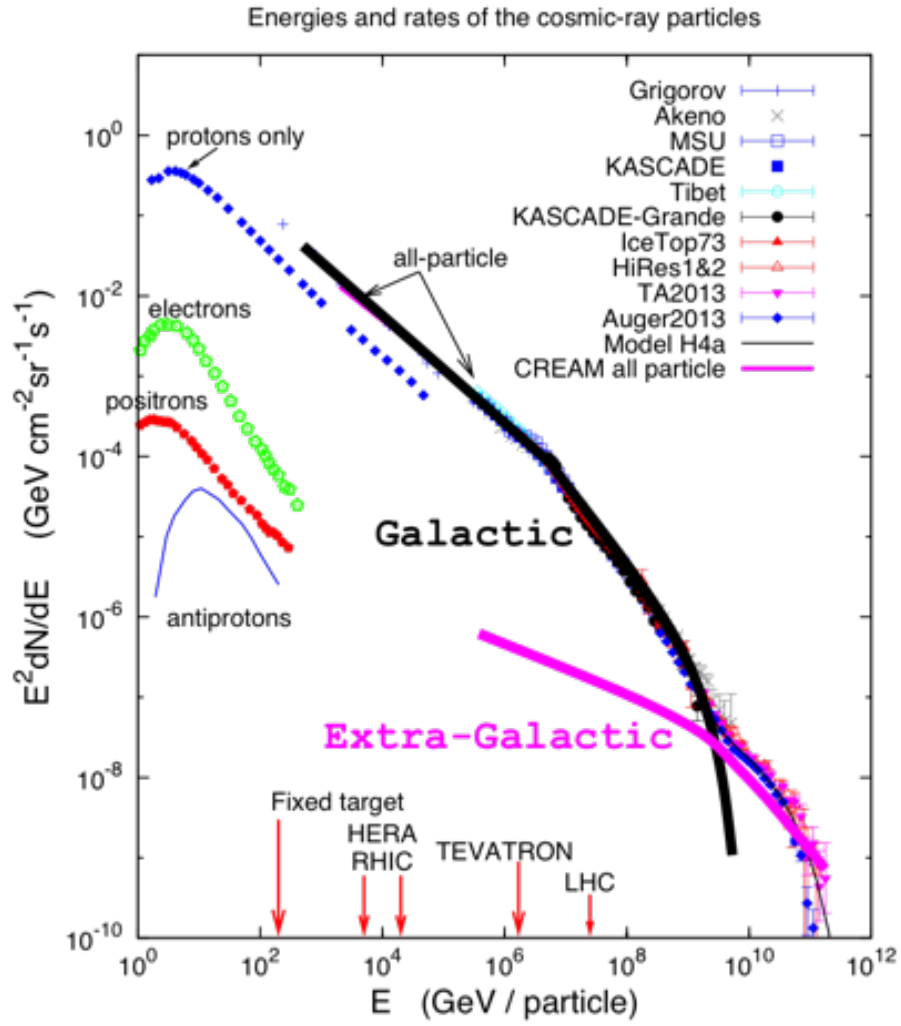
Figure 1.1: Number flux of CRs, weighted by E^2 as function of particle energy. Data from different CRs experiment are represented as shown in the legend.

flux drops below the extended power-law. This is due to the solar wind, that with his magnetic field is able to prevent the propagation of the low energy CRs. At high energies the flux shows extra features. The power-law index describing it has two majors changes of slope. A knee, at $E_{\text{knee}} \simeq 3 \times 10^{15}$ eV, corresponds to a steepening of the slope to $p \simeq 3.1$. An ankle, at $E_{\text{ankle}} \simeq 10^{18}$ eV, corresponds instead to an hardening of the slope. Finally the GZK-limit (Greisen 1966) imposes an upper limit at $E \simeq 5 \times 10^{19}$ eV to the CRs flux due to the interaction of protons with the Cosmic Microwave Background (CMB).

The differences in energy magnitude of the particles are associated to different origins of the CRs. An increment of the energy of a particle corresponds to an increment of the gyroradius of the particle while interacting with a magnetic field. When the energy is high enough to correspond to a gyroradius larger than the galactic halo the particle is supposed to have an extra-galactic origin. This is thought to happen around $E \simeq 10^{17} - 10^{18}$ eV (Aloisio et al. 2012).

Galactic CRs are thought to be originated by Supernovae remnants (Ackermann et al. 2013), such as the Crab Nebula. In these objects particles acceleration is thought to happen in shock waves generated by stellar explosions.

The identification of sources for extra-galactic CRs and the acceleration mechanisms that can reach the energies over the ankle are still open problems. This is firstly due to the lack of statistic, the flux for the extra-galactic CRs is in fact less than one particle per km^2 per year. Additionally being able to point back at the exact source generating CRs is not trivial due to the interaction that these charged particles can have along their path. For this reason $\gamma-$rays and more recently neutrinos (Aartsen et al. 2020; Abbasi et al. 2022; Albert et al. 2022) has been studied with particular interest, due to their ability, being neutral particles, to travel undeflected through the space.

Active galactic nuclei (AGNs) are a possible source candidate for extra-galactic (CRs). They are between the most energetic astrophysical objects in the universe, so their energy is sufficient to accelerate particles to the required energies. Additionally AGNs appear to be a possible source of neutrinos (Aartsen et al. 2018; Abbasi et al. 2022) and as a consequence of non-thermal proton populations.

Other possible sources are Galaxy cluster and Gamma-ray bursts (GRBs), in which the acceleration processes could lead particles energy up to 10^{20} eV and neutron stars, in which heavy nuclei can be accelerated by electric fields to the required energies.
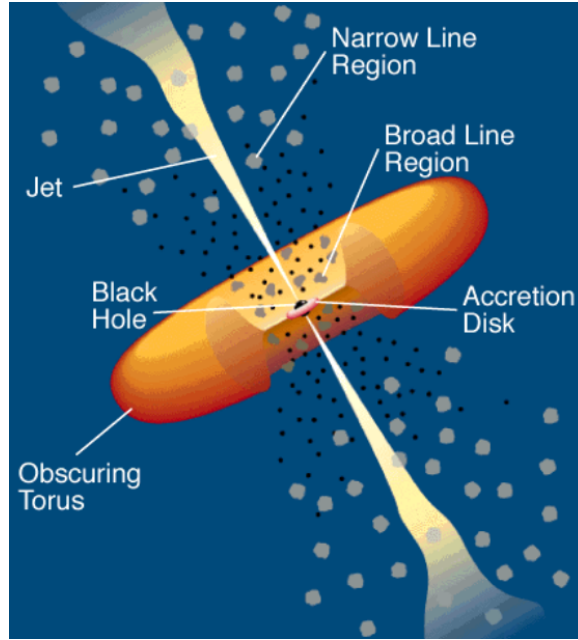
Figure 1.2: Sketch of the structure of an AGN.

1.1.2 Extra-galactic sources

Answering the fundamental question about the origin of extra-galactic CRs requires an efficient acceleration mechanism able to produce a power-law spectrum over many magnitudes in energy. The open problems on specific extra-galactic sources, however, contribute to answer the same question, but they may add additional requirements able to distinguish between different acceleration mechanisms.

AGNs and GRBs are two examples of extra-galactic sources that can develop a jet and candidate as CRs sources. There are strong theoretical motivations to consider their jets as magnetically dominated at the base (Blandford & Znajek 1977; Blandford & Payne 1982). If part of the magnetic energy is used to accelerate the flow to relativistic speed, the jet is Poyting-dominated when reaches the dissipation distance. Diffusive shock acceleration (DSA) is inefficient for the large plasma magnetization that is expected at this distance (Kennel & Coroniti 1984). A more likely candidate for these plasma conditions is magnetic reconnection (MR). Magnetically dominated jets can undergo to different instabilities (e.g. current-driven kink instabilities) that generates magnetic reconnection as common byproduct in particularly turbulent regions (Singh et al. 2016; Medina-Torrejón et al. 2021).

1.1.2.1 Active Galactic Nuclei

AGNs are, as described before, interesting extra-galactic CRs source candidates. It is useful to look for open problems able to shed light on the acceleration mechanisms and region in which the processes may happen.

AGNs are the nuclei of galaxies which show energetic phenomena that can not clearly and directly be attributed to stars. Fig. 1.2 shows a sketch of the structure of an AGN. At the center of the galaxy a Super Massive Black Hole (SMBH) is surrounded by an accretion disk. The SMBHs masses can range from 10^6 to $10^{10} M_\odot$ (Kormendy & Richstone 1995). The friction of the material spiraling towards the SMBH in the accretion disk produces radiation diffusing away. The integral of the different spectra produced by the accretion disk at different radii generate the so called Multicolor BB Spectrum in the Shakura-Sunyaev model (Shakura & Sunyaev 1973).

AGNs are characterized by some interesting properties as very high luminosities (up to $L_{\rm bol} \sim 10^{48}\,{\rm erg\,s^{-1}}$) that make AGNs the most powerful non-explosive category of sources in the Universe. They are observed up to very high redshift, currently up to $z \simeq 7.6$ (Wang et al. 2021). Based on the rapid variability observed, they are supposed to have small emitting regions (down to milliparsec) in most bands (Ulrich et al. 1997) with high energy densities. Their emissions cover the whole electromagnetic spectrum, as shown in Fig. 1.3.

Another important component that can be present in the AGNs morphology and of particular interest in this thesis is a jet. They are highly collimated outflows emerging on opposite direction near the disk. They can extent for extremely large scale in comparison to the AGN. The relativistic particles in the jet produce synchrotron emission (the first bump in Fig. 1.3), but they can emit also in the $\gamma-$ray band with different processes (the second bump in Fig. 1.3). The two main models explaining the γ-ray emissions in jets are the synchrotron self-Compton model (SSC), where the particles generating the synchrotron radiation are the same able to up-scatter the photons to higher energies, and the external radiation Compton model (EC), where an external radiation, coming from outside the jet, undergone a Comptonization of the original spectrum, populating the γ-ray band. The possible origins of the external radiation include CMB, radiation from the accretion disk and emission from the dust or the broad line region (See Fig. 1.2).

Some open problems that can shed light on the acceleration mechanisms in AGN jets are introduced. Ultrafast variability in AGNs, with an enhancement of the spectral energy density (SED) over less than 10 minutes timescale (Aharonian et al. 2007a) imposes strong limits on the radius of the emission zone that are difficult to explain
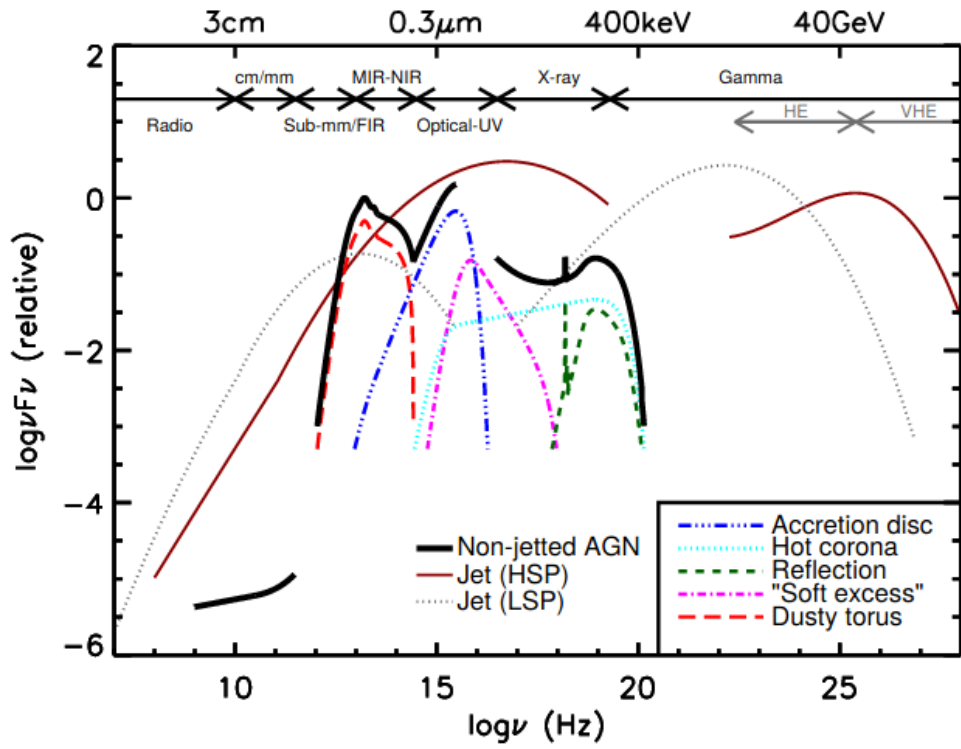
Figure 1.3: A schematic representation of an AGN spectral energy distribution (SED) (Padovani et al. 2017). The black solid curve represents the total emission and the various coloured curves (shifted down for clarity) represent the individual components. The jet SED is also shown for a high synchrotron peaked blazar (HSP) and a low synchrotron peaked blazar (LSP) as shown in the legend.
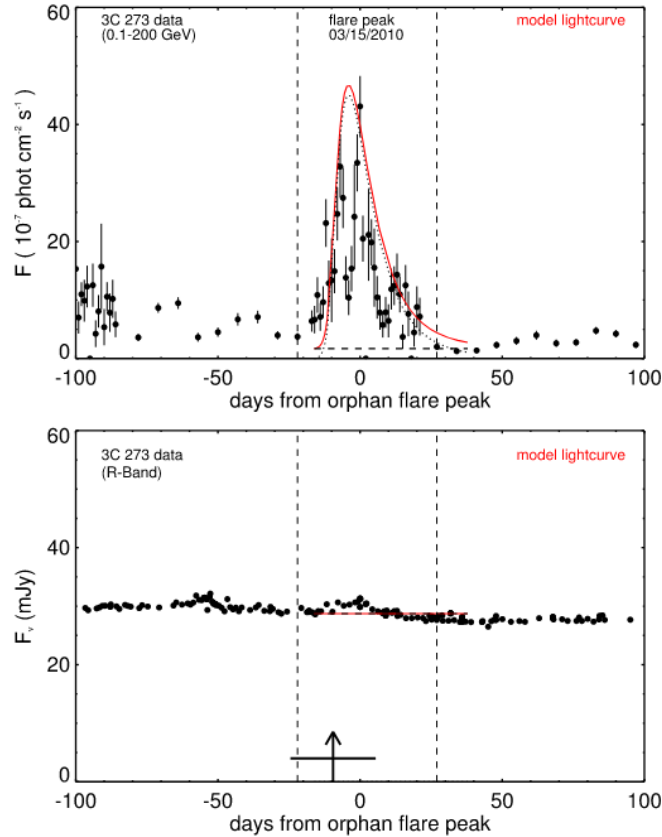
Figure 1.4: Light curves of 3C 273 (black circles) in the γ-rays (upper panel) and optical (lower panel) during an orphan $\gamma-$rays flare (MacDonald et al. 2017).

with DSA. On the other hand, strong MR events could happen in very localized regions and produce a fast flare when their emission is aligned with the observer (Giannios 2013; Petropoulou et al. 2016).

Orphan $\gamma-$ray flares in blazars, in which during a $\gamma-$rays flare in the optical counterpart a similar enhancement is missing (MacDonald et al. 2017) (Fig. 1.4), have a possible explanation with MR simulations at the kinetic level (Sobacchi et al. 2021) and should be assessed with large scale simulations.

1.2   High energy particles acceleration mechanisms

The observed high-energy γ-rays from extra-galactic sources and CRs require efficient acceleration mechanisms, able to convert the energy present in the extra-galactic sources into non-thermal particles populations and to reach the energy of the extra-galactic component of CRs ($E \gtrsim 10^{17} - 10^{18}$ eV).

A possible mechanism was proposed initially by Fermi (Fermi 1949, 1954). It considers
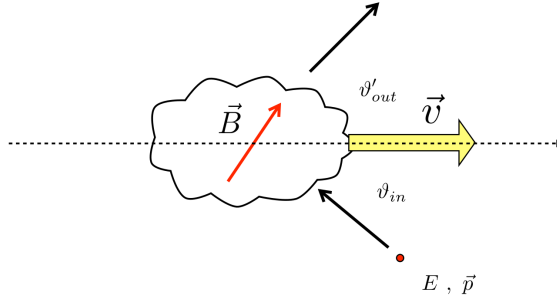
Figure 1.5: Sketch of the collision between a magnetic cloud and a particle in the Fermi second order mechanism. Primed quantities are measured in the rest frame of the cloud.

a magnetized cloud moving at non-relativistic velocity $U = \beta c$, where c is the speed of light, and a particle with relativistic velocity v. A sketch of a collision between a magnetic cloud and a particle is shown in Fig. 1.5. During a collision the energy gain is:

$$\frac{\Delta E}{E} = \beta \left(\cos\theta'_{out} - \cos\theta_{in} \right) + \beta^2 \left(1 - \cos\theta_{in}\cos\theta'_{out} \right) \; . \tag{1.2}$$

where primed quantities are measured in the rest frame of the cloud and θ_{in} and θ'_{out} are represented in Fig. 1.5. When considering an head-on collision the energy gain from Eq. (1.2) is $\Delta E/E = 2\beta(1 + \beta)$, while for a tail-on collision the rate gives an energy loss $\Delta E/E = -2\beta(1 - \beta)$. The average energy gain from Eq. (1.2) is evaluated. The hypothesis of isotropic distribution of particles in the cloud frame cancels out the term $\langle \cos\theta'_{out} \rangle$. The only angle factor remaining is $\langle \cos\theta_{in} \rangle = -\beta/3$, so that the average energy gain is:

$$\langle \frac{\Delta E}{E} \rangle \simeq \frac{4}{3}\beta^2 \; . \tag{1.3}$$

The mechanism, known as Fermi second order due to the index in Eq. (1.3), is inefficient and too slow.

1.2.1 Diffusive Shock Acceleration

A simple idea to improve the efficiency of Fermi second order is to find a physical situation in which the average is restricted to head-on collision, for which the maximum energy gain is achieved. Initially, acceleration of particles bouncing between converging walls of magnetized clouds was proposed. By restricting the average to head-on collision only in Eq. (1.2) it is possible to estimate the mean energy gain:
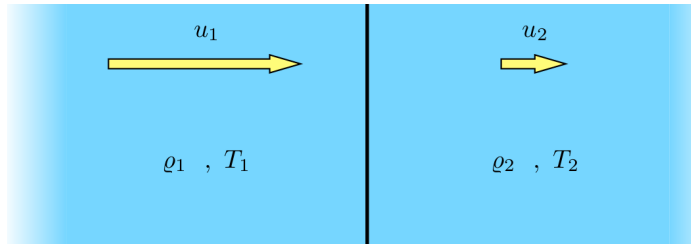
Figure 1.6: Sketch of a discontinuity in presence of a shock. The region on the left represents the up-stream region, while on the right it is represented the down-stream one.

$$\langle \frac{\Delta E}{E} \rangle \simeq \frac{4}{3} \beta \ . \tag{1.4}$$

The dependency of the average energy gain is linear under this additional hypothesis and for this reason the mechanisms producing such an average energy gain are usually known as Fermi first order.

Shocks were proposed as possible environment for the realization of Fermi first order (Hoyle 1960). They are in fact waves that propagate in plasma are characterized by an abrupt discontinuity in the plasma quantities, as represented in Fig. 1.6. The quantities in the up-stream and down-stream regions (as described in Fig. 1.6) are related by the Rankine–Hugoniot jump conditions, requiring along the shock, in a frame comoving with the discontinuity, conservation of mass, momentum and energy. It is additionally assumed that magnetic turbulence in the vicinity of the shock efficiently scatters off the particles, so that they are effectively isotropized on each side of the shock, meaning that their mean velocity follows the local flow velocity. Then the particles injected in a region with a shock can repeatedly cross the shock back and forth. Every time a particle crosses the shock, it undergoes an head-on collision with the plasma moving at velocity $u_1 - u_2$. The configuration is then a possible realization of the Fermi first order mechanism.

The Diffusive Shock Acceleration (DSA) is the name of the acceleration method and it results in a power-law spectra distribution (Axford et al. 1977; Krymskii 1977; Bell 1978; Blandford & Ostriker 1978; Drury 1983; Kirk et al. 2000; Achterberg et al. 2001). The final power-law depends on the strength of the magnetized shock (through the compression ratio r, defined as the ratio of up-stream and down-stream velocities in the shock rest frame) and the orientation of the magnetic field lines with respect to the shock normal (Jokipii 1987; Ballard & Heavens 1991; Summerlin & Baring 2011). Analytical results for the expected power-law have also been found for parallel relativistic shocks (Kirk et al. 2000; Keshet & Waxman 2005) and perpendicular ones (Takamoto & Kirk 2015).

Although DSA is an efficient acceleration mechanism, there are some plasma conditions that can suppress its efficiency. Perpendicular shock are inefficient for high magnetization values (Sironi et al. 2015; Plotnikov et al. 2018). AGN jets for example are in the vicinity of the supermassive black hole (SMBH) considered highly magnetized. The plasma is then magnetized until dissipative processes occur, reaching then the equipartition between the magnetic and the kinetic energy densities (the magnetization parameter) (Komissarov et al. 2007; Lyubarsky 2009). It is possible to have in these astrophysical environments a competition with a different acceleration method more efficient in higly magnetized plasma: magnetic reconnection.

1.2.2 Magnetic Reconnection

In the framework of high magnetized flows MR arises as an acceleration mechanism to consider. MR is non-ideal phenomenon and a natural byproduct of instabilities that are both observed and found in simulations in astrophysical jets.
The main consequences of MR are the transfer of magnetic field energy into thermal and kinetic energy and particles acceleration to non-thermal energies through a rearrangement of the magnetic field topology. MR aditionally lowers the magnetic energy in systems towards the equipartition. Similarly to the DSA (Sec. 1.2.1) the non-thermal spectra result of MR events can be described as a power-law depending on the plasma parameters surrounding the MR region as it will be described in details in Sec. 3.2.
With final spectra similar to the one obtained during DSA and a natural environment in highly magnetized flows, MR is a promising candidate as a viable mechanisms in many different astrophysical objects.

1.3 Outline

As seen in the introduction, when taking into account the problem of particles acceleration in astrophysical plasma, DSA and MR are the most likely mechanisms that could take place. Both are capable to accelerate particles to power-law spectra matching the observations from extra-galactic sources and they could be the responsible for CRs acceleration to the highest energies. Additionally, both can be characterized by the plasma surrounding the acceleration sites, allowing the implementation in large scale MHD simulations through sub-grid models. They are more efficient in different conditions, mainly due to the different plasma magnetization, in which MR is more likely to be efficient than DSA when the value of the magnetization is high. MR has

been in fact extensively studied with Particle-in-cell (PIC) simulations, being able to follow the kinematics of individual particles through the development of MR. The same approach is unfeasible in large scale (R)MHD simulations, where simulations of astrophysical objects would reach scales that would make computationally impossible to follow the individual particles.

The goal of the thesis is to implement a numerical framework in which both the phenomena can be studied with R(MHD) simulations, through the implementation of a sub-grid model for the MR in the PLUTO code (Mignone et al. 2007). In this code a sub-grid model for DSA is already present (Vaidya et al. 2018) and the inclusion of a similar approach for MR would make possible to follow spectra evolution due to both the phenomena during space and time dependent (R)MHD simulations.

The thesis is organized as follow: in Chap. 2 magnetohydrodynamics (MHD) equations are derived together with their relativistic counterpart, in Chap. 3 the main model and results on MR are analized in detail, in Chap. 4 a new algorithm to identify MR regions in large scale (R)MHD simulation is introduced, in Chap. 5 the algorithm necessary to sample in (R)MHD main plasma parameters needed for post-MR spectra update is presented and tested in 2D jet and in 3D unstable plasma column simulations, in Chap. 6 the strategy to update the particles spectra using the identification method and the sampling algorithm is introduced and tested in 3D unstable plasma column simulations and finally in Chap. 7 conclusions are presented, together with the future perspectives for the work presented in this thesis.

2

Magnetohydrodynamics

Plasma can be considered the fourth state of matter. At high temperatures the gas atoms split in electrons and positive ions, forming an ionised gas. In this regime the dynamics is dominated by electromagnetic interactions. Plasma is common in astrophysical environments and it is indeed the most abundant form in which the ordinary matter organizes in the universe.

Different models may be used to describe a plasma at different scales, in particular the MHD model is used for describing the large scale evolution of astrophysical plasmas in extragalactic objects (e.g. astrophysical jets). In this chapter we introduce this model and the relevant equations.

The Chapter is organized as follow: in Sec. 2.1 the standard description of plasma is provided, in Sec. 2.2 the basis of the Kinetic theory are described, in Sec. 2.3 the basic equations of MHD are presented and finally on Sec. 2.4 the relativistic extension of the previous equation is provided.

2.1 Standard plasma description

The most complete description of a plasma entails following the trajectory of every particle in the electromagnetic field self-consistently generated by the particle distribution. The electromagnetic field is described by the Maxwell equations:

$$\nabla \times \boldsymbol{E} = -\frac{1}{c}\frac{\partial \boldsymbol{B}}{\partial t}$$
$$\nabla \times \boldsymbol{B} = \frac{1}{c}\frac{\partial \boldsymbol{E}}{\partial t} + \frac{4\pi}{c}\boldsymbol{J} \qquad (2.1)$$
$$\nabla \cdot \boldsymbol{E} = 4\pi q$$
$$\nabla \cdot \boldsymbol{B} = 0 \ .$$

Eq. (2.1) describes the spatial and temporal behaviour of the magnetic and electric fields $\boldsymbol{E}$ and $\boldsymbol{B}$ under the effect of the charge density q and the current density $\boldsymbol{J}$ that are defined as:

$$q(\boldsymbol{r},t) = \sum_{i=1}^{N} e_i \delta \left[\boldsymbol{r} - \boldsymbol{r}_i(t)\right]$$
$$\boldsymbol{J}(\boldsymbol{r},t) = \sum_{i=1}^{N} e_i \boldsymbol{v}_i(t) \delta \left[\boldsymbol{r} - \boldsymbol{r}_i(t)\right] \ , \qquad (2.2)$$

where e_i represents the charge of the $i-$th particle and $\boldsymbol{r}_i$ and $\boldsymbol{v}_i$ are respectively the particle position and velocity. It is possible to consider in the definition of $\boldsymbol{J}$ and q also the presence of external sources.

From the combination of the divergence of the 2nd equation and the third equation in Eq. (2.1) it is possible to derive the so called equation of charge conservation:

$$\nabla \cdot \boldsymbol{J} + \frac{\partial q}{\partial t} = 0 \ . \qquad (2.3)$$

Eqs. (2.1) and (2.2) represent 10 independent equations, while the system has $3N+10$ unknowns $\boldsymbol{r}_i$, $\boldsymbol{E}$, $\boldsymbol{B}$, $\boldsymbol{J}$ and q. The remaining equations describe the motion of the charged particles due to the magnetic and electric fields:

$$m_i \frac{\partial^2 \boldsymbol{r}_i}{\partial t^2} = e_i \left(\boldsymbol{E} + \frac{1}{c}\frac{\partial \boldsymbol{r}_i}{\partial t} \times \boldsymbol{B}\right) \ . \qquad (2.4)$$

This approach can theoretically follow the trajectory of each individual particle present in the system. Nevertheless the study of such a nonlinear system of equations would be extremely complex, it would require the knowledge of the initial conditions for each individual particle in the plasma and would give a number of informations that would be impossible to compare with experimental results.

2.2 Kinetic theory

The first step towards the definition of the MHD equations is to describe the system introduced in Sec. 2.1 from a statistical point of view. It is first possible to define a distribution function $f(\boldsymbol{r}, \boldsymbol{v}, t)$, where the quantity $\mathrm{d}N = f(\boldsymbol{r}, \boldsymbol{v}, t)\mathrm{d}\boldsymbol{r}\mathrm{d}\boldsymbol{v}$ represents the average number of particles in the volume $\mathrm{d}\boldsymbol{r}\mathrm{d}\boldsymbol{v}$ in the phase space.

The equations describing such system can be determined by considering the conserved quantities and by deriving the corresponding conservation equations.

$$\frac{\partial f}{\partial t} + \nabla \cdot (f\boldsymbol{v}) = 0 \ , \tag{2.5}$$

where it has to be taken into account that the operator ∇ is applied in the phase space volume so it will act as $\nabla + \nabla_{\boldsymbol{v}}$.

Eq. (2.5) becomes then:

$$\frac{\partial f}{\partial t} + \boldsymbol{v} \cdot \nabla f + \frac{\boldsymbol{F}}{m} \cdot \nabla_{\boldsymbol{v}} f = 0 \ , \tag{2.6}$$

where it has been taken into account that in the phase space $\boldsymbol{r}$ and $\boldsymbol{v}$ are independent variables and that $f\nabla_{\boldsymbol{v}} \cdot (\boldsymbol{F}/m) = 0$.

Eq. (2.6) is the conservation equation for the integrated quantity N, defined as:

$$N = \int_V f(\boldsymbol{r}, \boldsymbol{v}, t)\mathrm{d}\boldsymbol{r}\mathrm{d}\boldsymbol{v} \ , \tag{2.7}$$

where the volume V is the phase space volume.

An additional hypothesis necessary to obtain Eq. (2.6) is that interactions involving two particles at the time are not taken into account. This would induce an additional collision term in the equation. If this hypothesis is reasonable we can then call our system as a collisionless plasma.

In the case of a plasma the force $\boldsymbol{F}$ can be written explicitly as:

$$\boldsymbol{F} = e_0 \left(\boldsymbol{E} + \frac{1}{c}\boldsymbol{v} \times \boldsymbol{B} \right) \ , \tag{2.8}$$

and by neglecting other collective type of forces that can be present in the system, for example gravitational forces, it is obtained the Vlasov equation:

$$\frac{\partial f}{\partial t} + \boldsymbol{v} \cdot \nabla f + \frac{e_0}{m}(\boldsymbol{E} + \frac{1}{c}\boldsymbol{v} \times \boldsymbol{B}) \cdot \nabla_{\boldsymbol{v}} f = 0 \ . \tag{2.9}$$

Eq. (2.9) is, in the generic case, non-linear and a comparison of a solution with data would require to define and study moments of the distribution f. It is possible for example to define for any velocity-dependent quantity Φ:

$$\langle \Phi \rangle = \frac{\int \Phi(\boldsymbol{v}) f(\boldsymbol{r}, \boldsymbol{v}, t) \mathrm{d}\boldsymbol{v}}{\int f(\boldsymbol{r}, \boldsymbol{v}, t) \mathrm{d}\boldsymbol{v}} = \frac{1}{n(\boldsymbol{r}, t)} \int \Phi(\boldsymbol{v}) f(\boldsymbol{r}, \boldsymbol{v}, t) \mathrm{d}\boldsymbol{v} , \qquad (2.10)$$

where $n(\boldsymbol{r}, t) = \int f(\boldsymbol{r}, \boldsymbol{v}, t) \mathrm{d}\boldsymbol{v}$ represents the numerical density of the system.

The general $n-$th order moment is defined as:

$$\int (v_i v_j \ldots v_k) f(\boldsymbol{r}, \boldsymbol{v}, t) d\boldsymbol{v} , \qquad (2.11)$$

where it has been defined $\Phi(\boldsymbol{v}) = v_i v_j \ldots v_k$, product of n velocity components.

It is possible to study the time evolution of the moment by taking moments of Eq. (2.9) and obtaining the general moment equation:

$$\frac{\partial}{\partial t}(n\langle \Phi \rangle) + \nabla \cdot (n\langle \boldsymbol{v}\Phi \rangle) - \frac{n}{m} e_0 \boldsymbol{E} \cdot \langle \nabla_{\boldsymbol{v}} \Phi \rangle - \frac{ne_0}{mc} \langle (\boldsymbol{v} \times \boldsymbol{B}) \cdot \nabla_{\boldsymbol{v}} \Phi \rangle = 0 . \qquad (2.12)$$

2.2.1 One-fluid model

The following step in the statistical description of plasma properties is to use the formalism introduced in Sec. 2.2 in order to derive equations that relate different moments of the distribution function f. In this way we arrive at a fluid description in term of macroscopic quantities and we do not require anymore a full knowledge of f in order to study the system.

In general, for a plasma of protons and electrons, we will have two fluids. However, if the two species are in thermodynamic equilibrium, we can reduce to a single species. The main quantities describing this model are then defined as $n = n_e + n_p$ for the numerical density, $\rho = n_p m_p + n_e m_e$ for the mass density, $q = e(n_p - n_e)$ for the charge density and $\boldsymbol{J} = e(n_p \boldsymbol{u}^p - n_e \boldsymbol{u}^e)$ for the current density, where $\boldsymbol{u}$ represent the bulk velocity and e represents the charge unit.

By studying the general moment equations, Eq. (2.12), under these assumptions it is possible to derive the equations describing the system. The continuity equation describing temporal evolution for the mass density ρ is:

$$\frac{\partial \rho}{\partial t} + \nabla \cdot (\rho \boldsymbol{U}) = 0 , \qquad (2.13)$$

where $\boldsymbol{U}$ is the fluid velocity defined as:

$$\boldsymbol{U} = \frac{m_e n_e \boldsymbol{u}^{(e)} + m_p n_p \boldsymbol{u}^{(p)}}{\rho} . \qquad (2.14)$$

Likewise, it is possible to derive the charge conservation equation:

$$\frac{\partial q}{\partial t} + \nabla \cdot \boldsymbol{J} = 0 \ . \tag{2.15}$$

The equation of motion can be described in terms of the definition of $\boldsymbol{U}$ from Eq. (2.14):

$$\rho \frac{\mathrm{d}\boldsymbol{U}}{\mathrm{d}t} = -\nabla \cdot \boldsymbol{P} + q\boldsymbol{E} + \frac{1}{c}(\boldsymbol{J} \times \boldsymbol{B}) \ , \tag{2.16}$$

where we have defined a pressure tensor $\boldsymbol{P}$ and the respective components for the two different species (indices (s) when refers to the generic one) as:

$$\begin{aligned} P_{ik} &= P_{ik}^{(e)} + P_{ik}^{(p)} \\ P_{ik}^{(s)} &= n_s m_s \langle w_i' w_k' \rangle = P\delta_{ik} + \Pi_{ik} \ . \end{aligned} \tag{2.17}$$

The pressure tensor takes into account the displacements in velocity of the particles in the system with the definition of this displacement in terms of the fluid velocity $\boldsymbol{U}$ and reads as:

$$\boldsymbol{w}' = \boldsymbol{v} - \boldsymbol{U} \ . \tag{2.18}$$

The energy equation of the one-fluid model is:

$$\frac{1}{\Gamma - 1}\rho^\Gamma \frac{\mathrm{d}}{\mathrm{d}t}\left(P\rho^{-\Gamma}\right) = -\Pi_{ik}\frac{\partial U_i}{\partial x_k} - \frac{\partial q_k}{\partial x_k} + (qU_k - J_k)\left[E_k + \frac{1}{c}(\boldsymbol{U} \times \boldsymbol{B})_k\right] \ , \tag{2.19}$$

where $\Gamma = 5/3$ in the case of a mono-atomic gas and q_k represent the $k-$th component of the heat flux vector, defined as:

$$\boldsymbol{q} = n\langle \boldsymbol{w}(1/2mw^2)\rangle \ . \tag{2.20}$$

The system described so far consists of 12 scalar equation (Eq. 2.13, 2.15, 2.16 and 2.19 together with the Maxwell's equation for $\nabla \times \boldsymbol{E}$ and $\nabla \times \boldsymbol{B}$) and 21 unknowns. In order to complete the system of equations we need to introduce another vectorial equation and then to define a closure, an equation describing the relation between Π_{ik}, $P_{ik}^{(e)}$ and $\boldsymbol{q}$. The additional required equation is the generalized Ohm's equation and can be obtained subtracting the equation of motion of the two particles species that are considered in this model:

$$\begin{aligned} E_i + \frac{1}{c}(\boldsymbol{U} \times \boldsymbol{B})_i - \frac{J_i}{\sigma_{\mathrm{ec}}} &= \frac{m_e}{e^2 n_e}\left[\frac{\partial J_i}{\partial t} + \frac{\partial}{\partial x_k}\left(J_i U_k + J_k U_i\right)\right] \\ &\quad + \frac{1}{en_e c}(\boldsymbol{J} \times \boldsymbol{B})_i - \frac{1}{en_e}\frac{\partial \mathrm{P}_{ik}^{(e)}}{\partial x_k} \ , \end{aligned} \tag{2.21}$$

where the plasma electric conductivity has been introduced as:

$$\sigma_{\mathrm{ec}} = \frac{e^2 n_e}{m_e \nu_{e,p}} \ . \tag{2.22}$$

and $\nu_{e,p}$ represents the average frequency for collision of electrons with protons species. The only missing equation is the one describing the closure of the system. It is possible to close the system without considering higher moment equations assuming different hypothesis:

- Cold plasma model: all the thermal effects are neglected, so that all the component of $\boldsymbol{P}_{ik}$ and $\boldsymbol{q}$ vanishes. What is obtained is an ideal system in which all the effects of particles collisions are neglected,

- Collisional plasma: the plasma is considered always in thermodynamical equilibrium, so that its distribution can be described as a Maxwellian. This assumption requires that $\Pi = 0$, $\boldsymbol{q} = 0$ while $P \neq 0$

2.3   Magnetohydrodynamics

A possible approach that allows to study plasma properties is to focus on a specific regime, defining characteristic spatial and time scales fundamental for the system in exam and to neglect the terms that become unimportant when in this specific regime. We can define characteristic timescales for the MHD regime, namely a spatial scale $\mathcal{L}$ and a timescale τ over which the fields that we are going to consider have a significant variation and a velocity $\mathcal{U}$ describing the fluid velocity of the plasma.

We define MHD regime as the one for which the speed of the electromagnetic phenomena, that we can define as $\mathcal{L}/\tau$, is of the same order of the typical speed of the hydrodynamical ones, which speed is defined as $\mathcal{U}$. For the non-relativistic case we also assume that these velocities are smaller than the speed of light, so that $\mathcal{U} \ll c$. Starting from Maxwell equations of Eq. (2.1), together with the equations of the one-fluid collisional model described in Sec. 2.2.1, we can carry out a dimensional analysis, by defining characteristic values also for $\mathcal{E}$, $\mathcal{B}$, $\mathcal{Q}$ and $\mathcal{J}$, respectively electric and magnetic fields, charge and current density.

From the fist Maxwell equation it is possible to deduce that $\mathcal{E}/\mathcal{B} \ll 1$:

$$\nabla \times \boldsymbol{E} = -\frac{1}{c}\frac{\partial B}{\partial t} \ \Rightarrow \ \frac{\mathcal{E}}{\mathcal{L}} \simeq \frac{1}{c}\frac{\mathcal{B}}{\tau} \ \Rightarrow \ \frac{\mathcal{E}}{\mathcal{B}} \ll 1 \ . \tag{2.23}$$

In the second Maxwell equation it is possible to show that the contribution of the term due to the temporal variation of the electric field is negligible so that the equation reduces to:

$$\nabla \times \boldsymbol{B} = \frac{4\pi}{c} \boldsymbol{J} \ . \tag{2.24}$$

The neglection of the displacement current clarify what we intend as MHD regime. Neglecting the displacement current (which is typically related to high-frequency phenomena) is consistent with the assumption of MHD being a low-frequency regime. The consequence of Eq. (2.24) is that the charge conservation equation (Eq. 2.15) reduces as follow:

$$\frac{\partial q}{\partial t} + \nabla \cdot \boldsymbol{J} = 0 \ \Rightarrow \ \frac{\mathcal{Q}}{\tau} + \frac{\mathcal{J}}{\mathcal{L}} = 0 \ . \tag{2.25}$$

Taking $\mathcal{J}$ from Eq. (2.24) we obtain that $\frac{\mathcal{E}}{\mathcal{B}}\frac{\mathcal{L}}{\tau} \simeq \left(\frac{\mathcal{U}}{c}\right)^2 \ll 1$, so that the equation for charge conservation can be written simply as:

$$\nabla \cdot \boldsymbol{J} = 0 \ . \tag{2.26}$$

In the momentum equation (Eq. 2.16) it is possible to show that the electric part of the force can be neglected obtaining:

$$\rho \frac{d\boldsymbol{U}}{dt} = -\nabla P + \frac{1}{c} \boldsymbol{J} \times \boldsymbol{B} \ . \tag{2.27}$$

Ohm's equation Eq. (2.21) requires some further work. We can define:

$$\omega \simeq \tau^{-1} \qquad c_s \simeq \left(\frac{P}{\rho}\right)^{1/2} \ . \tag{2.28}$$

Neglecting terms in the square bracket and proportional to $\boldsymbol{J} \times \boldsymbol{B}$ requires respectively:

$$\omega/\omega_{pe} \ll \mathcal{U}/c \qquad \omega/\omega_{cp} \ll (\mathcal{U}/c_a)^2 \ , \tag{2.29}$$

where $c_a = B/\sqrt{4\pi m_p n_p}$ is the Alfven velocity, ω_{pe} is the electron plasma frequency and ω_{cp} is the proton cyclotron frequency. In the low frequency regime these conditions are typically satisfied and Ohm's equation reduces to Ohm's equation for resistive plasma:

$$\boldsymbol{E} + \frac{1}{c} \boldsymbol{U} \times \boldsymbol{B} = \frac{\boldsymbol{J}}{\sigma_{\mathrm{ec}}} \ . \tag{2.30}$$

Under the condition:

$$\omega \nu_{ep}/\omega_{pe}^2 \ll (\mathcal{U}/c)^2 \; , \tag{2.31}$$

where ω_{pe} is the electron plasma frequency then also the right hand side can be neglected and we obtain the Ohm's equation for ideal plasma:

$$\boldsymbol{E} + \frac{1}{c}\boldsymbol{U} \times \boldsymbol{B} = 0 \; . \tag{2.32}$$

The energy equation describing the one-fluid model (Eq. 2.19) with the additional hypothesis of the collisional regime has the term $\mathcal{Q}\mathcal{U}$ of the order $(\mathcal{U}/c)^2$ with respect to $\mathcal{J}$ and the equation can be written as:

$$\frac{1}{\Gamma-1}\rho^{\Gamma}\frac{d}{dt}\left(P\rho^{-\Gamma}\right) = \frac{J^2}{\sigma_{\mathrm{ec}}} \; . \tag{2.33}$$

In addition to the previous equations we should consider also the equation that still contains the electric field:

$$\nabla \times \boldsymbol{E} = -\frac{1}{c}\frac{\partial \boldsymbol{B}}{\partial t} \; . \tag{2.34}$$

This equation governs the dynamics of magnetic fields. Finally by taking the curl of Ohm's equation substituting $\nabla \times \boldsymbol{E}$ from Eq. (2.34) we can obtain the so called magnetic induction equation or Faraday's equation:

$$\frac{\partial \boldsymbol{B}}{\partial t} = \nabla \times (\boldsymbol{U} \times \boldsymbol{B}) + \eta\nabla^2\boldsymbol{B} - \nabla\eta \times (\nabla \times \boldsymbol{B}) \; , \tag{2.35}$$

where we have introduced the magnetic diffusivity defined as:

$$\eta = \frac{c^2}{4\pi\sigma_{\mathrm{ec}}} \; . \tag{2.36}$$

Summarizing the MHD equations are:

$$
\begin{aligned}
\frac{\partial \rho}{\partial t} + \nabla \cdot (\rho\boldsymbol{U}) &= 0 \\
\rho\frac{d\boldsymbol{U}}{dt} &= -\nabla P + \frac{1}{c}\boldsymbol{J} \times \boldsymbol{B} = -\nabla P + \frac{1}{4\pi}(\nabla \times \boldsymbol{B}) \times \boldsymbol{B} \\
\frac{1}{\Gamma-1}\rho^{\Gamma}\frac{d}{dt}\left(P\rho^{-\Gamma}\right) &= \frac{4\pi}{c^2}\eta J^2 \\
\frac{\partial \boldsymbol{B}}{\partial t} &= \nabla \times (\boldsymbol{U} \times \boldsymbol{B}) + \eta\nabla^2\boldsymbol{B} - \nabla\eta \times (\nabla \times \boldsymbol{B}) \; .
\end{aligned}
\tag{2.37}
$$

Equations for the ideal plasma are obtained by neglecting the magnetic diffusivity so that $\eta = 0$ and they are:

$$\frac{\partial \rho}{\partial t} + \nabla \cdot (\rho \boldsymbol{U}) = 0$$

$$\rho \frac{\mathrm{d}\boldsymbol{U}}{\mathrm{d}t} = -\nabla P + \frac{1}{c}\boldsymbol{J} \times \boldsymbol{B} = -\nabla P + \frac{1}{4\pi}(\nabla \times \boldsymbol{B}) \times \boldsymbol{B}$$

$$\frac{1}{\Gamma - 1}\rho^{\Gamma}\frac{\mathrm{d}}{\mathrm{d}t}\left(P\rho^{-\Gamma}\right) = 0$$

$$\frac{\partial \boldsymbol{B}}{\partial t} = \nabla \times (\boldsymbol{U} \times \boldsymbol{B}) \ .$$

(2.38)

The system is closed and the other missing quantities can be deduced by:

$$\boldsymbol{J} = \frac{c}{4\pi}(\nabla \times \boldsymbol{B})$$

$$\boldsymbol{E} = -\frac{1}{c}\boldsymbol{U} \times \boldsymbol{B} + \frac{\boldsymbol{J}}{\sigma_{\mathrm{ec}}}$$

$$q = \frac{1}{4\pi}(\nabla \cdot \boldsymbol{E}) \ .$$

(2.39)

σ_{ec}, if present, is assumed a known quantity and is often considered a constant value. The MHD equations can be expressed in a conservation form:

$$\frac{\partial \rho}{\partial t} + \nabla \cdot (\rho \boldsymbol{U}) = 0$$

$$\frac{\partial}{\partial t}(\rho \boldsymbol{U}) + \nabla \cdot \left[\rho \boldsymbol{U}\boldsymbol{U} + \left(p + \frac{1}{2}B^2\right)\mathbf{I} - \boldsymbol{B}\boldsymbol{B}\right] = 0$$

$$\frac{\partial}{\partial t}\left(\frac{1}{2}\rho U^2 + \rho e + \frac{1}{2}B^2\right) + \nabla \cdot \left[\left(\frac{1}{2}\rho U^2 + \rho e + p + B^2\right)\boldsymbol{U} - \boldsymbol{U} \cdot \boldsymbol{B}\boldsymbol{B}\right] = 0$$

$$\frac{\partial \boldsymbol{B}}{\partial t} + \nabla \cdot (\boldsymbol{U}\boldsymbol{B} - \boldsymbol{B}\boldsymbol{U}) = 0 \ ,$$

(2.40)

where $\mathbf{I}$ is a 3×3 unit tensor and e is provided by an additional equation $\rho e = \rho e(\rho, p)$ that guarantee the closure of the equation system.

2.3.1 Magnetic Pressure and β parameter

The MHD equations (Eq. 2.37) allow to introduce a quantity that easily let understand the relative power of the hydrodynamical and magnetic effects in a system. The momentum equation can be re-expressed as:

$$\rho \frac{\mathrm{d}\boldsymbol{U}}{\mathrm{d}t} = -\nabla \left(P + \frac{B^2}{8\pi}\right) + \frac{1}{4\pi}(\boldsymbol{B}\nabla)\boldsymbol{B} \ .$$

(2.41)

Considering the i-th component and remembering that we have $\nabla \cdot \boldsymbol{B} = 0$ we can obtain:

$$\rho \frac{dU_i}{dt} = -\frac{\partial}{\partial x_k} T_{ik} \ , \tag{2.42}$$

where we have introduced a new tensor:

$$T_{ik} = \left(P + \frac{B^2}{8\pi} \right) \delta_{ik} - \frac{1}{4\pi} B_i B_k \ . \tag{2.43}$$

By assuming that the $z-$axis of the reference system is aligned (at least locally) to the magnetic field the tensor can be expressed as:

$$\begin{pmatrix} P + \frac{B^2}{8\pi} & 0 & 0 \\ 0 & P + \frac{B^2}{8\pi} & 0 \\ 0 & 0 & P - \frac{B^2}{8\pi} \end{pmatrix} \ . \tag{2.44}$$

The magnetic field introduces an extra isotropic pressure term $B^2/8\pi$ and a anisotropic negative pressure $-B^2/4\pi$ along the field. The interpretation of this expression can be understood thinking the field lines like an elastic material, in which any deformation induces a tension that tends to restore the configuration of straight lines.

A quantity to define the relative importance of the two pressure terms naturally arise as β parameter, defined as:

$$\beta = \frac{P}{B^2/8\pi} \ . \tag{2.45}$$

If $\beta \gg 1$ the system is then dominated by hydrodynamical effects, otherwise if $\beta \ll 1$ magnetic effects are dominating. In the case of magnetic reconnection the sites with $\beta \ll 1$ are of particolar interest, having more energy available to be converted in plasma heating and acceleration of particles to non-thermal energies.

2.3.2 The evolution of magnetic fields

It is possible to define a quantity comparing the timescale of the different terms describing the time evolution of the magnetic field $\boldsymbol{B}$ in the Faraday equation (Eq. 2.35).

By considering the case in which η is a constant value Eq. (2.35) reduces to:

$$\frac{\partial \boldsymbol{B}}{\partial t} = \nabla \times (\boldsymbol{U} \times \boldsymbol{B}) + \eta \nabla^2 \boldsymbol{B} \ . \tag{2.46}$$

By taking $\boldsymbol{U}$ as a known quantity the equation is closed. There are two terms describing different effects that can produce a time variation of the magnetic field in the right-hand side of the equation. The first term is the convective term, containing

the velocity $\boldsymbol{U}$ and describing how spatial changes on the velocity field can give rise to temporal changes of the magnetic field. The second term is the diffusive term.

It is possible to define typical timescales for the two phenomena using again a dimensional analysis as in Sec. 2.3 of Eq. (2.46):

$$\tau_f = \mathcal{L}/\mathcal{U} \qquad \tau_d = \mathcal{L}^2/\eta \ . \tag{2.47}$$

The ratio of the two timescales is called the magnetic Reynolds number:

$$\mathcal{R} = \frac{\tau_d}{\tau_f} = \frac{\mathcal{U}\mathcal{L}}{\eta} \ . \tag{2.48}$$

If the typical convection speed is of the same order of the Alfven speed (which we have defined in Sec. 2.3) then the number is called Lundquist number:

$$S = \frac{\tau_d}{\tau_f} = \frac{v_a \mathcal{L}}{\eta} \ . \tag{2.49}$$

If $\mathcal{R} \ll 1$ Eq. (2.46) reduces to:

$$\frac{\partial \boldsymbol{B}}{\partial t} = \eta \nabla^2 \boldsymbol{B} \ . \tag{2.50}$$

The resistivity η has the effect of generating a magnetic diffusion, in which the magnetic energy decreases and it is converted to thermal and kinetic energy. It is the regime in which magnetic reconnection take place, with the release of magnetic energy that can give rise to particles acceleration.

If $\mathcal{R} \gg 1$ instead Eq. (2.46) reduces to:

$$\frac{\partial \boldsymbol{B}}{\partial t} = \nabla \times (\boldsymbol{U} \times \boldsymbol{B}) \ . \tag{2.51}$$

The main consequence is the so called Alfven's theorem, stating that in this regime the magnetic flux through any closed line that is anchored to the fluid is constant in time. By shrinking the closed line down to reach a single field line the theorem has as effect that field lines can be considered frozen in the fluid. Since the fluid motion is described by a continuous function, the magnetic field lines can be bent and deformed, but not broken. This is an assumption adopted when we describe the system as ideal plasma. In many astrophysical environments this is a good approximation, but we have to be careful about systems in which the ideal plasma condition can be locally invalid and the diffusive term can then play an important role. This is particularly obvious in the case of magnetic reconnection, in which the release of energy is the result of the rearrangement of the magnetic field topology, requiring that the magnetic

field lines are broken and reconnected in a state with lower magnetic energy. These concepts are elaborated more in details in Chap. 3, where MR phenomenon is treated and the main results on particles acceleration due to MR are introduced.

2.4 Relativistic Magnetohydrodynamics

MHD formalism developed in Sec. 2.3 can be adapted to the relativistic case. In this case, the hypothesis that $\mathcal{U} \ll c$ is not valid anymore. The RMHD equations are:

$$
\begin{aligned}
&\partial_t \left(\gamma \rho \right) + \nabla \cdot \left(\gamma \rho \mathbf{v} \right) = 0 \\
&\partial_t \mathbf{m} + \nabla \cdot \left[\gamma^2 w \mathbf{v} \mathbf{v} - \mathbf{E} \mathbf{E} - \mathbf{B} \mathbf{B} + (p + u_{\text{em}}) \mathbf{I} \right] = 0 \\
&\partial_t \left(\gamma^2 w - p + u_{\text{em}} \right) + \nabla \cdot \left(\gamma^2 w \mathbf{v} + \mathbf{E} \times \mathbf{B} \right) = 0 \\
&\partial_t \mathbf{B} + \nabla \times \mathbf{E} = 0 \; ,
\end{aligned}
\tag{2.52}
$$

where ρ is the rest-mass density, $\mathbf{m} = \gamma^2 w \mathbf{v} + \mathbf{E} \times \mathbf{B}$ the momentum density, p the gas pressure, w the relativistic enthalpy and γ the Lorentz factor. $\mathbf{E}$, $\mathbf{B}$ and $\mathbf{v}$ are, respectively, the three–vectors representing the electric field, the magnetic field and the velocity, $u_{\text{em}} = (E^2 + B^2)/2$ and $\mathbf{I}$ is a 3×3 unit tensor. The electric field is determined by the ideal condition $\mathbf{E} + \mathbf{v} \times \mathbf{B} = 0$. We use an ideal equation of state, so that $w = \rho + \Gamma/(\Gamma - 1)p$. The units are chosen so that the speed of light $c = 1$ and a factor $\sqrt{4\pi}$ is reabsorbed in the definition of $\mathbf{E}$ and $\mathbf{B}$.

3

Magnetic Reconnection

Magnetic reconnection is a non-ideal phenomenon that occurs when two magnetic fluxes of opposite polarity encounter each other. The converging magnetic field lines annihilate at the discontinuity surface. The process dissipates the energy stored in magnetic field into plasma kinetic and thermal energy, through a rearrangement of magnetic field topology, resulting in particles heating and acceleration. MR is a natural tendency in a conductive fluid, a natural way to lower the magnetic energy stored in a system.

Historically MR studies have focused on laboratory experiments (Ji et al. 1998; Egedal et al. 2011, e.g.) and observations of the solar corona (e.g. Krucker & Battaglia 2013; Gary et al. 2018; Pontin & Priest 2022).

It is thought to play an important role in several different astrophysical sources, including pulsar wind nebulae (PWNe; Kirk & Skjæraasen 2003; Cerutti et al. 2014, 2020), GRBs (Zhang & Yan 2010; McKinney & Uzdensky 2011; Kumar & Zhang 2015) and coronae and jets in AGNs (Giannios et al. 2009; Nalewajko et al. 2011; Sironi et al. 2015; Davelaar et al. 2020; Nishikawa et al. 2020).

The phenomenon has been studied through theoretical models and Particles-in-a-cell (PIC) simulations, in which it is possible to follow the kinematics of all the particles and the development of the non-thermal spectra can be studied from first principles. The Chapter is organized as follow: in Sec. 3.1 the main theoretical models proposed historically to explain the reconnection rate are presented together with the spontaneous reconnection, while in Sec. 3.2 the main results from PIC simulations, with the

main focus on the plasma parameters necessary for the implementation of a sub-grid model in the PLUTO code (Mignone et al. 2007), are presented.

3.1 Magnetic reconnection models

The first theoretical models of MR where historically studied to explain the flares in the solar corona. The main quantity studied is the reconnection rate defined as the ratio between the inflow and outflow speeds. The observed temporal and spatial scales indicate a reconnection rate of the order $0.001 - 0.1$ the Alfvén rate, the Alfvén speed divided by the observed length scale. This corresponds to a Reynolds number (Sec. 2.3.2) for large-scale structures in the corona of the order of $10 - 1000$ (Dere 1996). The first reconnection models here presented had then as goal to estimate the reconnection rate based on plasma conditions and inflow quantities.

3.1.1 Sweet-Parker magnetic reconnection model

The Sweet-Parker model (Sweet 1958; Parker 1957) represents the stationary model describing MR. The model considers a two-dimensional, incompressible fluid. The velocity $\boldsymbol{v}$ and the magnetic field $\boldsymbol{B}$ have non-vanishing components in the (x, z) plane and an electric field $\boldsymbol{E}$ is directed along the $y-$axis. The magnetic field changes polarity along the $x-$axis (see Fig. 3.1) and at the center of the model a current sheet forms, where resistivity η (See Sec. 2.3.2 for a more detailed description of the role of resistivity) has to be considered and the plasma is not ideal anymore. The current sheet is described by its length L and thickness Δ, where $L \gg \Delta$, as shown in Fig. 3.1. Outside the resistive layer the plasma can be considered ideal as shown in Fig. 3.1 (effects of the η are negligible outside the current sheet). As a consequence the magnetic field lines outside this region will be convected towards the current sheet with the speed of the flowing plasma v_{in}.

The achievement of a stationary state requires a perfect agreement between the entrance speed of the inflow plasma and the velocity of diffusion and annihilation of the magnetic field lines in the current sheet. The requirement imposes a condition on the inflow velocity v_{in}. The diffusion velocity is instead dependent from the $\boldsymbol{B}$ gradient, roughly approximated as B_{in}/Δ, imposing limitations on the thickness Δ of the current sheet.

The model is defined by the inflow quantities v_{in} and B_{in}, the outflow ones B_{out} and v_{out}, where v_{out} is the velocity of the plasma leaving the diffusive layer, the magnetic diffusivity η and the characteristic dimensions of the current sheet L and Δ.
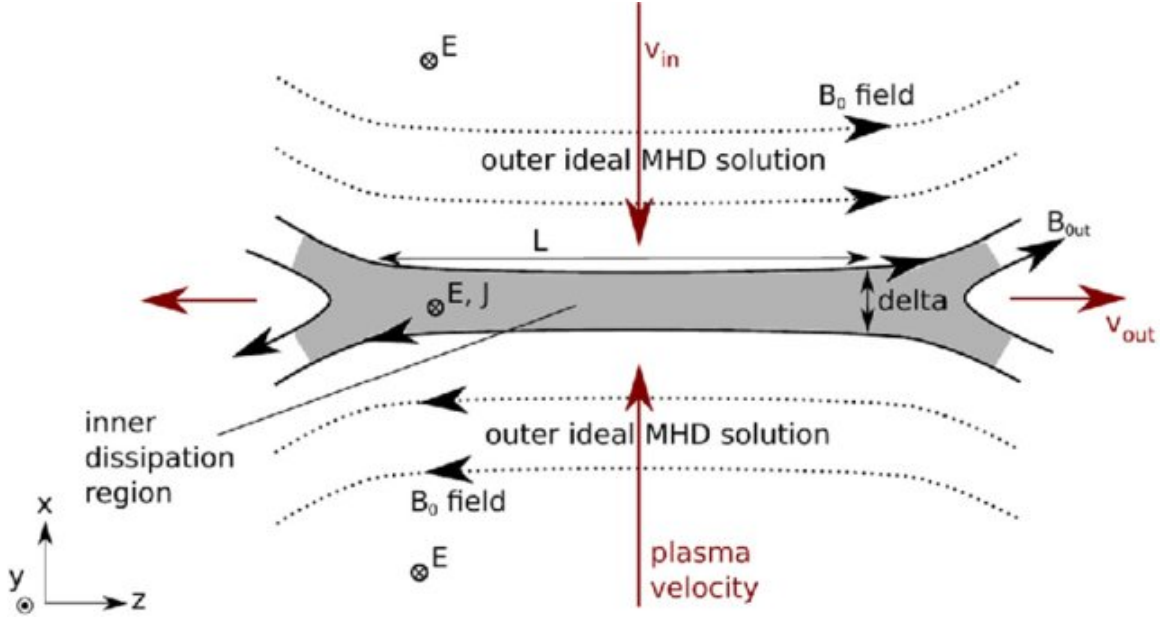
Figure 3.1: Sketch of the Sweet-Parker model. At the center the current sheet is represented as a grey box. The plasma moves toward the resistive layer with velocity v_i along the $x-$axis, while exits along the $z-$axis with velocity v_{out}. From Marcowith et al. (2020).

If the values of η, B_{in}, L are fixed, it is possible to derive the dependence of the other quantities using the equations for mass and flux conservation. The relations that are obtained reads as:

$$v_{\text{in}} = \frac{\eta}{\Delta} \qquad \Delta = L\frac{v_{\text{in}}}{v_{\text{out}}} \qquad B_{\text{out}} = B_{\text{in}}\frac{v_{\text{in}}}{v_{\text{out}}} = B_{\text{in}}\frac{\Delta}{L} \; . \tag{3.1}$$

All the quantities can be written as function of the outflow velocity v_{out}. Using the Lorentz force v_{out} can be estimated as:

$$v_{\text{out}} = \frac{B_{\text{in}}}{\sqrt{4\pi\rho}} \equiv c_{ai} \; , \tag{3.2}$$

where c_{ai} is the Alfven speed of the incoming flux. As already mentioned, the ratio between the inflow and outflow speed is know as reconnection rate R_i and for the Sweet-Parker model is evaluated as:

$$R_i = v_{\text{in}}/c_{ai} \sim S^{-1/2} \; , \tag{3.3}$$

where S is the Lundquist number (Sec. 2.3.2). Similarly, the reconnection velocity, defined as the velocity v_{in} of the inflow plasma, is $v_R \sim c_{ai}S^{-1/2}$.

The rate predicted by the Sweet Parker model is not fast enough when compared with observations. It can lead to a reconnection event, but a stationary model is not able to
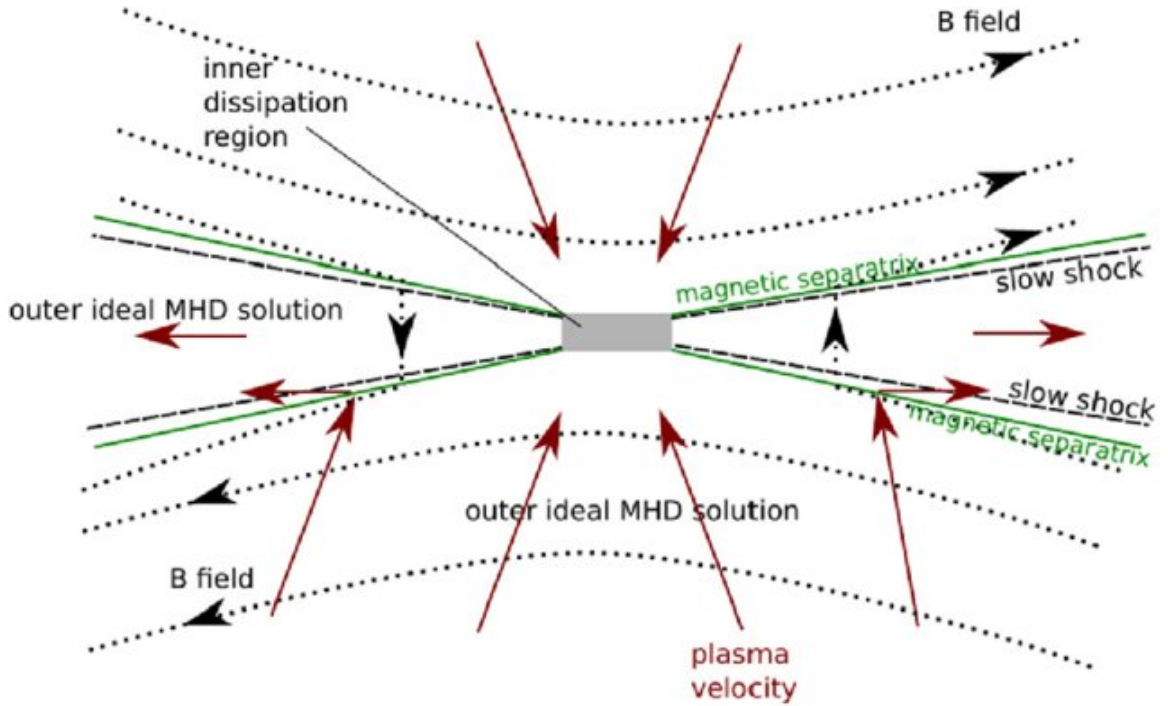
Figure 3.2: Sketch of the Petschek model. At the center the current sheet is represented as grey box. The plasma moves toward the resistive layer along the $y-$axis, while it exits along the $x-$axis. Slow shocks are formed in the region surrounding the sides of the reconnection region (Marcowith et al. 2020).

explain the reconnection rates that are observed in the solar corona. The total energy released in a solar flare can release up to 10^{32} erg, in few hours, with reconnection rate of the order $0.001-0.1$ the Alfvén rate (Isobe et al. 2002). Observations indicate that most of the energy is released during the initial phase of the flare (order of minutes) and the only available source of this amount of energy is the magnetic field. Some modifications in the geometry or in the stationary hypothesis of the Sweet-Parker model is required to match the observations.

3.1.2 Petschek magnetic reconnection model

A different geometry of the reconnection site with respect to the Sweet-Parker model introduced in Sec. 3.1.1 is the Petschek model. The Sweet-Parker model describes only the region close to the diffusive layer. At the same time the quantities taken into account to model the reconnection rate comes from a larger region surrounding the layer. It is natural to extend the model to a larger portion of plasma around the current sheet. The model assumes a 2D geometry in which the reconnection is now supposed to happen in a region that can considered as a single point with respect
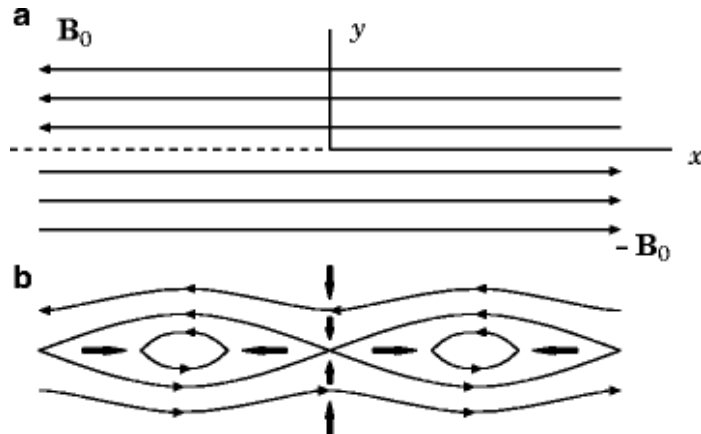
Figure 3.3: Evolution of tearing instabilities in a current sheet.

to the macroscopic scale of the system (Fig. 3.2). The central idea is to observe that we can have a plasma entering a diffusive region with a velocity larger than the characteristic velocity of the system. This can produce slow shocks and the dissipation can take place in the diffusive region as well as on the shock fronts, increasing the efficiency of the energy conversion.

The configuration results in a faster reconnection speed:

$$v_R \sim \frac{\pi}{8} \frac{v_A}{lnS} \ .$$
(3.4)

S in the equation is determined with the external values far from the current sheet, key point of this reconnection model. The main problem has been shown by numerical simulation results: the geometry described is not stable and rapidly collapses to the Sweet-Parker model.

3.1.3 Spontaneous reconnection

Both the Sweet Parker and the Petschek models suppose that somehow at the beginning an initial plasma flow towards the resistive layer is present. Alternatively, it is natural to ask whether reconnection can occur as a spontaneous process instead. An initial homogeneous current sheet, in fact, will tend to evolve in a series of current filaments. Resistive instabilities can develop, in particular the Tearing Mode instability (Furth et al. 1963; Rutherford 1973; Coppi et al. 1976). It is driven by the non-uniformity of the magnetic field, that tries to relax to a lower energy state. This instability can give rise to spontaneous reconnection events. Resistive instabilities have timescales intermediate between the resistive diffusion (very slow) and the ideal

MHD (very fast), $\tau_f \ll \tau \ll \tau_d$ (Sec. 2.3.2). In particular for the Tearing mode instability:

$$\tau \simeq \tau_d S^{2/5}(kL)^{-2/5} \ , \tag{3.5}$$

where L is the size of the system and k is the wave number. The resulting reconnection rate is higher with respect to the Sweet Parker configuration (Sec. 3.1.1).

An unperturbed state is assumed with a magnetic field:

$$\mathbf{B}_0 = B_{0x}(y)\mathbf{e}_x + B_{0z}\mathbf{e}_z \ , \tag{3.6}$$

where $B_{0x}(0) = 0$, $B_{0x}(\pm\infty) = B_0$ and for simplicity B_{0z} is constant. There is no initial velocity field and the density value ρ is assumed constant. The tearing instability develops when perturbing such a system with magnetic and velocity field perturbations, given as:

$$\mathbf{B}_1 = B_{1x}(x,y)\mathbf{e}_x + B_{1y}(x,y)\mathbf{e}_y \quad \mathbf{v}_1 = v_{1x}(x,y)\mathbf{e}_x + v_{1y}(x,y)\mathbf{e}_y \ . \tag{3.7}$$

Due to the tearing instabilities a component $B_{1y} \neq 0$ rises, as expected during MR. This magnetic field component drags the initial magnetic field $\mathbf{B}_0$ towards the dissipative region at $y = 0$. The velocity flow due to the instability in the v_y component goes as well towards the same region. Additionally the magnetic field component B_{0z} has no influence in the development of the tearing instability.

A sketch of the evolution of the tearing instabilities is represented in Fig. 3.3. The initial unperturbed magnetic field is represented in the upper panel. In the lower panel the magnetic field lines, results of the instability, are represented. Due to the perturbations, the current sheet fragments in islands (the region with closed magnetic field lines at the side of the bottom panel) and x-points, region in which the magnetic field lines annihilates. The process can further develop, with the current sheet that can further fragment at smaller scales. As it will be shown soon, the development of tearing instabilities is what is observed during PIC simulations. Current sheets in the Sweet Parker configuration appear to be unstable to tearing instabilities (Loureiro et al. 2005; Bárta et al. 2011).

3.2 Main results on particles acceleration

In order to study a phenomenon complex as the MR appears to be, simulations starting from plausible initial conditions are required. The more consistent way to
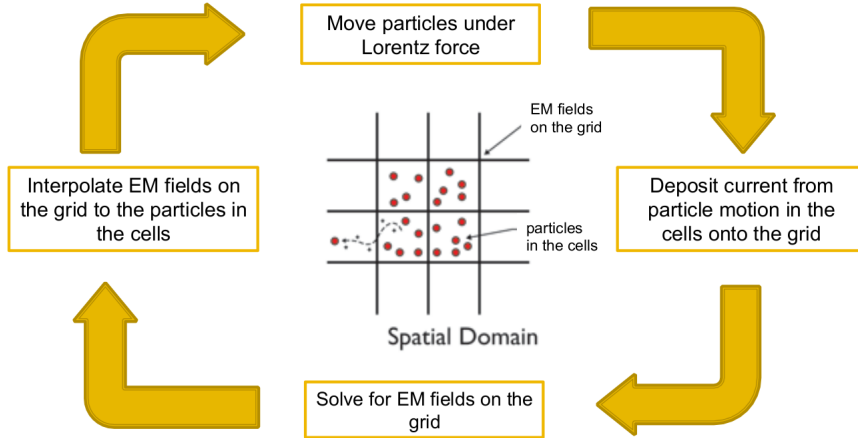
Figure 3.4: Schematic view of a PIC solver.

study all the details of reconnection such as the final spectra of accelerated particles, the energy that is released and the acceleration mechanism, is with PIC simulations. They allow to follow the position and the energy of the particles in a consistent way with the fluid evolution, with a kinetic approach to the MR problem. A sketch of how PIC simulations work is shown in Fig. 3.4. In each step during the temporal evolution of the system, the electric and magnetic fields are defined on a static spatial grid and evolved with Maxwell equations (Eq. 2.1). The particles are instead able to move freely on the domain and they evolve according to the Lorentz force, with the quantities needed interpolated from the grid quantities at their positions. The current from the particles is then deposited in the cell in which they are located and the next step of evolution of magnetic and electric field can start again.

As PIC codes need to resolve the (temporal and spatial) dynamic scales of individual particles, the physical size of the domains and the timescales in which the PIC can be used is restricted by the plasma skin depth and the plasma frequency of the particle species that the simulation wants to study. PIC simulations are then necessarily focused on the microscopic scale of MR phenomenon and their temporal and spatial domain are limited with respect to MHD simulations.

3.2.1 Development of a non-thermal spectrum

The energy released by the reconnection of the magnetic field lines can have many effects on the system. The temperature of the fluid increases and, of main interest for the astrophysical implications, a non-thermal spectrum can develop, in the shape of a power-law governed by the initial plasma conditions around the current sheet.
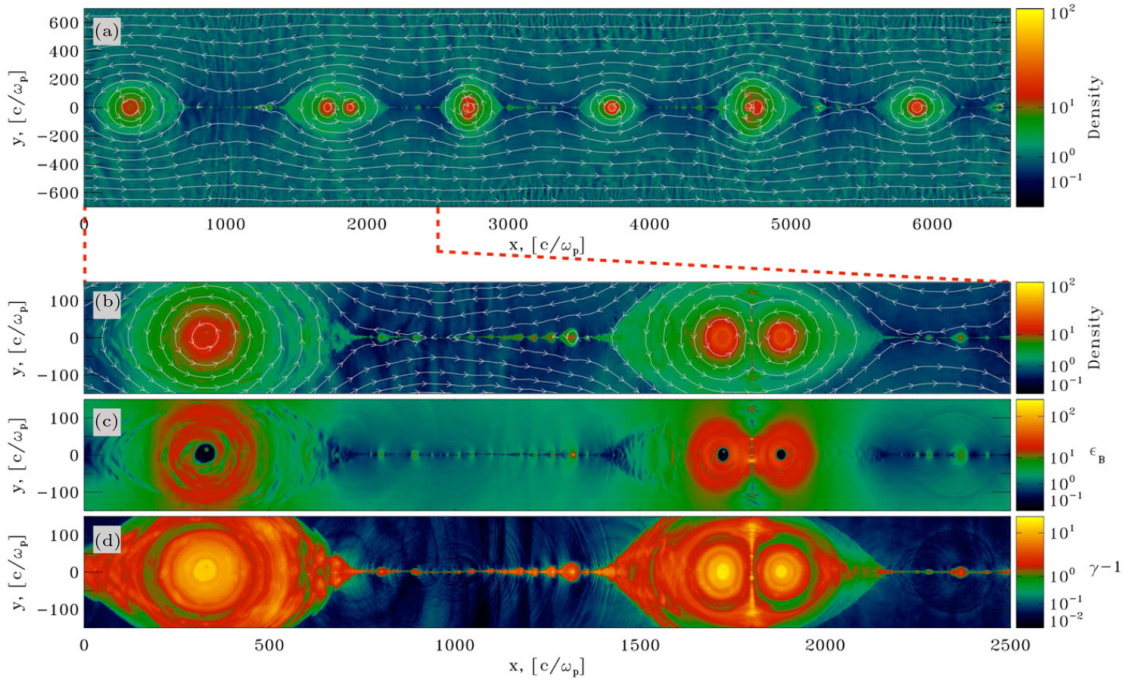
Figure 3.5: Reconnection layer from a 2D PIC simulation with initial value of $\sigma = 10$ from Sironi & Spitkovsky (2014) at $\omega_p t = 3000$. In the top panel the colormap represents the density of the fluid, while the lines represent the magnetic field, of opposite polarity along the $y-$axis. In the three bottom panels a zoom of the magnetic islands structure $x \in [0, 2500]\, c/\omega_p$ is presented. The three colormaps represent respectively the density together with the magnetic field lines, the magnetic energy fraction $\epsilon_B = B^2/8\pi mnc^2$ and the mean kinetic energy per particle.

The particle spectrum resulting from MR has been indeed extensively studied in a fully kinetic framework with PIC simulations, both in a pair plasma (Zenitani & Hoshino 2001, 2005, 2008; Guo et al. 2014; Jaroschek et al. 2004; Sironi & Spitkovsky 2014; Guo et al. 2015; Sironi et al. 2016; Werner et al. 2015; Petropoulou & Sironi 2018; Werner & Uzdensky 2021; Zhang et al. 2021), in a ion-electron (Melzani et al. 2014; Guo et al. 2016; Werner et al. 2017; Ball et al. 2018; Li et al. 2019; Kilian et al. 2020) and in the pair-ion one (Petropoulou et al. 2019).

The main difficulty of considering ion and electrons in PIC simulations is due to the different skin depth of the two species, that require very high spatial and temporal resolutions to catch the details of both species.

The setup normally used in order to study MR in PIC simulations is the so called Harris current sheet. In the 2D version of this setup the magnetic field is defined as $\boldsymbol{B} = -B_0 \tanh(y/\Delta)\hat{\mathbf{x}}$, where B_0 is the intensity of the reconnecting magnetic field and Δ represents the thickness of the current sheet.

A snapshot of the evolution of a current sheet layer is shown in Fig. 3.5 from Sironi &

31
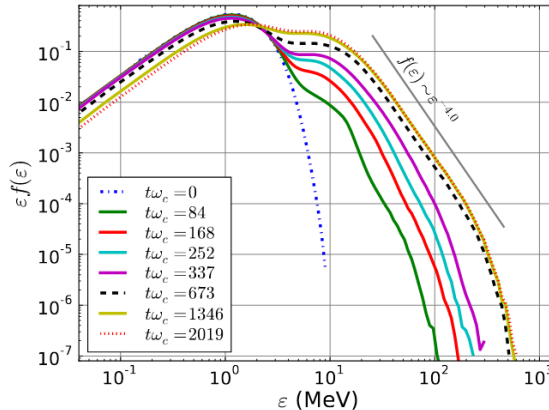
Figure 3.6: Time evolution of the electron spectrum (represented as $\epsilon f(\epsilon)$) during a 2D PIC simulation of a current sheet with initial ion-magnetization $\sigma_{\mathrm{i}} = 0.1$ from Werner et al. (2017). Different times during the simulation are shown with different colors as shown in the legend. The black solid line represents a power-law with index $p = 4$ as developed by the particles at the end of the simulation.

Spitkovsky (2014). During the time evolution the initial thin current sheet fragments in the so called plasmoids, regions with higher density. An example is the big magnetic island at $x \sim 400 c/\omega_p$ in Fig. 3.5. Fig. 3.5 is a good representation of the realization of tearing mode instabilities (3.1.3) in MR simulations. Looking at the top panel a series of magnetic island (or plasmoids) is visible, with x-points between them, similarly to the sketch of Fig. 3.3. Zooming in between two magnetic islands reveals the small scale structure of the problem. The plasma between two magnetic islands is fragmented in other smaller islands and x-points. The particles are accelerated both by the electric field generated during the reconnection and by the fragmentation of the current sheet and subsequent merging of magnetic islands (Guo et al. 2019). The magnetic energy is released mainly in the magnetic islands, as it can be seen from the panel (c) in Fig 3.5, where the magnetic energy fraction ϵ_B reaches the lowest values and at the same time in panel (d) it is possible to observe that the same regions are the ones on which the particles have achieved the highest values of kinetic energy.

A typical time evolution of a particles spectrum during a MR event is represented in Fig. 3.6 from Werner et al. (2017). The particles are initially distributed following a thermal behaviour. While MR occurs, the temperature of the distribution increases and a non-thermal component with a power-law tail starts to develop. The final spectrum has clearly a non-thermal component with a power-law shape and the acceleration saturates, with the maximum energy reaching a final value around $t\omega_c \simeq 1300$.

The feasibility to study in details the different final spectra depending on the plasma conditions with PIC simulations opens the possibility to develop a phenomenological model of the final results of particles acceleration due to MR. The Harris setup is an idealized version of what is expected to be found in astrophysical environments, where current sheets generated by the evolution of the plasma may significantly change from this picture, but it allows to define what are the initial conditions of the system and to study the different final spectra in a wide range of plasma parameters. Having a model based on PIC results would allow to implement in (R)MHD codes (see Chap. 2 for a description of the main characteristic of this methodology) a sub-grid model based on the plasma conditions of the region surrounding the current sheets.

In the following section weare going to take into exams what are, according to PIC results, the chief parameters required to have a full descriptions of the final accelerated spectra.

3.2.2 Modeling the accelerated spectrum: the plasma chief parameters

3.2.2.1 Magnetization σ

The first parameter that immediately has been taken into account in the PIC studies is the cold magnetization σ. For the species i it is defined as:

$$\sigma_i = B^2/4\pi n_i m_i c^2 \ , \tag{3.8}$$

quantifying the ratio between magnetic energy density and rest mass energy density in the system.

The development of a MR event requires that the system is initially energetically dominated by the magnetic energy. More powerful reconnection events can be then naturally expected in current sheets where the surrounding medium has higher values of σ_i.

The correlation of the maximum spectral energy and the power-law slope with different initial σ_i values has been observed in the final spectra by many PIC studies. Various regimes of reconnection are usually defined for different ranges of σ_i. If $\sigma_i \ll 1$ the regime is defined non-relativistic, since the magnetic energy is subdominant with respect to the rest mass in the system. For $\sigma_i \sim 1$ the transrelativistic regime is reached. The magnetic energy in the system reaches similar values of the rest mass and the system can be considered in equipartition. Finally for $\sigma_i \gg 1$ the magnetic energy is clearly the dominant energy of the system and this regime is called (ultra)
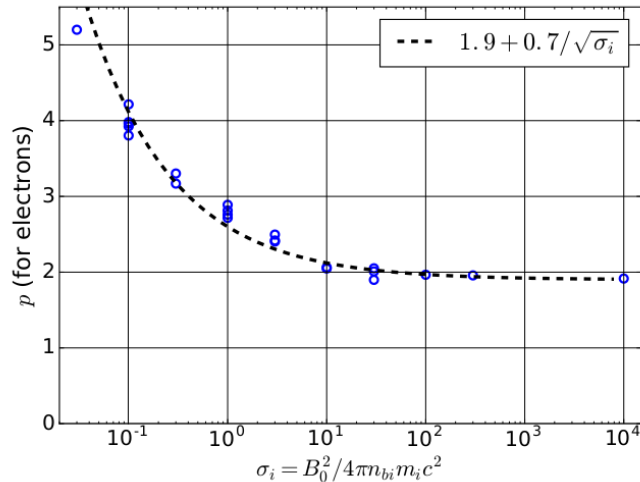
Figure 3.7: Power-law index p of the electron distribution as a function of σ_i as found in Werner et al. (2017). The dashed line represents the best fit for the blue points, results of PIC simulations with different initial σ_i values.

relativistic reconnection, with the more powerful acceleration phenomenon happening in this last regime.

In Werner et al. (2017) a systematic study of the dependency of the characteristic of the final spectra of electron has been carried out, in a proton-electron plasma. The σ_i here discussed refers to the proton species. The final power-law index shows a dependency on σ_i as represented in Fig. 3.7. As expected in the non-relativistic regime the index is very steep, while going towards higher values of σ_i the index approaches a asymptotic value $p \sim 1.9$. The relation found for the best fit obtained with data from PIC simulation is expressed as:

$$p = 1.9 + 0.7/\sqrt{\sigma_i} \ . \tag{3.9}$$

The $\sigma_i^{-1/2}$ scaling of the electron power-law index p can be understood within the framework of stochastic second-order Fermi acceleration of ultrarelativistic electrons bouncing back and forth between plasmoids moving randomly along the reconnection layer. λ_{pl} is the typical separation between plasmoids and v_{pl} their typical speed, of the order of c_a Alfven velocity, $c_a \ll c$ in the semirelativistic regime. The average energy gain per bounce is:

$$\Delta \varepsilon \sim (v_{pl}/c)^2 \varepsilon \ . \tag{3.10}$$

34

The time between bounces is $\Delta t_b \sim \lambda_{lp}/c$ and so the acceleration timescale is:

$$t_{acc} = \varepsilon \Delta t_b / \Delta \varepsilon \propto c\lambda_{pl}/v_{pl}^2 . \tag{3.11}$$

The escape time can be extimated as the time necessary for two plasmoids to approach each other:

$$t_{esc} \sim \lambda_{pl}/v_{pl} . \tag{3.12}$$

For a second-order Fermi acceleration process the power-law index should scale as:

$$p = 1 + t_{acc}/t_{esc} = 1 + \text{const } c/v_{pl} . \tag{3.13}$$

Having $v_{lp} \simeq c_a \simeq c\sigma_i^{1/2}$ for $\sigma_i \ll 1$ the general form that we obtain for the power-law index is consistent with the numerical findings of Eq. (3.9).

The maximum energy ϵ_c (defined as cut-off energy of the power-law spectra) obtained by the accelerated particles shows as well a dependency on σ_i that can be expressed as:

$$\epsilon_c = 4\sigma_e m_e c^2 , \tag{3.14}$$

where σ_e is the magnetization of the electron species that is related to the proton one by $\sigma_e = \mu\sigma_i$, with $\mu = m_p/m_e$. This cut-off energy could eventually be overcome by additional acceleration that has been recently observed in 3D PIC simulations (Zhang et al. 2021) and the possibility to model an additional higher-energy tail of the spectra has to be taken into consideration.

Werner et al. (2017) found as well that the fraction of energy, defined as q_e, that in MR is gained by the electron population has a dependency on σ_i. The dependency can be expressed as:

$$q_e = \frac{1}{4} + \frac{1}{4}\sqrt{\frac{\sigma_i/5}{2 + \sigma_i/5}} \tag{3.15}$$

and the best fit and the comparison with results from PIC simulations is shown in Fig. 3.8. While in the non-relativistic to the transrelativistic regime we have $q_e < 0.5$, with the proton component taking the majority of the available energy, in the relativistic regime $q_e \sim 0.5$. This equipartition between the two different species is reached because in the relativistic limit the available magnetic energy is so high that the difference in mass between the two species becomes negligible and the reconnection can be considered happening in an similar way for electrons as well as protons.
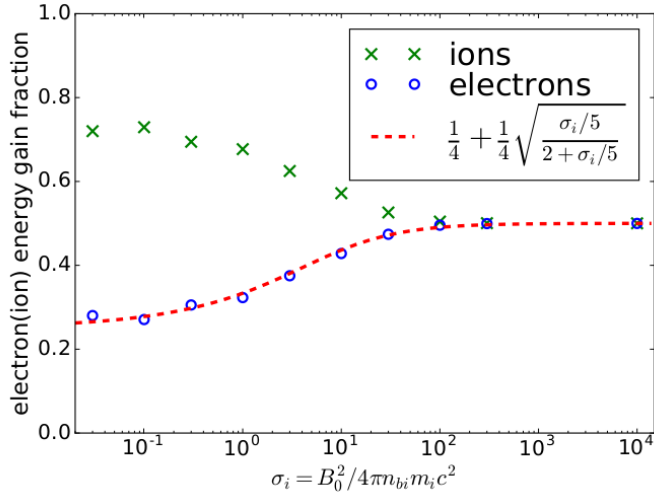
Figure 3.8: Fraction of energy gained by the electron population from the total energy available in a reconnection event as function of the magnetization σ_i as found in Werner et al. (2017). The blue symbols represent the energy fraction gained by the electrons as found in the PIC simulations, while the green dots represent the fraction for the proton population. The red dashed line is the best fit obtained for the electron fraction.

3.2.2.2 β parameter

In order to have a complete picture of the acceleration due to MR based on the characteristics of the surrounding plasma to consider only σ_i is not enough. An additional plasma parameter that PIC studies have taken into account is the plasma β_i, representing the proton β parameter, the thermal to magnetic pressure ratio (see Sec. 2.3.1 for more details). By taking into account the dependency from both these parameters, the phenomenological model describing the final spectra due to RM can be described as follow.

The power-law index can be modelled as shown in Fig. 3.9 (Ball et al. 2018):

$$p(\sigma_i, \beta_i) = A_p + B_p \tanh\left(C_p \beta_i\right) \ , \tag{3.16}$$

where:

$$A_p = 1.8 + 0.7/\sqrt{\sigma_i} \, , \quad B_p = 3.7\sigma_i^{-0.19} \, , \quad C_p = 23.4\sigma_i^{0.26} \ . \tag{3.17}$$

The expression for A_p has the dependency from σ_i as the one found in Werner et al. (2017) and B_p and C_p become negligigle for the β range that has been considered in Werner et al. (2017). This means that when considering β_i low enough ($\beta_i < 3 \times 10^{-3}$), we recover the same results found when considering the σ_i parameter only. This fit

36
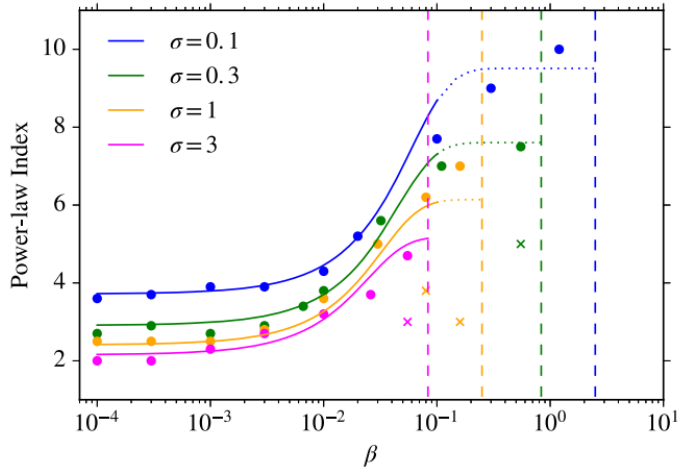
Figure 3.9: Characterization of the power-law index of the final electron spectra as a function of σ_i and β_i. The dots represent different results from PIC simulation, while the solid lines are the best fit obtained for different values of β_i at fixed σ_i value (Ball et al. 2018).

is robust for $\beta_i < 0.1$ and can be eventually pushed in modelling the final spectra up to $\beta_i \sim 0.5$.

It is possible to quantify the efficiency of the non-thermal electron spectrum with respect to the Maxwellian for $\gamma > \gamma_{pk}$ normalized to the overall energy content of the spectrum, by defining the acceleration efficiency ϵ_{acc} as:

$$\epsilon_{acc} = \frac{\int_{\gamma_{\mathrm{pk}}}^{\infty} (\gamma - 1) \left[\frac{dN}{d\gamma} - f_{\mathrm{MB}}(\gamma) \right] d\gamma}{\int_{\gamma_{\mathrm{pk}}}^{\infty} (\gamma - 1) \frac{dN}{d\gamma} d\gamma} \ , \tag{3.18}$$

where f_{MB} represents the Maxwell-Boltzmann distribution identified as the thermal component of spectra. The acceleration efficiency ϵ_{acc} can be fitted, as shown in Fig. 3.10, by the empirical formula:

$$\epsilon_{acc} = A_\epsilon + B_\epsilon \tanh\left(C_\epsilon \beta_i\right) \ , \tag{3.19}$$

where:

$$\begin{aligned} A_\epsilon &= 1 - \frac{1}{4.2\sigma_i^{0.55} + 1} \ , \quad B_\epsilon = 0.64\sigma_i^{0.07} \\ C_\epsilon &= -68\sigma_i^{0.13} \ . \end{aligned} \tag{3.20}$$

By considering both σ_i and β_i around a reconnection site we have all the ingredients that are needed to develop a sub-grid model able to describe the final spectra due to MR in MHD simulations, in which a determination of the spectra would be otherwise
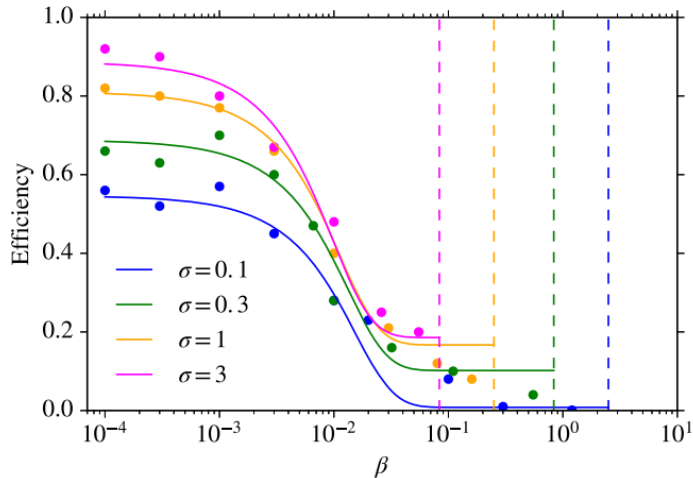
Figure 3.10: Characterization of the acceleration efficiency ϵ_{acc} defined in Eq. (3.18) of the final electron spectra as a function of σ_i and β_i. The dots represent different results from PIC simulation, while the solid lines are the best fit obtained for different values of β_i at fixed σ_i value (Ball et al. 2018).

impossible to achieve when the domains taken into account would be of astrophysical scales.

3.2.2.3 Guide field

The power-law behaviour of spectra due to MR acceleration may depends on the presence of a guide field. A guide field is defined as the component of magnetic field that has no inversion trough the current sheet. Guide fields may be present in astrophysical environments if a large scale magnetic field structure is present.

In Werner & Uzdensky (2017) the role of a guide field has been studied in 3D pair plasma simulations. It results that strong guide field fraction B_{gz}/B_0, where B_{gz} is the guide field and B_0 the total magnetic field, can significantly inhibit the non-thermal particle acceleration. The effect of the guide field is to reduce the effective hot magnetization (Werner & Uzdensky 2017):

$$\sigma_{h,\text{eff}} = B_0^2 / \left(4\pi h + B_{gz}^2 \right) \ . \tag{3.21}$$

For modest values of the guide field $B_{gz} \lesssim B_0/4$ there is almost no effect, while strong guide fields $B_{gz} \gtrsim B_0$ can suppress particle acceleration, yielding to steeper spectra as show in Fig. 3.11 (left panel).

An empirical fit for the role of the guide field, parameterized trough the effective of magnetization of Eq. (3.21), is shown in Fig. 3.11 (right panel). The plot shows how an ultra-relativistic reconnection event ($\sigma_i = 2.74 \times 10^4$ in the plot) reaching, when
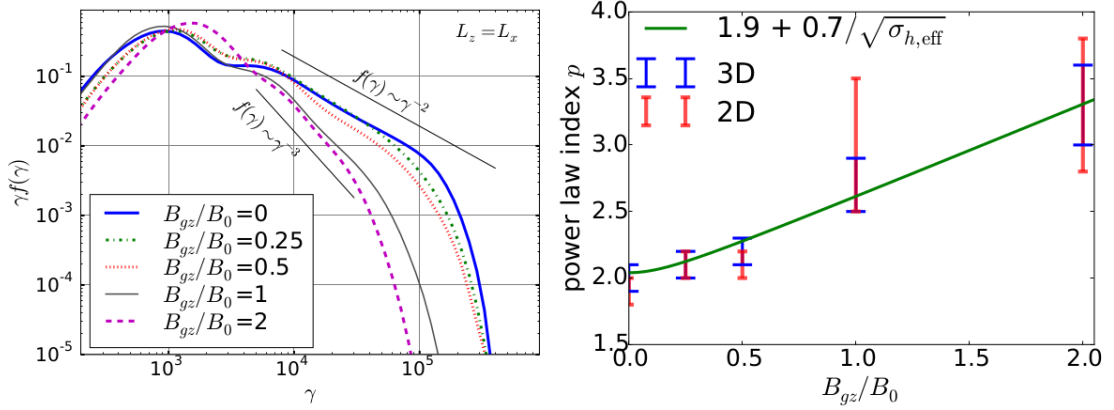
Figure 3.11: Left: Power-law behaviour for different B_{gz} fraction. Right: empirical fit for the dependency of the power-law index of accelerated spectra as function of the effective hot magnetization (green line) Werner & Uzdensky (2017). The red and blue error bars represent the power-law index found respectively in the 2D and 3D simulations.

no guide field is present, the asymptotic power-law index $p \sim 1.9$ as predicted by Eq. (3.16). By increasing the ratio of guide field with respect to the total magnetic field the power-law index increases. The dependency of the power-law index as function of $\sigma_{h\,\mathrm{eff}}$ (Eq. 3.21) is represented as green line.

Despite the big errors in the determination of the power-law index for high values of $\sigma_{h\,\mathrm{eff}}$, including the effects of the presence of a significative guide field in a sub-grid model for MR appears to be important.

4

Current sheet identification

The PIC results describing evolution or MR allow to develop a sub-grid model in (R)MHD simulations able to model the post-MR spectra of non-thermal particles. In this chapter I will describe the first step toward the description of the acceleration of particles due to magnetic reconnection in large scale simulations: the identification of the current sheet, sites in which the acceleration happens. I will introduce a new algorithm able to determine on the fly during (R)MHD simulations if a cell can be identified as reconnection site.

The chapter is organized as follows: in Section 4.1 the current sheet detector algorithm and its validation are presented and in Section 4.2 the newly introduced method is applied to a steady state current sheet setup.

4.1   Current-sheet detector

Magnetic reconnection is thought to take place in current sheets, thin layers with high values of the current density, $\mathbf{J} = c/4\pi \nabla \times \mathbf{B}$ (in the static case). Idealized current sheet configurations have been extensively adopted by PIC and MHD studies, typically in the form of a Harris current sheet (see Sec. 3.2.1 for its description). However, when current sheets form dynamically as byproducts of plasma instabilities, more irregular shapes can be expected that can significantly differ from the idealized profile.

For these reasons I now propose an algorithm to identify localized plasma region where reconnection may take place. In particular, I aim at: i) improving the computational speed to identify current sheets at runtime during large-scale simulations; ii) tracing information on the physical parameters (to be subsequently employed in particle spectral update) in complex structures. While other methods exist in literature, they are either complex to be extended to a 3D time-dependent simulation because based on the vector potential **A** (Servidio et al. 2010) or they rely on the definition of an average value of **J** on the domain (e.g. Zhdankin et al. 2013, 2015; Kadowaki et al. 2018) that can be problematic when considering very inhomogeneous situations, such as that of a jet propagating into an external environment with very different properties. Besides, these methods additionally identify a current sheet by clustering adjacent cells, part of the same acceleration site. This provides more information about the global characteristic of the reconnection region, but requires extra computational time to be performed.

The newly proposed algorithm follows from Mignone et al. (2012) (see, in particular, Sec. 5.3 of their paper) and flags as reconnection sites cells that satisfy the following condition (in the 2D Cartesian case):

$$\chi = \frac{|\Delta_{\mathrm{x}} B_{\mathrm{y}} - \Delta_{\mathrm{y}} B_{\mathrm{x}}|}{|\Delta_{\mathrm{x}} B_{\mathrm{y}}| + |\Delta_{\mathrm{y}} B_{\mathrm{x}}| + \sqrt{\rho}} > \chi_{\min} \,, \tag{4.1}$$

where $\Delta_{\mathrm{x}} B_{\mathrm{y}}$ and $\Delta_{\mathrm{y}} B_{\mathrm{x}}$ are undivided central differences and $\chi_{\min}$ is a free parameter. The parameter χ gives a measure of the magnetic field gradient and it is here computed by performing finite differences on adjacent cells, making it computationally less expensive and more efficient in parallel computation with respect to the other method already cited. Its computation also does not need the definition of a region over which average quantities are evaluated as in Zhdankin et al. (2013), leaving $\chi_{\min}$ as the only problem-dependent parameter.

Eq. (4.1) can be extended to the 3D Cartesian case. Numerator and denominator of Eq. (4.1) become respectively, in this case,

$$|\Delta_{\mathrm{x}} B_{\mathrm{y}} - \Delta_{\mathrm{y}} B_{\mathrm{x}}| + |\Delta_{\mathrm{x}} B_{\mathrm{z}} - \Delta_{\mathrm{z}} B_{\mathrm{x}}| + |\Delta_{\mathrm{y}} B_{\mathrm{z}} - \Delta_{\mathrm{z}} B_{\mathrm{y}}| \tag{4.2}$$

and

$$|\Delta_{\mathrm{x}} B_{\mathrm{y}}| + |\Delta_{\mathrm{y}} B_{\mathrm{x}}| + |\Delta_{\mathrm{x}} B_{\mathrm{z}}| + |\Delta_{\mathrm{z}} B_{\mathrm{x}}| + |\Delta_{\mathrm{y}} B_{\mathrm{z}}| + |\Delta_{\mathrm{z}} B_{\mathrm{y}}| + \sqrt{\rho} \,, \tag{4.3}$$

respectively.

4.1.1 Method comparison and verification

In order to verify our method, I first compare my results with those obtained by adopting the method proposed by Zhdankin et al. (2013). I remind the reader that Zhdankin's algorithm identifies current sheet regions in MHD snapshots through local maxima of the current density $\mathbf{J}$. After the evaluation of the average value of the current density $\langle|\mathbf{J}|\rangle$, cells with $\mathbf{J}|_{ijk} > n\langle|\mathbf{J}|\rangle$ are selected as candidate current sheet cells, where n is a free parameter of the algorithm.

To compare the two methods, I perform 2D MHD simulations of a Kelvin-Helmholtz instability (KHI) naturally producing current sheets. The domain consists of a 2D rectangular box of size $L \times L/2$, where $L = 2c/\omega_{\mathrm{p}}$, with a resolution of 512×256 grid points. The velocity has a profile $v_{\mathrm{x}} = 0.5\,v_0\mathrm{sign}(y)$, where $v_0 = 0.1$ is the shear velocity. The instability is triggered by perturbing the y-component of velocity, $v_{\mathrm{y}} = r\,v_0\exp(-50\,y/L_{\mathrm{y}})$, where $L_{\mathrm{y}} = L/2$ is the vertical size of the computational box and r is a random number in the range $[-10^{-2}, 10^{-2}]$. The initial density is $\rho_0 = 1$ and the magnetic field is set as $B_0 = 0.1\sqrt{\rho_0 c_{\mathrm{s}}^2}$, where the sound speed $c_{\mathrm{s}} = v_0 = 0.1$. The magnetic field is at $t = 0$ along the $x-$axis, $\mathbf{B} = B_0\hat{x}$. The pressure is set as $p = c_{\mathrm{s}}^2\rho_0/\Gamma$, where $\Gamma = 5/3$ is the adiabatic index. Boundary conditions are periodic on the x direction and outflow elsewhere.

The comparison between the two methods has been carried out in post-processing by varying χ_{min} and n and computing the number of flagged zones common to both algorithms. The average value of $\mathbf{J}$, required in the method by Zhdankin et al. (2013), is evaluated over the whole domain.

Fig. 4.1 shows the results of the best agreement (maximum overlapping, with $\approx 96\%$ of points found by the two algorithms), which is obtained at $t = 1.2 \times 10^6\omega_{\mathrm{p}}^{-1}$ when $\chi_{\mathrm{min}} = 0.006$ and $n = 21.6$, supporting the effectiveness of our algorithm. It has to be noticed that the average value of $\mathbf{J}$ over the whole domain greatly changes during the time evolution and the comparison with the method proposed by Zhdankin et al. (2013) can be performed only for a specific time. At a previous time $t = 10^6\omega_{\mathrm{p}}^{-1}$, for example, the maximum overlapping ($\approx 95\%$) is achieved with $\chi_{\mathrm{min}} = 0.006$ and $n = 16$, due to the earlier development of the KHI.

As done in Zhdankin et al. (2013), I want to check in post-processing that the current sheets found by the algorithm are regions in which an inversion of the magnetic field components parallel to the sheet is actually present. To this end, I estimate the direction normal to the current sheet by using $\nabla|\mathbf{J}|$ as a proxy. I pick the value of $\nabla|\mathbf{J}|$ in the cell in which $|\mathbf{J}|$ is largest among those of the same current sheet. The
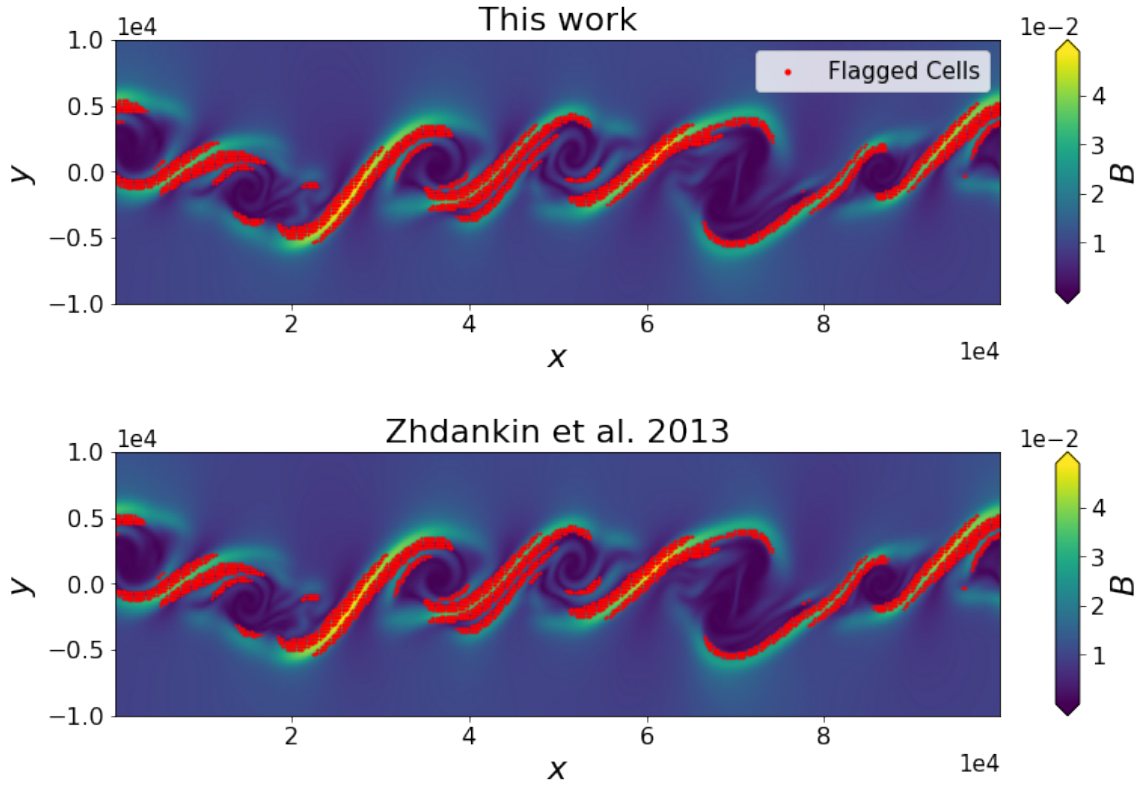
Figure 4.1: Comparison of the results of the current sheet detection method described in section 4.1 (top panel) and that described in Zhdankin et al. (2013) (bottom panel) at $t = 1.2 \times 10^6 \omega_p^{-1}$. The color plots show the magnetic field B and the red dots represent points flagged as current sheets regions.
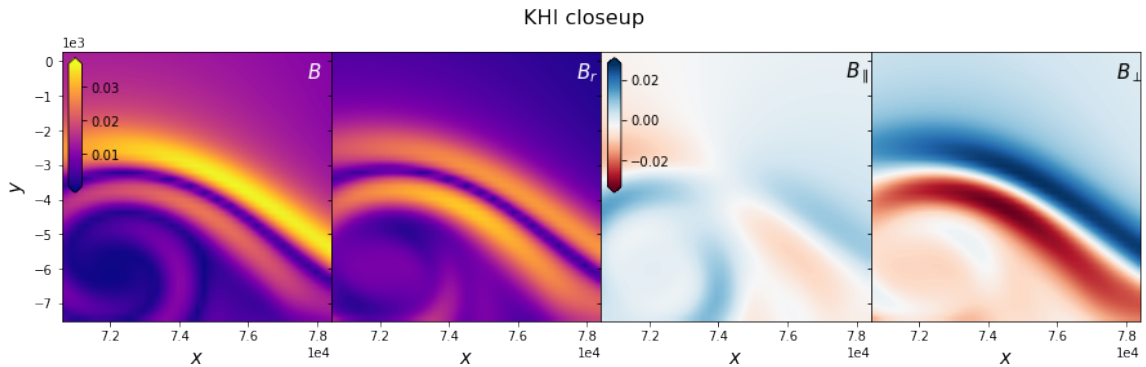
Figure 4.2: Total and reconnecting magnetic field intensities in the KHI problem (zoom on a smaller domain patch). From left to right: The 1st and 2nd panels represent, respectively, the magnetic field $|\boldsymbol{B}|$ around a current sheet (identified via Eq. 4.1) and the reconnecting magnetic field $|\boldsymbol{B_r}|$ after the subtraction of the guide field. The 3rd and 4th panels show the parallel $|\boldsymbol{B_r}|$ and perpendicular components to $\nabla \boldsymbol{J}$, respectively.

evaluation of the cell where to evaluate $\nabla|\mathbf{J}|$ has been performed by using a similar approach to what has been done in Zhdankin et al. (2013), where, after the selection of the cells in which $|\mathbf{J}|_{ijk} > n\langle|\mathbf{J}|\rangle$, the local maximum is found as maximum in a $7 \times 7 \times 7$ cube. This allows to have a reliable estimate of the vector perpendicular to the current sheet in its most dissipative regions. I estimate the guide field $\mathbf{B}_\mathrm{g}$ as the average value of the magnetic field components in a box of 21×21 cells size. This region has been defined "ad hoc" for this problem in order to include the entire reconnection sites. A generalization, necessary for example to systematically estimate the guide field, would require a local description of the perpendicular to the current sheet and of the average value around the flagged cell. I then define a "reduced" field $\mathbf{B}_\mathrm{r}$ as $\mathbf{B}_\mathrm{r} = \mathbf{B} - \mathbf{B}_\mathrm{g}$. It is then possible to evaluate the parallel component $B_\parallel$ and the perpendicular one $B_\perp$ of $\mathbf{B}_\mathrm{r}$ with respect to $\nabla|\mathbf{J}|$.

Fig. 4.2 shows the result for a single current sheet found in the simulation. The first and second panels show respectively the total magnetic field intensity $\mathbf{B}$ and the reduced magnetic field $\mathbf{B}_\mathrm{r}$, that can be considered a good approximation of the reconnecting field after the guide field subtraction. The third and fourth panels show $B_\parallel$ and $B_\perp$, i.e. the parallel and perpendicular components of $\mathbf{B}_\mathrm{r}$ with respect to the current sheet perpendicular $\nabla|\mathbf{J}|$. It is possible to notice that $\mathbf{B}_\mathrm{r}$ results more symmetric along the current sheet direction with respect to the total magnetic field $\mathbf{B}$ and that $B_\perp$ shows the inversion of polarity expected for a current sheet in which magnetic reconnection takes place.

This method can be extended to a local analysis, where for any cell identified the normal to the current sheet is evaluated and an estimate of the reconnecting magnetic field can be evaluated on the fly, in order to be more precise about the amount of magnetic energy available during the reconnection (See Sec. 6.2 for an application to this problem).

4.2   Application to a steady state current sheet

I test the algorithm presented in Sec. 4.1 also in a 2D simulation with a setup representing a current sheet of known values of σ and β of the fluid. Following Chiuderi & Velli (2014) we describe a stationary reconnection state.

The velocity field is described by:

$$\mathbf{v} \equiv \left[\frac{v_0}{a}x, -\frac{v_0}{a}y, 0\right] \ , \tag{4.4}$$

where v_0 and a are constant values.

The electric field is directed along the z direction, $\mathbf{E} = E\hat{\mathbf{e}}_z$, where E is the constant field strength. The magnetic field is assumed to lie in the x-direction, that is $\mathbf{B} \equiv [B(y), 0, 0]$ where the exact form of $B(y)$ can be recovered from the stationary condition $(\partial/\partial_t = 0)$ and the Ohm's law for a resistive plasma. This yields

$$B(y) = B_0 \, \mathrm{e}^{-(y/\Delta)^2} \int_0^{y/\Delta} \mathrm{e}^{u^2} \mathrm{d}u \; , \tag{4.5}$$

where $B_0 = 2Eca/v_0\Delta$, $\Delta = \sqrt{2\eta a/v_0}$ and η is the magnetic diffusivity. I set $c = 1$. I assume as pressure profile:

$$p = c_0 + f(y) + c_x x^2 + c_y y^2 \; . \tag{4.6}$$

In order to have a stationary solution we obtain the following conditions:

$$c_x = c_y = -\frac{\rho v_0^2}{2a^2} \qquad f(y) = -\frac{1}{8\pi} B^2(y) \; , \tag{4.7}$$

while the choice of c_0 has to guarantee that $p > 0$ over the whole domain.

The setup consists of a 2D square domain of size $L \times L$, with $x/\Delta, y/\Delta \in [-10, 10]$. The resolution is kept deliberately low in all the simulations, in order to have the resolution of only a few cells on the vertical of the current sheet, similarly to what is expected in large scale simulations representing astrophysical object in which many reconnection sites may be present. The boundary conditions are outflow everywhere. I set $v_0/a = 0.1$, $\eta = 0.05$, $\rho = 10^{-2}$ to be constant over the whole domain. Macroparticles are injected at $t = 0$ in the region $|y/\Delta| > 3$, so that all of them can be considered far away from the current sheet. The fluid is kept frozen in the initial configuration, while the macroparticles evolve according to Eq. (5.2).

I study the dependence of the threshold $\chi_{\min}$ on the numerical resolution of a current sheet and on the values of σ which can be detected, and thus sampled, by the algorithm (see Eq. 4.1). $\chi_{\min}$ has been determined as $\chi_{\min} \equiv \chi \, (y/\Delta = \pm 0.5)$, where χ is defined in Eq. (4.1). The resolution is indicated by the number of cells across the current sheet. I expect indicatively, in the simulations of an astrophysical jet, that the resolution, constrained by the computational demand, corresponds to a few cells in a single current sheet.

Fig. 4.3 shows the results. Clearly, for a given number of cells, lower values of threshold are required to sample lower values of σ. For a given σ, an increase in the number of cells requires a lower $\chi_{\min}$ for the algorithm to detect a reconnection site (by the definition of χ).
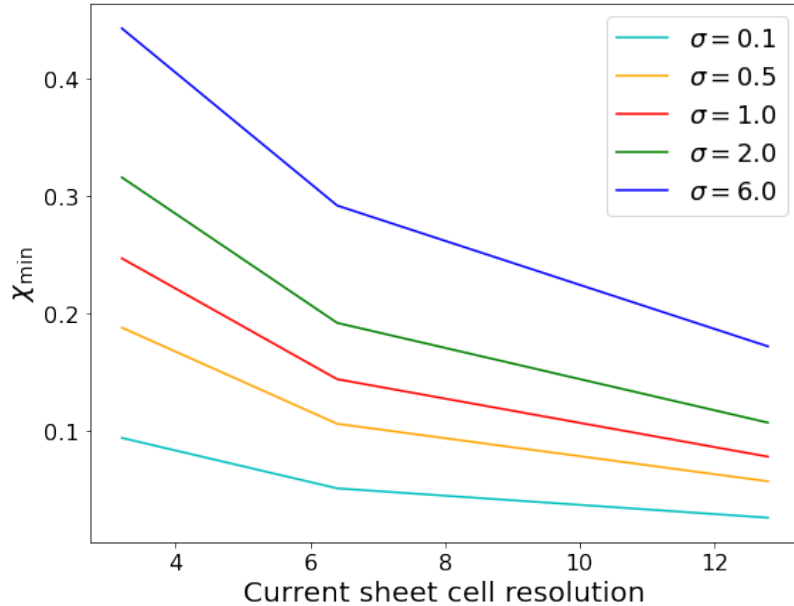
Figure 4.3: Values of the threshold χ_{min} (Eq. 4.1) required to sample different values of σ as a function of the resolution, given by the number of zones contained in the current sheet width. Different colours refer to different values of σ, as indicated.

While the results can not be simply extended to more complex situations, they can be indicative for the choice of the threshold for a given resolution and "required" minimum σ to be sampled.

4.3 Conclusions

In this chapter I have presented a new method to identify and characterize the physical properties of current sheets and reconnection regions in (R)MHD simulations, implemented in the PLUTO code (Mignone et al. 2007).

With respect to previous investigations, the novelty of our algorithm, for the identification of reconnection sites, is the improved computational efficiency in large scale simulations, and its capability of recognizing current sheets in complex 2D and 3D geometries.

5

Current sheet characterization

In Chap. 4 a new algorithm for the identification of the reconnection sites in large scale simulations has been proposed. The natural development of a complete subgrid model able to estimate the post reconnection spectra is to recognize what are the main plasma parameters describing the phenomenon and to develop an algorithm that can follow these quantities during the (R)MHD simulations.

Following the PIC result firstly introduced in Sec. 3.2 I now propose an algorithm able to sample these parameters.

The chapter is organized as follow: in Sec. 5.1 are described the main plasma parameter essential to the full characterization of the particles accelerated spectra and the validation done with the steady state reconnection setup already introduced in Sec. 4.2, then in Sec. 5.2 the newly developed algorithm is applied to a 2D injected jet setup and to a 3D unstable plasma column, in order to study in a complex and more realistic setup what are the expected sampled values for these parameters.

5.1 Characterization of Magnetic Reconnection properties

In order to estimate the efficiency of particle acceleration and the particle spectra resulting from our simulations, it is necessary to determine the physical properties of the identified reconnection sites. As shown in Sec. 3.2, PIC studies (Werner et al. 2017; Ball et al. 2018) have shown that the plasma quantities that play a major role

in this respect are the cold ion (proton) magnetization σ and β (the ratio between proton thermal pressure and magnetic pressure) defined as:

$$\sigma \equiv \sigma_{\mathrm{i}} \equiv B^2/4\pi n_{\mathrm{i}} m_{\mathrm{i}} c^2 \qquad \beta \equiv \beta_{\mathrm{i}} \equiv 8\pi n_{\mathrm{i}} k T_{\mathrm{i}}/B^2 \,, \tag{5.1}$$

where B refers to the magnetic field that undergoes reconnection and n_{i} is the ion density. Both quantities refer to the plasma region surrounding the reconnection site. In the following I will use the symbols σ and β to refer to the fluid quantities of Eq. (5.1).

The spectrum is described as a power-law distribution in particle energy, $f(\epsilon) \propto \epsilon^{-p}$ with a high-energy cut–off. ϵ is $\epsilon = (\gamma_{\mathrm{p}} - 1)mc^2$, where γ_{p} is the macroparticle's Lorentz factor. In particular in Werner et al. (2017) the particles spectrum has been studied in the semi-relativistic regime ($10^{-3} < \sigma < 1$) and up to the relativistic one ($\sigma \gg 1$). Their work has shown that the expected power-law index p and cut-off energy (Eq. 3.14) can be approximated as a function of σ. Their results are in agreement with those by Ball et al. (2018). While this holds for $\beta \times 3 \cdot 10^{-3}$, Ball et al. (2018) found that at higher values the power-law steepens and the final index p depends also on the value of β (Eq. 3.16).

The other two parameters needed for the description of the post-reconnection spectrum, i.e. the fraction of energy gained by the electrons and the acceleration efficiency, also depend on the same fluid parameters σ and β (Werner et al. 2017; Ball et al. 2018, Eqs. 3.15 and 3.19). With the sampling of these two quantities it is thus possible to reasonably approximate the particle spectra. In Chap. 6 I will focus on results for an ion-electron plasma and the electrons acceleration through the use of macroparticles and a sub-grid model based on PIC simulations results.

The values usually assumed in PIC studies in order to determine the initial configuration of the current sheet are the asymptotic values of σ and β, far from the reconnecting region. In the following corresponding σ and β will be identified with the respective fluid quantities around the region recognized as current sheet in the MHD simulations. In presence of complex structures and magnetic field configurations evolving with time a dynamic sampling of the fluid quantities is required.

Thus I develop an algorithm able to estimate their values at simulation runtime and keep track of them. This make use of macroparticle, comoving with the fluid, which sample σ and β.

The algorithm is implemented in the Lagrangian Particle module (Vaidya et al. 2018) in the PLUTO code (Mignone et al. 2007). In this module the spatial motion of macroparticles is described by:

$$\frac{d\mathbf{x}_\mathrm{p}}{dt} = \mathbf{v}(\mathbf{x}_\mathrm{p})\,, \tag{5.2}$$

where $\mathbf{v}$ represents the fluid velocity interpolated at the macroparticle's position and the subscript "p" labels the individual macroparticle.

While the macroparticles move in the domain according to Eq. (5.2), σ and β at the particle's position are sampled at each step and their value is stored in the variables σ_p and β_p and updated according to the following algorithm:

1. The first time a macroparticle exits a reconnection region or it is injected in the simulation domain, the corresponding values of σ and β are sampled by interpolating the fluid values at the macroparticle's position and stored as current σ_p and β_p. The variable N, describing the number of steps from the reset of σ_p and β_p values, is set to $N = 1$.

2. At each time step, while the macroparticle is in a cell that has not been tagged as current sheet region, the stored values are updated with the sampled ones if a new σ peak is detected.

3. In case σ does not represent a new peak, the stored values are updated through a weighted average, namely:

$$\begin{aligned} \sigma_\mathrm{p} &\leftarrow \sigma_{\mathrm{p,N-1}} + \frac{1}{N}\left(\sigma - \sigma_{\mathrm{p,N-1}}\right)\\ \beta_\mathrm{p} &\leftarrow \beta_{\mathrm{p,N-1}} + \frac{1}{N}\left(\beta - \beta_{\mathrm{p,N-1}}\right)\,, \end{aligned} \tag{5.3}$$

   where $\sigma_{\mathrm{p,N-1}}$ and $\beta_{\mathrm{p,N-1}}$ represent the values previously associated to the macroparticle and N is the number of steps from the last reset of the sampled quantities.

4. If the macroparticle is in a cell tagged as current sheet region the values σ_p and β_p are not updated. These values are describing the asymptotic values with which the macroparticle has entered the current sheet.

With the average of the sampled σ and β we ensure that σ_p and β_p remain good estimates of the values surrounding the current sheets, independently of possible peculiar behaviours of the plasma during its evolution far away from the reconnection sites.
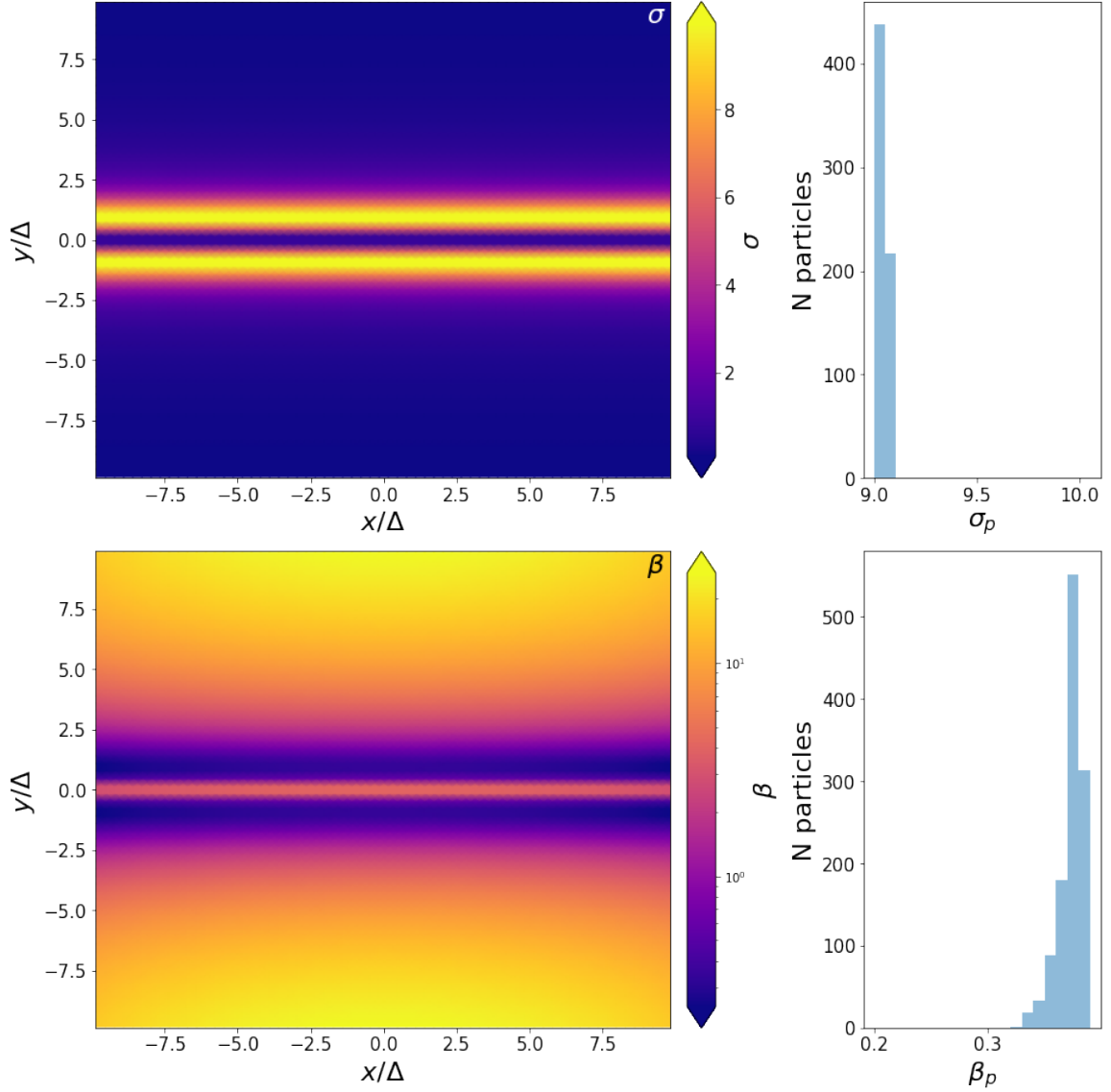
Figure 5.1: Results of the sampling of σ_{p} and β_{p} for the analytical setup (§5.1.1). The top and bottom left-hand panels represent, respectively, σ and β (in logarithmic scale) at $t = 30\Delta/c$. The right-hand panels show the corresponding distributions of σ_{p} and β_{p} sampled by the macroparticles located inside the reconnection region at that time.

5.1.1 Steady state current sheet: Numerical setup

I test the algorithm by determining σ_{p} and β_{p} in a 2D simulation with a setup representing a current sheet of known values of σ and β of the fluid. The setup is the same used to test the behaviour of the identification algorithm in Sec. 4.2, following the setup proposed in Chiuderi & Velli (2014).

I briefly remind that for this setup the velocity field is described by:

$$\mathbf{v} \equiv \left[\frac{v_0}{a}x, -\frac{v_0}{a}y, 0\right] , \tag{5.4}$$

where v_0 and a are constant values.

The electric field is directed along the z direction, $\mathbf{E} = E\hat{\mathbf{e}}_z$, where E is the constant field strength. The magnetic field is assumed to lie in the x-direction, that is $\mathbf{B} \equiv [B(y), 0, 0]$ where the exact form of $B(y)$ is:

$$B(y) = B_0 \, \mathrm{e}^{-(y/\Delta)^2} \int_0^{y/\Delta} \mathrm{e}^{u^2} \mathrm{d}u , \tag{5.5}$$

where $B_0 = 2Eca/v_0\Delta$, $\Delta = \sqrt{2\eta a/v_0}$ and η is the magnetic diffusivity. We set $c = 1$.

I assume as pressure profile:

$$p = c_0 + f(y) + c_x x^2 + c_y y^2 . \tag{5.6}$$

I remind that the stationary solution require:

$$c_x = c_y = -\frac{\rho v_0^2}{2a^2} \qquad f(y) = -\frac{1}{8\pi}B^2(y) , \tag{5.7}$$

while the choice of c_0 has to guarantee that $p > 0$ over the whole domain. Notice that the pressure profile contains a component $\propto x^2, y^2$, introducing a dependence on β, which is a function of the horizontal distance from the center of the simulation. This dependence is expected to be reflected in the distribution of the β_{p} sampled by the macroparticles.

This setup, with the $B(y)$ and $p(y)$ profiles showing respectively a peak and a minimum for $y/\Delta = \pm 1$, is particularly suited to verify our sampling algorithm. In fact, the macroparticles with initial position $|y/\Delta| > 1$ start with σ_{p} and β_{p} values that are reset when they encounter the peak of σ at $y/\Delta = \pm 1$, allowing us to verify both the condition of reset of the algorithm and the agreement between the sampled σ_{p} and the β_{p} and the fluid ones as defined in Eq. (5.1).

The setup consists of a 2D square domain of size $L \times L$, with $x/\Delta, y/\Delta \in [-10, 10]$. The resolution is kept deliberately low (64×64 cells), in order to have the resolution of

only a few cells on the vertical of the current sheet, similarly to what expected in the simulations of Sec. 5.2. The boundary conditions are outflow everywhere. I set $v_0/a = 0.1$, $\eta = 0.05$, $\rho = 10^{-2}$ to be constant over the whole domain, $\sigma_{\mathrm{peak}} \equiv \sigma(y/\Delta = \pm 1) = 10$. Macroparticles are injected at $t = 0$ in the region $|y/\Delta| > 3$, so that their initial sampled value is far from the reconnection region and from the expected maximum values of σ and β. The fluid is kept frozen in the initial configuration, while the macroparticles evolve according to Eq. (5.2). I set $\chi_{\mathrm{min}} = 0.4$ as the threshold to identify the reconnection region, defined in Eq. (4.1) and according to the findings of Sec. 4.2 for the value of σ set for the initial conditions.

5.1.1.1 Results on MR characterization

The results of the sampling of σ_{p} and β_{p} are shown in Fig. 5.1. The top and bottom panels on left–hand side represent the plasma values of σ and β (in logarithmic scale), respectively. As expected σ peaks in a region along the entire x−axis at $y/\Delta = \pm 1$, with $\sigma_{\mathrm{max}} = 10$. A similar profile is found for β, where at $y/\Delta = \pm 1$ a minimum of $\beta_{\mathrm{min}} \sim 0.34$ is found. The right–hand panels show the results of the sampling of σ_{p} and β_{p} for the macroparticles that are inside the reconnection region at time $t = 30\Delta/c$. The algorithm correctly resets their values at $y/\Delta = \pm 1$. The distributions found for σ_{p} and β_{p} are narrowly peaked at values close to the fluid σ_{max} and β_{min}. More precisely, the sampled σ_{p} are systematically lower with respect to the peak value: this can be ascribed to the number of averaging operations ($N \sim 9 - 10$ in this setup) that the sampling method performs before the macroparticles enter the reconnection region. The larger spread of the distribution of β_{p} with respect to that of σ_{p} is due to the pressure profile of Eq. (5.6), as mentioned above.

5.2 Jet simulations

I now wish to assess the validity of the method on more complex configurations like those typically found in magnetically dominated jets.

5.2.1 Slab Jet

5.2.1.1 Numerical setup

The setup consists of a 2D rectangular domain of size $L \times L/2$, with a resolution of 2048×1024 grid points. The ambient medium has constant pressure $p_0 = 2 \times 10^{-3}$, density $\rho_0 = 1$ and a magnetic field along the x–axis with constant magnitude $B_0 =$

$\sqrt{2\sigma_{\rm h}p_0}$, where $\sigma_{\rm h}$ is the hot magnetization, different from the cold one sampled by the macroparticles in the algorithm and defined as $\sigma_{\rm h} = B^2/\rho_0 w c^2$, where w is the enthalphy. The jet enters the domain from a nozzle of radius $r_{\rm j} = 1$ along the x–direction, with speed $v_{\rm j} = 0.95c$. The domain size can be defined based on $r_{\rm j}$ so that $L = 40r_{\rm j}$. The jet pressure is assumed to be the same of the ambient medium, $p_{\rm j} = p_0$, while its density is $\rho_{\rm j} = \lambda\rho_0$, where $\lambda = 10^{-2}$ represents the density ratio. The macroparticles are injected at a fixed time interval $\Delta t_{\rm inj} = 1$ at the jet base, in a region $x \in [0, r_{\rm j}]$ and $y \in [-r_{\rm j}, r_{\rm j}]$ with one macro-particle per cell. The boundary conditions are outflow everywhere except for the injection region.

Values of p and ρ in the ambient medium have been chosen so that the ensuing jet is not ballistic. I consider different values of $\sigma_{\rm h}$ in order to determine the expected sampled values of $\sigma_{\rm p}$ and $\beta_{\rm p}$. Specifically, I set the initial jet and ambient magnetization to be equal and study two cases with $\sigma_{\rm h} = 2$ and $\sigma_{\rm h} = 6$.

I run the simulations with different values of $\chi_{\rm min} = 0.3, 0.2, 0.1$ and for $\chi_{\rm min} = 0.1$ also at a lower resolution of 1024×512 grid points. With the high and low resolution $r_{\rm j}$ results resolved respectively by ~ 51 and ~ 25 cells.

5.2.1.2 Results

The results obtained from the simulation with $\sigma_{\rm h} = 2$ are shown in Fig. 5.2 at $t = 112$. In the top and bottom left–hand panels the values of (cold) σ and β (defined in Eq. 5.1) are plotted, respectively (in logarithmic scale for β). As expected, nearby the injection region, the values of σ and β remain similar to the initial values (for these initial conditions we have $\sigma_{\rm h} \sim \sigma$) while, when interacting with the external medium, the values of σ (β) tend to decrease (increase). The distributions of the corresponding quantities $\sigma_{\rm p}$ and $\beta_{\rm p}$ sampled by the macroparticles that entered a reconnection region at times $t = 112 \pm 10$ are shown in the right-hand panels. The different histograms refer to different threshold values ($\chi_{\rm min}$) and grid resolutions. The corresponding macroparticles positions are marked in the top left–hand panel using green dots.

The $\sigma_{\rm p}$ distribution is not monotonic: most of the reconnection sites have very low values of $\sigma_{\rm p}$, but another peak is observed at $\sigma_{\rm p} \approx 2$. The distribution of $\sigma_{\rm p}$ around this peak is shown in the inset of the histogram. Such a behaviour reflects the fact that the sampling macroparticles can enter reconnection sites lying in strongly magnetized regions (near the jet beam) as well as in the cocoon. The values of β span a broad range with only a small fraction achieving $\beta \lesssim 1$. The distribution of $\beta_{\rm p}$ has two peaks (around $\beta_{\rm p} \approx 0.3$ and a broad one around ~ 10) in correspondence of the two maxima of $\sigma_{\rm p}$. For the sake of clarity the main plot shows the distribution for $\beta_{\rm p} < 1$, while
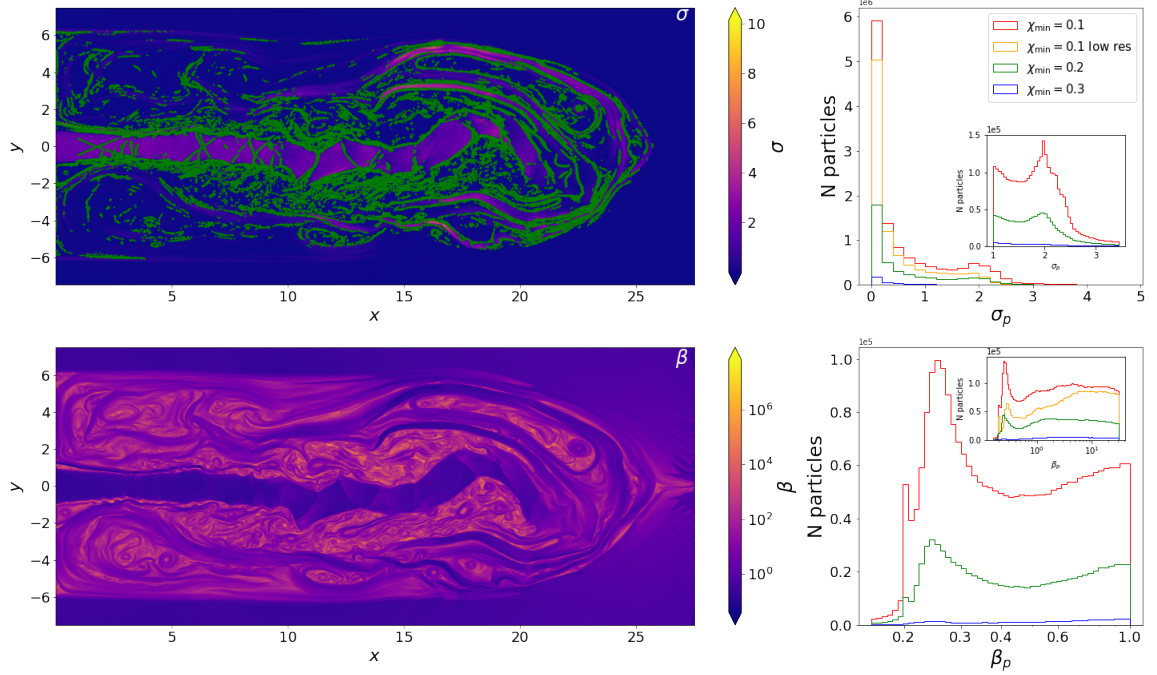
Figure 5.2: Results for the 2D MHD jet simulation with continuous injection, initial $\sigma_{\mathrm{h}} = 2$, $\chi_{\mathrm{min}} = 0.1$ at the largest resolution. The left-hand panels show σ and β (in logarithmic scale) of the fluid at $t = 112$. In the upper left panel the macroparticles lying inside a reconnection region at $t = 112$ are represented as green dots. The right-hand panels represent the distributions of σ_{p} and β_{p} sampled by the macroparticles that entered a reconnection region in the time interval $t = 112 \pm 10$. The distributions for different thresholds χ_{min} and resolutions are also plotted. For the sake of clarity the histogram of σ_{p} around $\sigma_{\mathrm{p}} \sim 2$ is plotted in the inset of the σ_{p} distribution. For β_{p} the main distribution plot is limited to $\beta_{\mathrm{p}} < 1$, while the whole distribution is shown in the inset.
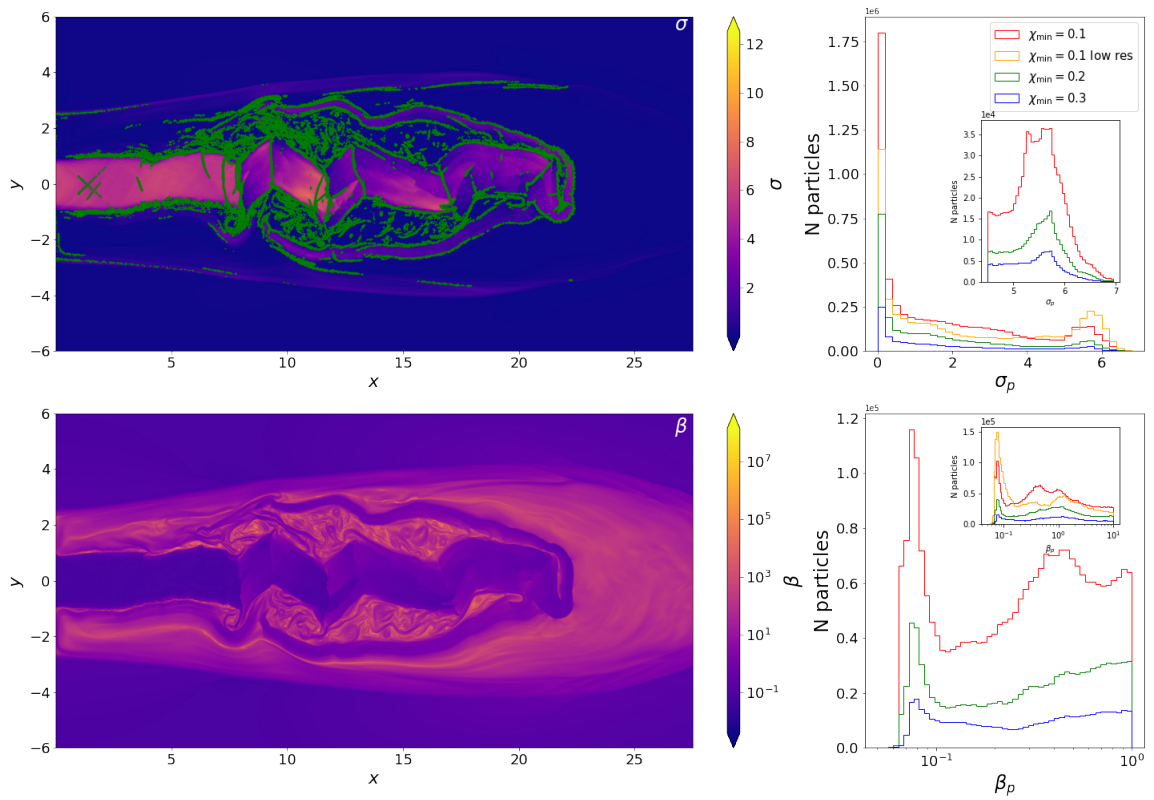
Figure 5.3: Same as Fig. 5.2 but for $\sigma_{\mathrm{h}} = 6$. For the sake of clarity the histogram of σ_{p} around $\sigma_{\mathrm{p}} \sim 6$ is plotted in the inset of the σ_{p} distribution. For β_{p} the main distribution plot is limited to $\beta_{\mathrm{p}} < 1$, while the whole distribution is shown in the inset.

the whole range spanned is plotted in the inset. Fig. 5.3 reports the same quantities for the case with $\sigma_\mathrm{h} = 6$: consistently, the second peak of the σ_p distribution for this case is located around $\sigma_\mathrm{p} \approx 6$, in agreement with the value injected at the base of the jet. These results confirm that the method can correctly sample the reconnection sites as well as the magnetization and plasma β values.

Regarding the choice of χ_min (which determines the total number of samples sites), I observe the peaks in the distribution start to become significant for $\chi_\mathrm{min} \sim 0.2$ and are better sampled for $\chi_\mathrm{min} = 0.1$. This is even more clear for the setup with initial $\sigma_\mathrm{h} = 6$ due to the dependence of the value of χ_min on the value of the minimum σ_p that the algorithm can sample (see Sec. 5.1.1.1).

Finally, in both simulations I compare the results obtained with a lower resolution: no dramatic differences are found, with some differences in the number of sampling particles and distribution of σ_p and β_p that can be ascribed to the different simulations that have been performed to obtain these results.

For a better understanding of the behaviours of field and macroparticles in these large scale setups a zoom on a reconnection region of the simulation of Fig. 5.3 around $x \approx 10$ and $y \approx 2$ is reported in Fig. 5.4. The region at the center of the plot is identified by the algorithm as a reconnection site, with many other smaller current sheets around it. The top panel shows the values of χ (for $\chi \geq 0.1$) together with the positions of the macroparticles, represented as green dots. Many macroparticles are inside this reconnection site at the time of the snapshot, after they sampled σ_p and β_p while entering it. The values of σ are plotted in the central panel together with the magnetic field topology indicated by arrows whose length is proportional to its strength. Around the reconnection site σ is higher with respect to its center, with $\sigma \gtrsim 1$. Its values are not symmetric on the two sides of the current sheet, reflecting the asymmetry of the configuration. Asymmetric configurations with different values of σ around the reconnection site have also been recently investigated with PIC simulations by Mbarek et al. (2022) showing that relativitic asymmetric reconnection still produce power-law distributions and the slope depends on the magnetization of both inflowing plasmas. The same behaviour can be taken into account by our method, with macroparticles entering from both sides.

The magnetic field lines show inversion of the direction along the perpendicular to the current sheet, as we expect in reconnection events.

In the bottom panel the values of β are shown together with the velocity field of the particles. Although the σ values for this current sheet are typically high, most of the plasma has values $\beta \gtrsim 1$ and only the sides of the most powerful reconnection region

in the figure has $\beta \lesssim 1$. The velocity field follows a behaviour similar to the magnetic field lines, as we expect in ideal RMHD.

Although I will amply discuss the following point in Chap. 6, it is worth noticing that the majority of the reconnection sites that these setups generate have values of β_{p} that are too large for efficient acceleration of particles to relativistic energies: in this case the dissipated energy may increase the temperature of the fluid. This can be more clearly seen in Fig. 5.5, a 2D histogram of the values of σ_{p} and β_{p} for the case with injected $\sigma_{\mathrm{h}} = 6$ (corresponding to Fig. 5.3 and $\chi_{\mathrm{min}} = 0.1$). The color bar in the 2D histogram describes the number of particles with specific σ_{p} and β_{p} values. The corresponding 1D histograms show their probability distributions function. Most of the sites with the lowest values of σ_{p} are associated to the tail of the β_{p} distribution at high values. A population of particles with favourable acceleration condition is present at high values of σ_{p} and $\beta_{\mathrm{p}} \simeq 10^{-1}$. I stress however that in this configuration these values depend on the fluid properties set for the simulations.

5.2.2   3D unstable plasma column

5.2.2.1   Numerical setup

I now study a 3D plasma column threaded by an helical magnetic field and unstable to current–driven kink mode. Both MHD and PIC numerical simulations have shown, indeed, that such configurations may naturally generate reconnection regions which can accelerate particles to non-thermal energies (Striani et al. 2016; Alves et al. 2018; Bromberg et al. 2019; Davelaar et al. 2020; Ortuño-Macías et al. 2022). Bodo et al. (2013) performed an in-depth linear analysis of the instabilities and studied the development of kink instabilities that may form reconnecting regions (Bodo et al. 2021; Bodo et al. 2021).

Following Bodo et al. (2013), the 3D initial configuration of the force-free magnetic field of the magnetically dominated jet is described, in cylindrical coordinates, by:

$$
\begin{aligned}
B_{\mathrm{r}} &= 0 \\
B_{\varphi} &= -\frac{B_{\varphi c}}{(r/a)} \sqrt{\left[1 - \exp\left(-\frac{r^4}{a^4} \right) \right]} \\
B_{\mathrm{z}} &= B_{\varphi c} \sqrt{\left[P_{\mathrm{c}}^2 - \frac{\sqrt{\pi}}{a^2} \mathrm{erf}\left(\frac{r^2}{a^2} \right) \right]},
\end{aligned}
\tag{5.8}
$$

where erf() is the error function, $a = 0.6 r_{\mathrm{j}}$ is the magnetization radius (the radius within the magnetic field is concentrated), $r_{\mathrm{j}} = 1$ is the jet radius and $B_{\varphi c}$ is the
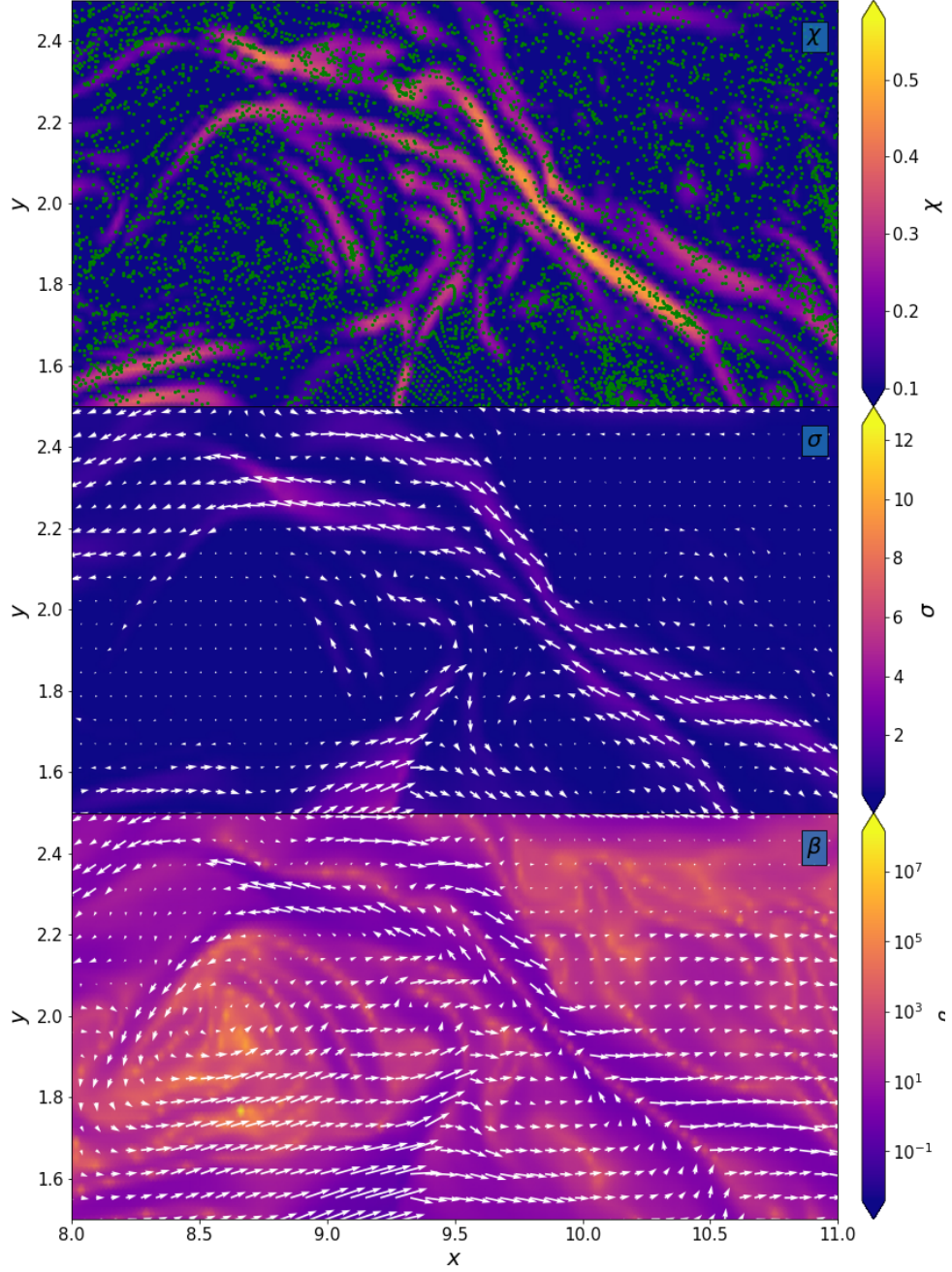
Figure 5.4: Closeup view of the region $x \in [8, 11]$ and $y \in [15, 2.5]$ for the 2D RMHD jet simulation, shown in Fig. 5.3. **Upper panel:** colormap of χ used to identify reconnection regions (Eq. 4.1). The minimum value has been set to the chosen threshold $\chi_{\min} = 0.1$. Macroparticles located inside the identified sites are shown as by green points. **Central and bottom panels:** colormaps of σ and β with arrows representing the magnetic field (central) and velocity field (bottom). Arrow length is proportional to magnitude.
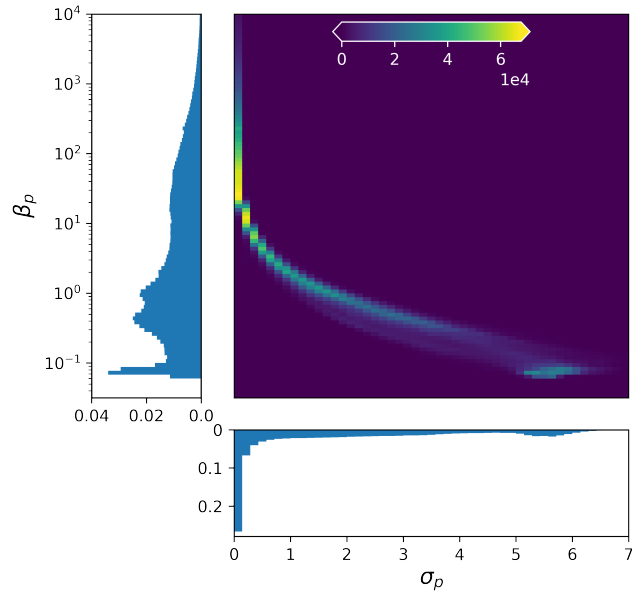
Figure 5.5: Values of σ_p and β_p for the 2D RMHD jet simulation with injected $\sigma_\mathrm{h} = 6$ at $t = 112 \pm 10$ (corresponding to Fig. 5.3). The left and bottom plots show the 1D histogram of the probability distribution funtion, while the combined probability distribution is represented in the 2D plot, where the color gives the number of particles. The probabilities represented refer to the whole 3D domain.

maximum azimuthal field. The configuration is thus characterized by the pitch angle P_c and the average hot magnetization σ_h. More precisely, P_c is the value of the pitch of the magnetic field on the jet axis, defined as:

$$P_c = \left| \frac{r B_z}{B_\varphi} \right| \ , \tag{5.9}$$

and the hot average magnetization σ_h is:

$$\sigma_h = \frac{\langle B^2 \rangle}{\rho_0 h c^2} \ , \tag{5.10}$$

where $\langle B^2 \rangle = \int_0^a (B_z^2 + B_\varphi^2) r dr / \int_0^a r dr$ and $\sigma_h = 10$. The initial values of density ρ_0 and pressure p_0 are uniform, with $p_0 = 0.01 \rho_0 c^2$ in order to have a cold jet. Following Bodo et al. (2021) I choose $P_c/a = 1.332$ to guarantee a fast growth of the instabilities and efficient dissipation. For simplicity, the numerical simulations are performed in a frame in which the jet plasma is not moving ($v_z = 0$). As the jet is highly magnetized, it is necessary to solve the relativistic MHD equations.

The macroparticles are initially located in the jet volume ($r < r_j$) and, as in the 2D case, during the evolution of the simulation they can move across reconnecting regions, providing a sampling of the fluid quantities around them.

The computational box is the cube $L \times L \times L_z$ discretized with $700 \times 700 \times 250$ grid zones, where $L = 60 r_j$ and $L_z = 10 r_j$. The grid is uniform for $|x|$, $|y| < 8$ ($x = y = 0$ are on the jet axis) and geometrically stretched elsewhere in order to have a box large enough to avoid spurious effects from the lateral boundaries. The stretched grid is generated as follow. A stretching ratio r is computed as:

$$\delta x = (r + r^2 + \ldots + r^N) = x_R - x_L \quad \Rightarrow \quad r \frac{1 - r^N}{1 - r} = \frac{x_R - x_L}{\Delta x} \ , \tag{5.11}$$

where Δx comes from the uniform grid, N is the number of points of the stretched grid patch and x_L and x_R are respectively the leftmost and rightmost points of the patch. The boundary conditions are periodic in the z direction and outflow elsewhere.

5.2.2.2 Results

The results of the simulation are reported in Fig. 5.6, where σ and β isosurfaces are shown together with slice cuts. I analyze 3 different simulation times $t = 50, 100, 140$ representative of different phases of the evolution of the plasma column, respectively: the linear phase, the full onset of the kink instabilities and the final phase when the column gets disrupted.
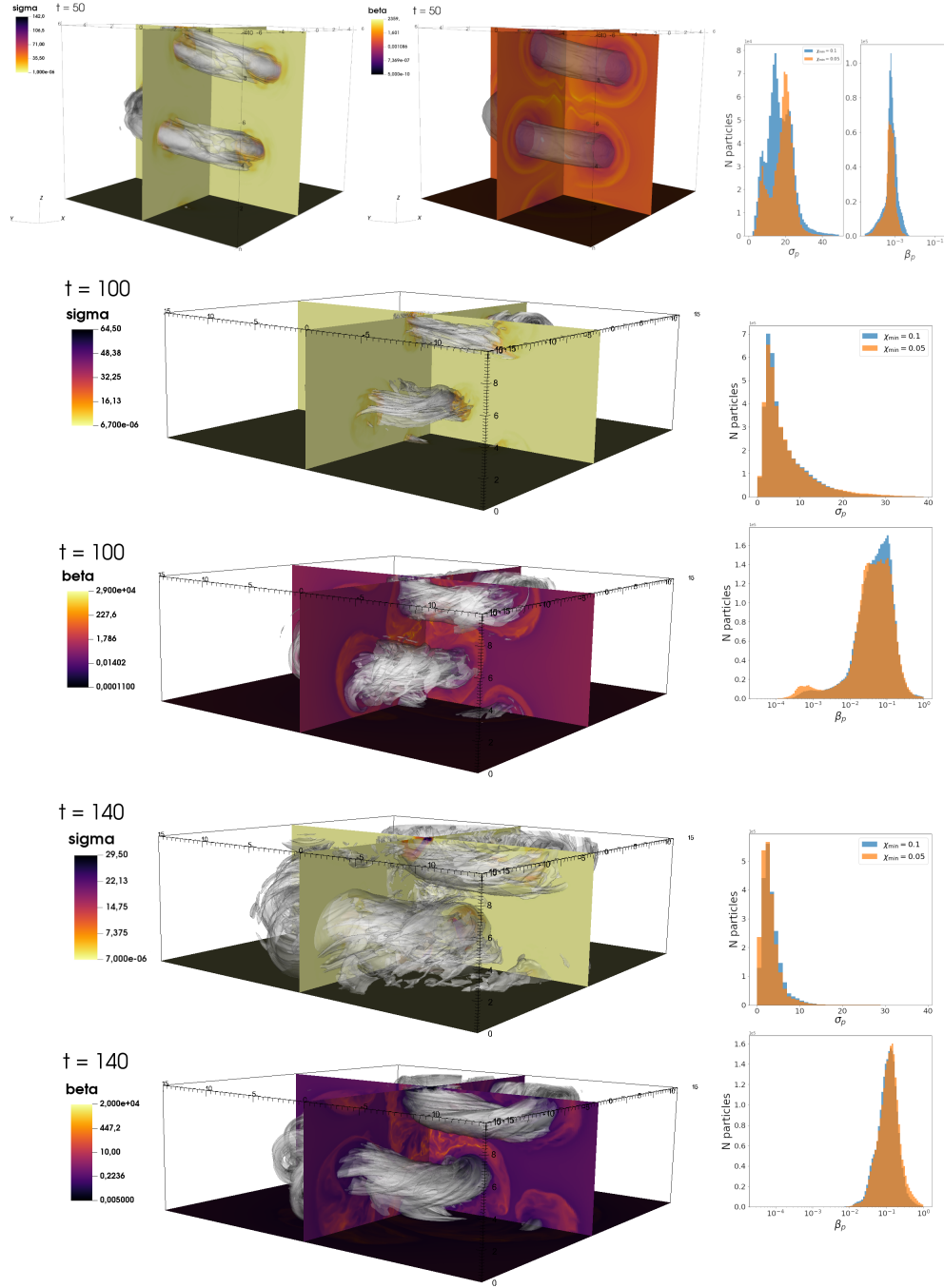
Figure 5.6: Results for the 3D RMHD jet simulation for an initial $\sigma_{\mathrm{h}} = 10$ and a threshold $\chi_{\mathrm{min}} = 0.1$. Three different times ($t = 50, 100, 140$) are shown. The domain is restricted to $x, y \in [-6, +6]$ for $t = 50$ and $x, y \in [-15, +15]$ for $t = 100, 140$. For each panel the jet values of σ and β (in logarithmic scale) are shown, with a 3D slice and an isosurface plot. The right-hand panels represent (in blue) the distributions of σ_{p} and β_{p} sampled by the macroparticles that entered a reconnection region in the time interval of the respective plot time ± 10. The distributions coloured in orange refer to the results with a threshold $\chi_{\mathrm{min}} = 0.05$.
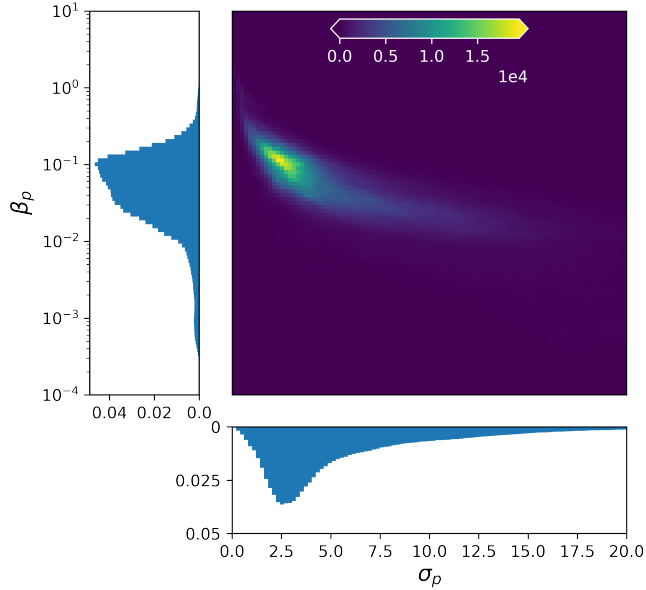
Figure 5.7: Same as Fig. 5.5 but for the 3D RMHD jet simulation, with initial $\sigma_{\mathrm{h}} = 10$ at $t = 100 \pm 10$ (corresponding to $t = 100$ in Fig. 5.6).

A threshold $\chi_{\min} = 0.1$ has been set for the identification of the reconnection sites. Similarly to the 2D case (Sec. 5.2.1), the right–hand panels of the figures report the distributions (in blue color) of the sampled quantities σ_{p} and β_{p} over the whole 3D domain.

During the linear phase ($t = 50$) the reconnection sites are located at the borders of the column (its external parts), where σ and β achieve, respectively, large and small values. The values of σ_{p} sampled by the macroparticles are as large as 20. As expected, the instability leads to the formation of increasingly complex spatial structures (corresponding to the growth of different azimuthal modes, on top of the $|m| = 1$ mode) with a systematic decrease of the magnetization ($t = 100, 140$) and reconnection sites occupying the whole column volume. The distributions of σ_{p} and β_{p} at $t = 50$ are still similar to the initial values and, at later times of the evolution, their values reach quasi-equipartition, with the distributions becoming more peaked around $\sigma_{\mathrm{p}} \sim$ a few and $\beta_{\mathrm{p}} \sim 10^{-1}$.

In order to check the effect of the threshold, I also consider the case $\chi_{\min} = 0.05$. The resulting distributions of σ_{p} and β_{p} are shown in the right–hand panels of the figures using orange color. While during the initial phase, the distributions of σ_{p} are sensitive to the value of $\chi_{\min}$, at later times the distributions are basically indistinguishable,

indicating that the chosen value of threshold $\chi_{\min} = 0.1$ could be adequate in the long-term evolution of the reconnection regions. I notice that a lower threshold does not increase the number of sampled particles: this is due to the fact that macroparticles tend to concentrate in the regions around reconnection sites.

I stress that in the resulting 3D structure of the reconnection regions, with very asymmetric and complex geometry of the reconnection sites, the algorithm I developed shows its full potential for the sampling of the relevant physical parameters.

Finally, in Fig. 5.7, I show again a 2D representation of the probability distributions function of σ_p and β_p at $t = 100$. The color bar in the 2D histogram describes the number of particles with specific σ_p and β_p values. The vast majority of the reconnection regions are characterized by $\sigma_p \sim 2.5$ and $\beta_p \sim 10^{-1}$. PIC simulations indicate that these values are suited for efficient acceleration of a non-thermal particle distribution with typical power-law indices broadly consistent with observations. I notice that this differs from the results of the 2D case with the continuous injection (see above). Plausibly this is due to the greater dependence of the values sampled on the initial (and border) conditions in the slab jet with respect to the case of the evolving plasma column. Such (promising) findings are explored in Chap. 6.

5.3 Conclusions

As my aim is to determine the effectiveness of MR events occurring in large scale simulations to accelerate particles to a non-thermal distribution, we have developed an algorithm which, using macroparticles in the fluid, sample the plasma properties. According to PIC simulations (see Sec. 3.2) the magnetization σ and the β are the chief parameters which determine the efficiency, energetics and resulting particle spectra. Such a sampling has been performed in both the 2D and 3D simulations and the statistical properties of such parameters have been inferred.

A limitation of the presented method is that the estimate of the magnetization does not take into account the possible presence of a guide field. I will present a way to overcome this limitation in Sec. 6.2 by using the method presented in Sec. 4.1.1 to estimate the guide field and subtracting to the sampled σ_p the component of magnetic field along the direction perpendicular to the current sheet. However a study of the dependence of the final spectra depending on both σ_p and β_p is needed.

Finally, a more fundamental limit could be given by the lack of energetic feedback between the fluid and the macroparticles. In Chap. 6 I will analyze how often the amount of energy given to the macroparticles is limited by the lack of feedback and

numerical limitation, in order to understand the importance of the implementation of the feedback in our sub-grid model.

6

Accelerated spectra update

The algorithm for the identification of reconnection sites introduced in Chap. 4 and the characterization of the plasma quantities around a current sheet as presented in Chap. 5 enable the implementation in the Lagrangian particles module of PLUTO code (Vaidya et al. 2018) a model for electrons the post-reconnection update. In this numerical framework the spectra of the macroparticles is evolved with the use of the CRs transport equation.

The Chapter is organized as follow: in Sec. 6.1 I will briefly describe the Lagrangian particle module, responsible for the macroparticles spectra evolution. In Sec. 6.2 I will describe how it is possible to quantify the fraction of energy that goes from the reconnecting field to the non-thermal electron population. This novel sub-grid method will be presented with two different update techniques. In Sec. 6.3 is introduced a brute-force approach where the macroparticles spectra are reset to a power-law based on σ_p and β_p. In Sec. 6.4 a convoluted method is proposed, where the spectral update of the macroparticles considers the history of the spectra and accounts for multiple macroparticles within the same computational cell. Finally in Sec. 6.5 the convoluted method is applied to RMHD simulations of a 3D unstable plasma column, studying spectra evolution in a complex setup.

6.1 Lagrangian particles: a module for non-thermal emissions

The Lagrangian particles module in the PLUTO code (Vaidya et al. 2018) has been developed to study radiative emissions due to non-thermal populations in large scale (R)MHD simulations. A macroparticle, the fundamental element of this module, is defined as an ensemble of real particles that can be considered close in space and described by their collective spectrum. Differently from the particles that are part of the plasma description, macroparticles have non-thermal spectra, for example due to MR acceleration. In Chap. 5 I extensively used the macroparticles to sample the σ and β parameters while they were approaching a current sheet, but I did not make use of the full capabilities of the spectral evolution present in the Lagrangian particles module. Now, with a method for the identification of MR regions and a sampling algorithm, it is possible to finally implement in this framework a spectral update due to MR acceleration.

The isotropic distribution function of the non-thermal particles in phase space for the relativistic case is defined as:

$$f_0(x^\mu, p) \ , \tag{6.1}$$

where x^μ represents the position four-vector and p the momentum magnitude.

The distribution is evolved in space and time with the relativistic CRs transport equation, as found in Webb (1989):

$$\begin{aligned}
&\nabla_\mu(u^\mu f_0 + q^\mu) + \\
&+ \frac{1}{p^2}\frac{\partial}{\partial p}\left[-\frac{p^3}{3}f_0\nabla_\mu u^\mu + \langle \dot{p}\rangle_l f_0 - \Gamma_{\text{visc}} p^4 \tau \frac{\partial f_0}{\partial p} - p^2 D_{pp}\frac{\partial f_0}{\partial p} - p(p^0)^2 \dot{u}_\mu q^\mu \right] = 0 \ .
\end{aligned} \tag{6.2}$$

The terms in the round brackets describe respectively the transport by convection and by diffusion, where u^μ is the bulk four-velocity of the fluid and q^μ is the spatial diffusion flux. The terms in the square brackets describe instead respectively the adiabatic expansion, the losses due to synchrotron and inverse Compton emissions, where $\langle \dot{p}\rangle_l$ is the average momentum change due to non-thermal radiation, the acceleration due to fluid shear, where Γ_{visc} is the shear viscosity coefficient, second order Fermi process, described by the diffusion coefficient in the momentum space D_{pp} and lastly non-inertial energy changes due to the measurement of the momentum p in a frame moving with the fluid.

The equation can be implemented together with a RMHD solver to evolve concurrently the plasma and the distribution describing the non-thermal population. This has been done with the PLUTO code (Vaidya et al. 2018). In the implementation, some assumptions have been taken into account. Specifically it has been neglected the spatial diffusion ($q^\mu = 0$), the energization due to shear ($\Gamma_{\mathrm{visc}} = 0$), second order Fermi process ($D_{pp} = 0$) and non-inertial energy changes. Eq. (6.2) reduces then to:

$$\nabla_\mu(u^\mu f_0) + \frac{1}{p^2}\frac{\partial}{\partial p}\left[-\frac{p^3}{3}f_0\nabla_\mu u^\mu + \langle\dot{p}\rangle_l f_0\right] = 0 \ . \tag{6.3}$$

To further simplify the equation it is possible to define:

$$\mathcal{N}(p,\tau) = \int d\Omega p^2 f_0 \approx 4\pi p^2 f_0 \ , \tag{6.4}$$

where $\mathcal{N}$ represents the number of particles per unit volume lying in the range from p to $p + dp$ at a given time τ. In the relativistic case the energy of a particle can be express as $\epsilon \approx pc$ and so $\mathcal{N}(\epsilon,\tau)d\epsilon = \mathcal{N}(p,\tau)dp$.

Eq. (6.3) can be expressed for the quantity $\mathcal{N}(p,\tau)$ as:

$$\frac{d\mathcal{N}}{d\tau} + \frac{\partial}{\partial\epsilon}\left[\left(-\frac{\epsilon}{3}\nabla_\mu u^\mu + \dot{\epsilon}_l\right)\mathcal{N}\right] = -\mathcal{N}\nabla_\mu u^\mu \ , \tag{6.5}$$

where it has been defined $\dot{\epsilon}_l = \langle\dot{p}\rangle_l/p^2$.

Finally for computational reason the quantity to be evolved in the code is redefined as:

$$\chi(\epsilon) = \mathcal{N}(\epsilon)/n \ , \tag{6.6}$$

where n is the fluid number density. $\chi(\epsilon)$ represents the number of particles in the non-thermal component normalized to the fluid number density for the energy ϵ. In the following the macroparticles will describe the electron population.

Eq. (6.5) becomes for the quantity χ:

$$\frac{d\chi}{d\tau} + \frac{\partial}{\partial\epsilon}\left[\left(-\frac{\epsilon}{3}\nabla_\mu u^\mu + \dot{\epsilon}_l\right)\chi\right] = 0 \ . \tag{6.7}$$

The macroparticles are spatially evolved as described in Sec. 5.1, being carried along with the fluid.

The energy is discretized in N_ϵ energy bins of width, for the $p-$th macroparticle, $\Delta\epsilon_i^p = \epsilon_{i+\frac{1}{2}}^p - \epsilon_{i-\frac{1}{2}}^p$, spanning from $\epsilon_{\mathrm{min}}^p$ to $\epsilon_{\mathrm{max}}^p$, specific of the individual macroparticle and evolving dinamically during the simulation.

The maximum energy ϵ^p_{max} is numerically limited by the assumption of having the particles close in space. The particles can not be considered as part of the same macroparticle if their Larmor radius exceed the computational cell size, so that the limit on ϵ^p_{max} is:

$$\epsilon^p_{\text{max}} \leq \epsilon_{\text{Larmor}} = \gamma^{cf}_L m_{\text{e}} c^2 = \frac{eBr^{cf}_L}{\beta_\perp} , \qquad (6.8)$$

where $r^{cf}_L = 0.5 \min(\Delta x, \Delta y, \Delta z)$ at the macroparticle's position, B is the magnetic field and e is the electron charge. Everything is expressed in c.g.s. units. In the macroparticles limit the individual particles can be assumes as highly relativistic and $\beta_\perp$, representing the ratio of velocity perpendicular to the magnetic field of a single particle with the speed of light can be assumed as $\beta_\perp \approx 1$. Despite this possible computational limitation, in the results presented in this chapter the limitation in maximum energy has never been reached.

Radiative losses are threated as follow. For the Inverse Compton (IC) only the interaction with the isotropic Cosmic Microwave Background (CMB) is considered. The scattering is assumed to happen in the Thompson regime in the relativistic particles rest frame, so that the cross section σ_T is independent of the incident photon energy E_{ph}. The energy loss term for IC and Synchrotron is then given by:

$$\dot{\epsilon}_l = -c_r \epsilon^2 , \qquad (6.9)$$

where:

$$c_r = \frac{4}{3} \frac{\sigma_T c \beta^2}{m_e^2 c^4} \left[U_B(t) + U_{\text{rad}}(E_{\text{ph}}, t) \right] . \qquad (6.10)$$

U_B and U_{rad} are the magnetic and the radiation field energy densities. In the black body approximation U_{rad} is expressed as:

$$U_{\text{rad}} = a_{\text{rad}} T^4_{\text{CMB}} = a_{\text{rad}} T^4_0 (1 + z)^4 , \qquad (6.11)$$

where a_{rad} is the radiation constant, z is the red-shift and $T_0 = 2.782 \, \text{K}$ is the CMB temperature at the present epoch.

6.2 Evaluation of available energy

The identification and characterization algorithms introduced respectively in Chaps. 4 and 5 allow to implement a sub-grid model for the post-MR acceleration spectra.

All the quantities necessary to the sub-grid model can be determined based on σ_p and β_p as described in Sec. 5.1.

The first quantity to be evaluated in both the spectra update methods that we present in this chapter is the energy available to the non-thermal electron population from the reconnection event. I define δ_ϵ as the energy gained by the accelerated macroparticles due to MR. This energy is directly related to the intensity of the magnetic field that is reconnecting around the current sheet and can be expressed as:

$$\delta_\epsilon = f_{\text{rec}} \, q_e \, \epsilon_{\text{acc}} \, E_{B,r} \; . \tag{6.12}$$

The terms present in Eq. 6.12 can be defined and evaluated as follow:

- f_{rec} describes the fraction of the available magnetic energy that is released during a reconnection event. As shown in Werner et al. (2017), this fraction is $\sim 40\%$ of the total magnetic energy and it's only mildly dependent from σ in the trans-relativistic regime, while in the relativistic regime no dependency is observed. The factor f_{rec} is set to $f_{\text{rec}} = 0.4$.

- q_e is the fraction of the available energy that goes to the electron population (Eq. 3.15).

- ϵ_{acc} represents the fraction of the available energy that goes to the non-thermal component (Eq. 3.19).

- $E_{B,r}$ is the magnetic energy, evaluated using $\boldsymbol{B}_\perp$, component of the magnetic field surrounding the reconnection site that is locally parallel to the current sheet (and as a consequence perpendicular to the normal to the current sheet). In order to evaluate $\boldsymbol{B}_\perp$, while the macroparticle is moving outside a reconnection region, the magnetic field is sampled, individually for each component, with the same method described for σ_p and β_p (Sec. 5.1). The component of this field parallel to the current sheet is then evaluated with the same algorithm introduced in Sec. 4.1.1.

Since the feedback between the macroparticles and the fluid is not implemented in the code, a comparison between the energy given to the macroparticles and the internal energy at macroparticle's position has been implemented. A similar comparison has been introduced also for the number density. Two fractions f_E and f_N, representing respectively the fraction of the internal energy and of number density that I want to

check are not overcome, are introduced. We set for the simulations in this chapter $f_E = f_N = 0.1$.

In order to perform the energy comparison, during the spectral update the fuild internal energy at macroparticle's position is computed as:

$$
\begin{aligned}
\rho\epsilon &= \frac{p}{\Gamma - 1} \quad \text{Ideal EOS} \\
\rho\epsilon &= \frac{3}{2}p - \rho c^2 + \sqrt{\frac{9}{4}p^2 + \rho^2 c^4} \quad \text{T} - \text{M EOS} ,
\end{aligned}
\tag{6.13}
$$

where the second equation is valid for the Taub-Mathews (T-M) equation of state (Taub 1948; Mignone & McKinney 2007).

In the following simulation I keep track of how often the energy available overcome this fraction as indication of the importance of an introduction of a feedback.

6.3 Update without convolution with previous spectra

A simple implementation of the spectra update in the Lagrangian Particle module is to impose the new developed power-law as new spectrum for the macroparticles that are inside a reconnection sites, taking into account the previous energy of the macroparticle, but not considering the previous shape of the pre-acceleration spectrum.

In the current sheet the spectrum is updated to the power-law predicted by the theory:

$$
\mathcal{N}_{\text{mr}}(\epsilon, t) = \mathcal{N}(\epsilon_{\text{min}})(\epsilon/\epsilon_{\text{min}})^{-p+2} ,
\tag{6.14}
$$

where the $+2$ in the power-law index is due to the definition of $\mathcal{N}$ (Eq. 6.4).

The value ϵ_{min} is determined as the peak of the Maxwellian distribution that describes the thermal component at the macroparticle's position.

The normalization of the final spectrum is obtained by imposing the total energy of the spectrum as the sum of the energy in the pre-acceleration spectrum ϵ_{old} and the energy gained by the reconnection event δ_ϵ. The equation necessary to normalize the spectrum is then:

$$
\mathcal{N}(\epsilon_{\text{min}}) \int_{\epsilon_{\text{min}}}^{\epsilon_{\text{max}}} (\frac{\epsilon}{\epsilon_{\text{min}}})^{-p+2} \epsilon d\epsilon = \delta_\epsilon + \epsilon_{\text{old}} .
\tag{6.15}
$$

where ϵ_{max} is determined as described in Sec. 5.1.

The spectra update happens only if the maximum energy ϵ_{max} is higher than the one of the pre-acceleration spectrum.
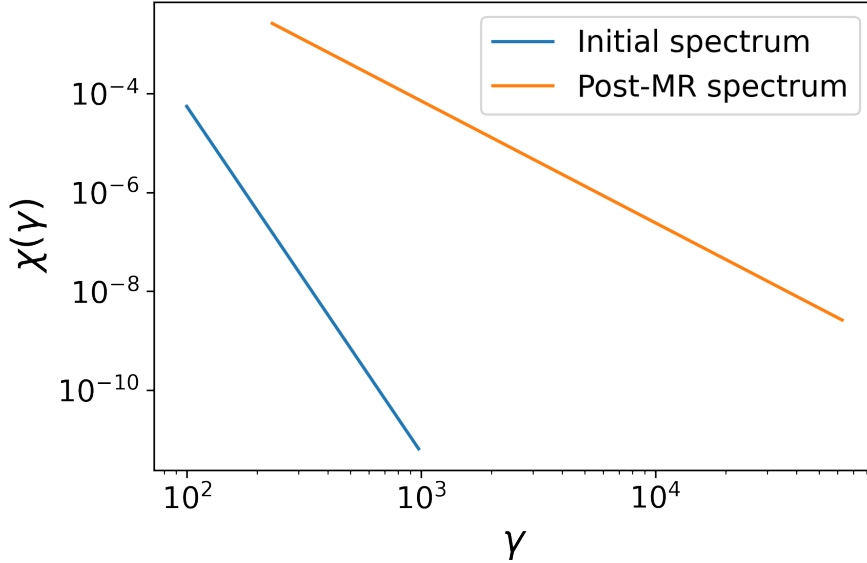
Figure 6.1: Result of the acceleration of a single macroparticle's spectrum due to magnetic reconnection without convolution, as described in Sec. 6.3.

In order to test the post-reconnection update I use the steady state current sheet configuration, already exploited to test the sampling method in Sec. 5.1.1. As in the previous test, the setup has a $\sigma_{max} = 10$ and the distribution of the sampled β_p values peaks around $\beta_p \sim 0.35$. With these sampled values a power-law index is expected $p \sim 4.5$, a non-thermal efficiency $\epsilon_{eff} \sim 0.2$ and a $q_e \sim 0.4$. The macroparticles are created at the beginning of the simulation with an initial steep power-law spectra with index $p = 7$, with $\gamma_{min} = 10^2$ and $\gamma_{max} = 10^3$.

The post acceleration spectrum, plot together with the initial injected spectrum is shown in Fig. 6.1.

As a result of the acceleration in the current sheet, the initial steep power-law is reset to the new index predicted by the sub-grid model. The old spectrum is taken into account when evaluating the energy previously present in the spectrum and only the minimum and maximum energy are reset and any previous slope is not considered. In this test all the macroparticles never overcame the limits of internal energy and number density fractions defined by f_E and f_N.

A possible limitation for this method is the presence of more than one macroparticle in the same computational cell at the moment of the spectra update. The same limit applies for the evaluation of δ_ϵ, where the quantity is determined for the single macroparticle irrespectively of the others. Eq. (6.15) takes into account the previous energy of the individual macroparticle and the resulting energy that is assigned to

the macroparticle is independent from how many other macroparticles are present in the same cell, resulting, in the case of numerous macroparticles accumulated in the same cell, in a overestimation of the energy that can be individually assigned to the macroparticles.

6.4 Update with convolution with previous spectra

For these reasons I developed a more refined model that is able to take into account not only the energy but also the pre-acceleration spectral shape and can correctly distribute the right amount of energy to each macroparticle when more than one is present in the same computational cell during the spectral update.

6.4.1 Convolution strategy

A macroparticle enters a reconnection region with a spectrum $\mathcal{N}_0(\epsilon)$. The final spectra $\mathcal{N}(\epsilon)$, obtained taking into account both the existing spectrum $\mathcal{N}_0(\epsilon)$ and the power-law generated by the reconnection acceleration $\mathcal{N}_{\mathrm{mr}}$, can be defined through a convoluted method, as firstly described for DSA in Mukherjee et al. (2021):

$$
\begin{aligned}
\mathcal{N}(\epsilon) &= \mathcal{C} \int_{\epsilon_{\min}}^{\epsilon} \mathcal{N}_0(\epsilon') \mathcal{N}_{\mathrm{mr}}(\epsilon, \epsilon') \frac{\mathrm{d}\epsilon'}{\epsilon'} \\
&= \mathcal{C} \int_{\epsilon_{\min}}^{\epsilon} \mathcal{N}_0(\epsilon') \left(\frac{\epsilon}{\epsilon'}\right)^{-p+2} \frac{\mathrm{d}\epsilon'}{\epsilon'} \ .
\end{aligned}
\tag{6.16}
$$

The initial spectrum is convoluted with the power-law $\mathcal{N}_{\mathrm{mr}}$ obtained by PIC prescriptions described in Sec. 5.1 and the integral is evaluated considering $\epsilon \in [\epsilon_{\min}, \epsilon_{\max}]$. $\epsilon_{\min}$ is the same of the initial spectrum $\mathcal{N}_0(\epsilon)$, while $\epsilon_{\max}$ is evaluated as described in Sec. 5.1. Similarly to the case without convolution (Sec. 6.3) the spectra update happens only if the newly found $\epsilon_{\max}$ is higher than the maximum energy of the pre-acceleration spectra $\mathcal{N}_0(\epsilon)$.

6.4.2 Normalization of spectra

The normalization factor $\mathcal{C}$ in Eq. (6.16) is set in two steps. First the normalization due to the available energy δ_ϵ is evaluated. Then, if the macroparticle number density is greater than the fraction f_N, the normalization is reset in order to match this fraction.

6.4.2.1 Energy normalization

In the first step I impose that the total energy of all the macroparticles undergoing MR in a single computational cell is the fraction of magnetic energy of the reconnecting field that is suppose to go to the non-thermal electron component δ_ϵ as described in Sec. 6.2. In presence of multiple macroparticles in the same cell the quantity $E_{B,r}$ necessary for the determination of δ_ϵ (Eq. 6.12) is evaluated as the average of this individual quantity for each macroparticle.

The energy available for all the macroparticles that have to be updated in the same cell is:

$$\Delta\epsilon = \min(\delta_\epsilon, f_E\rho\epsilon) - \sum_i \epsilon_i \ , \tag{6.17}$$

where $\sum_i \epsilon_i$ takes into account macroparticles that are in the computational cell but have been already updated with post-reconnection spectra or lie in the flagged region with β_p values that are not suitable for an efficient particle acceleration ($\beta_p > 0.5$). The energy of the single spectrum of these macroparticles is evaluated as:

$$\epsilon_i = \int_{\epsilon_{\min}}^{\epsilon_{\max}} \epsilon \mathcal{N}(\epsilon) \mathrm{d}\epsilon \ . \tag{6.18}$$

Their energy is so removed from the total energy available for the macroparticles that are undergoing reconnection in Eq. (6.17).

If the resulting available energy is $\Delta\epsilon > 0$, the energy so obtained is distributed among all the macroparticles that have to be updated in the computational cell, obtaining for each of them the normalization $\mathcal{C}$. If $\Delta\epsilon \leq 0$ no macroparticle is updated, since they have already reached the threshold of energy available and there is no more energy that can be provided from the fluid.

6.4.2.2 Number density normalization

In the second step I check that the normalization $\mathcal{C}$ found in the first step (Sec. 6.4.2.1) does not saturate the fraction of the fluid number density f_N that is imposed to the macroparticles. I compute:

$$\Delta N = f_N \frac{\rho}{\mu m_a} - \sum_i N_i \ , \tag{6.19}$$

where ρ is the fluid density interpolated at the macroparticle's position, $\mu = 0.6$ is the the mean molecular weight for ionised gas and m_a is the atomic mass unit. $\sum_i N_i$
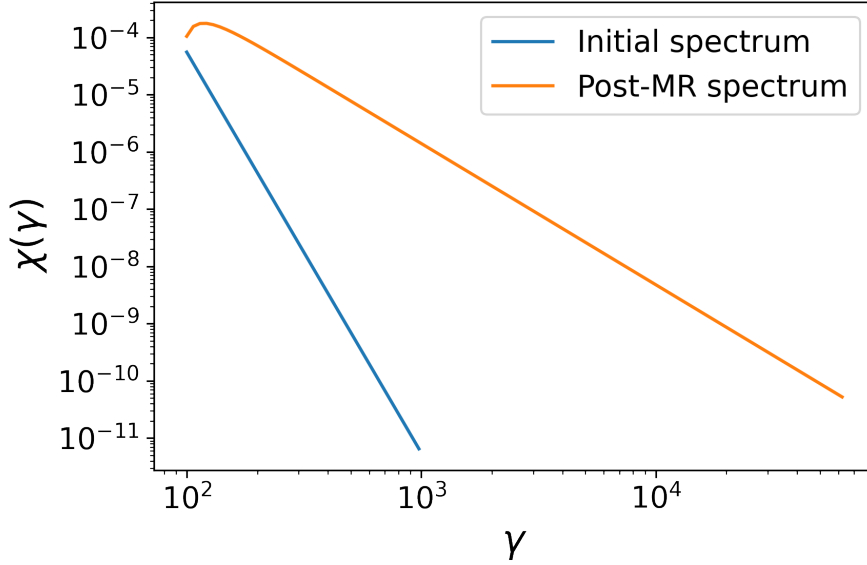
Figure 6.2: Results of the acceleration of a single macroparticle spectrum due to magnetic reconnection with the convoluted method (Sec. 6.4) an an initial steep spectrum.

takes into account the number density of the macroparticles in the computational cell that are excluded from the spectra update for the same reasons of Sec. 6.4.2.1.

The number density for a single macroparticle is obtained as:

$$N_i = \int_{\epsilon_{\min}}^{\epsilon_{\max}} \mathcal{N}(\epsilon) \mathrm{d}\epsilon \ . \tag{6.20}$$

If the result is $\Delta N > 0$ the macroparticles do not saturated the fraction of the number density available in the cell and the spectra is not further normalized. If instead $\Delta N < 0$ a new normalization based on the number density requirement is imposed, in order to ensure the maximum fraction f_N of the fluid number density.

6.4.3 Numerical validation

The same setup as in Sec. 6.3 has been used to test for the convoluted method. Initially the same initial spectra has been considered.

The results of the method, for a single macroparticle spectrum, are shown in Fig. 6.2. Differently from the result from the method without convolution shown in Fig. 6.1, in this case the minimum energy is the same of the pre-reconnection spectrum. The normalization of the macroparticle spectrum is ensured by the energy normalization as in Sec. 6.4.2.1 and the fration f_E is not overcome.
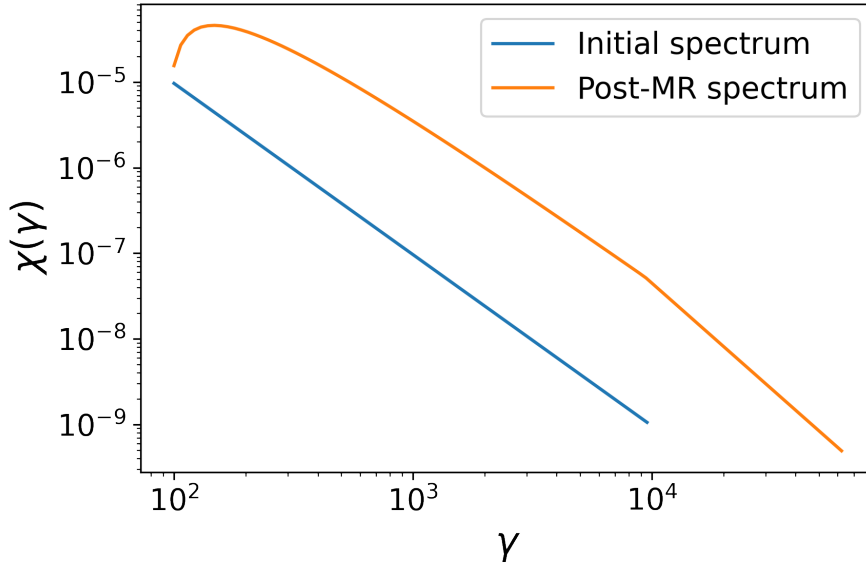
Figure 6.3: Result of the acceleration of a single macroparticle's spectrum due to magnetic reconnection with the convolution method, as described in Sec. 6.4. Case of a convolution with the result of a previous reconnection event, with the creation of a broken power-law spectrum.

The method has been tested also with an initial spectra of macroparticles with power-law index $p = 2$, with $\gamma_{\min} = 10^2$ and $\gamma_{\max} = 10^4$. This setup wants to mimic an initial spectrum that has previously developed some power-law behaviour in a MR event and, due to following radiative losses, has decreased its maximum energy.

The result for this second setup is shown in Fig. 6.3. It is possible to see that in this case, due to the different power-law behaviour of the initial spectrum, the result of the convolution is a spectrum with a broken-law behaviour. Differently from the previous proposed method this one is able to keep track of the shape of the pre-acceleration spectrum.

6.5 3D unstable plasma column

6.5.1 Numerical setup

I now study a 3D plasma column threaded by an helical magnetic field and unstable to current–driven kink mode. I have already studied this setup in Sec. 5.2.2, motivated by the instabilities analysis done in Bodo et al. (2013) that found the parameter space that lead to the development of kink instabilities.

The investigation of Sec. 5.2.2 was focused on sampling σ_p and β_p values. In the early

phase of development of the instabilities I found high values of $\sigma_p \geq 10$ and low of $\beta_p \lesssim 10^{-3}$. Such values are compatible with a regime of ultra-relativistic reconnection, when the power-law index evaluated with the sampled values and Eq. (3.16) reaches the asymptotic values $p \sim 1.9$ and the reconnection is more powerful. When the kink instabilities is finally developed, the plasma column approaches a condition of equipartition, with lower σ_p values $\sim 1-2$ and higher $\beta_p \sim 10^{-2}$. In this second time the plasma conditions still allow an efficient reconnection and eventually accelerate again the particles in the system.

I chose similarly to the previous chapter $\sigma_{\rm h} = 10$. The initial values of density ρ_0 and pressure p_0 are uniform, with $p_0 = 0.01\rho_0 c^2$ in order to have a cold jet. Following Bodo et al. (2021) we choose $P_{\rm c}/a = 1.332$ to guarantee a fast growth of the instabilities and efficient dissipation. For simplicity, the numerical simulations are performed in a frame in which the jet plasma is not moving ($v_{\rm z} = 0$). As the jet is highly magnetized, it is necessary to solve the relativistic MHD equations (Sec. 2.4).

The macroparticles are located at $t = 0$ as described in Sec. 5.2.2. In order to be able to identify at any time during the simulation which macroparticles can be considered inside the plasma column, a tracer quantity has been initialized as tr $= 1$ for $r < r_{\rm j}$ at $t = 0$ and tr $= 0$ elsewhere. Additionally, for this setup and in order to study the spectra evolution during magnetic reconnection, I have to initialize the spectra of macroparticles. Each macroparticle is generated at $t = 0$ with a steep power-law with index $p = 7$ and spanning from $\gamma_{\rm min} = 5 \times 10^2$ to $\gamma_{\rm max} = 5 \times 10^3$. These initial spectra inject energy in the macroparticles that can be increased by the acceleration processes during the reconnection and have a steep power-law that is going to be negligible with respect to the spectra generated by acceleration, similarly to what has been done in Sec. 6.3 and 6.4.

The computational box and boundary conditions are defined as in Sec. 5.2.2.

The normalization units are chosen as follow. The unit of length is set to $\hat{l} = 100\,\mathrm{pc}$, the velocity is set to $\hat{v} = c$ speed of light and as a consequence the unit of time in the simulation is $\hat{t} \simeq 236\,\mathrm{yrs}$. The unit for magnetic field results as $\hat{B} \simeq 1.37\,\mathrm{mG}$.

6.5.2 Results for the convolution method

Results for the 3D unstable plasma column setup are presented for two different times, $t = 50$ and $t = 100$, that I have already analyzed for this setup in Sec. 5.2.2 when presenting the sampling algorithm. They correspond respectively to the first stages of the development of the instabilities, when σ_p sampled values are still in the ultra-relativistic regime and to a situation more close to equipartition, with σ_p peak of the
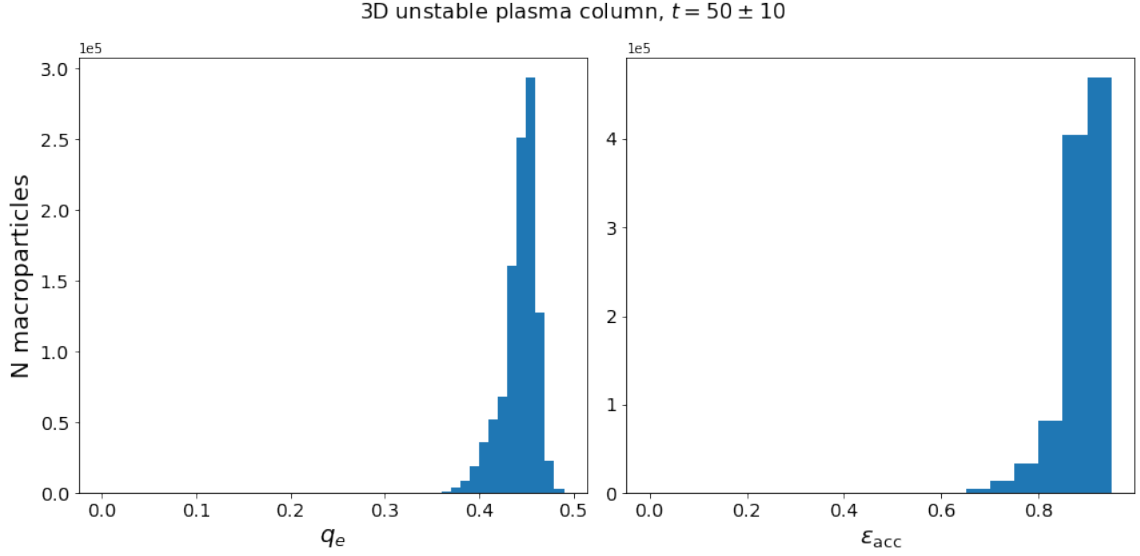
3D unstable plasma column, $t = 50 \pm 10$

Figure 6.4: Distributions of the fraction of energy going to the electron population q_e (Eq. 3.15, left panel) and acceleration efficiency ϵ_{acc} (Eq. 3.19, right panel) at $t = 50 \pm 10$ for the 3D unstable plasma column.

sampled distribution approaching $\sim 1 - 2$. The data analyzed refers respectively to $t = 50 \pm 10$ and $t = 100 \pm 10$, taking into account macroparticles that entered a reconnection site during these time intervals of the simulation.

6.5.2.1 Electron energy gained ratio and acceleration efficiency distributions

I study the fraction of available energy going to the electron population q_e (Eq. 3.15) and the acceleration efficiency ϵ_{acc} (Eq. 3.19). These two parameters allow to have an indication of the amount of the available energy that effectively goes to the macroparticles. Additionally, if $q_e \simeq 0.5$, this could be interpreted as an hint that at that time in the simulation also the proton population could be accelerated efficiently by MR.

The distributions at $t = 50 \pm 10$ are shown in Fig. 6.4. As consequence of the sampled σ_p and β_p values both q_e and ϵ_{acc} approach their saturation values. q_e shows a peak around $q_e \sim 0.45$, meaning that the energy is almost perfectly distributed between electron and proton populations. Similarly the ϵ_{acc} distribution peaks at $\epsilon_{\text{acc}} \sim 0.9$. Almost all the energy available to the electron population goes into the non-thermal component, contributing to the development of the power-law.

The distributions for $t = 100 \pm 10$ are shown in Fig. 6.5. As described the reconnection regions that I find at this second time are less powerful (meaning that σ_p values are
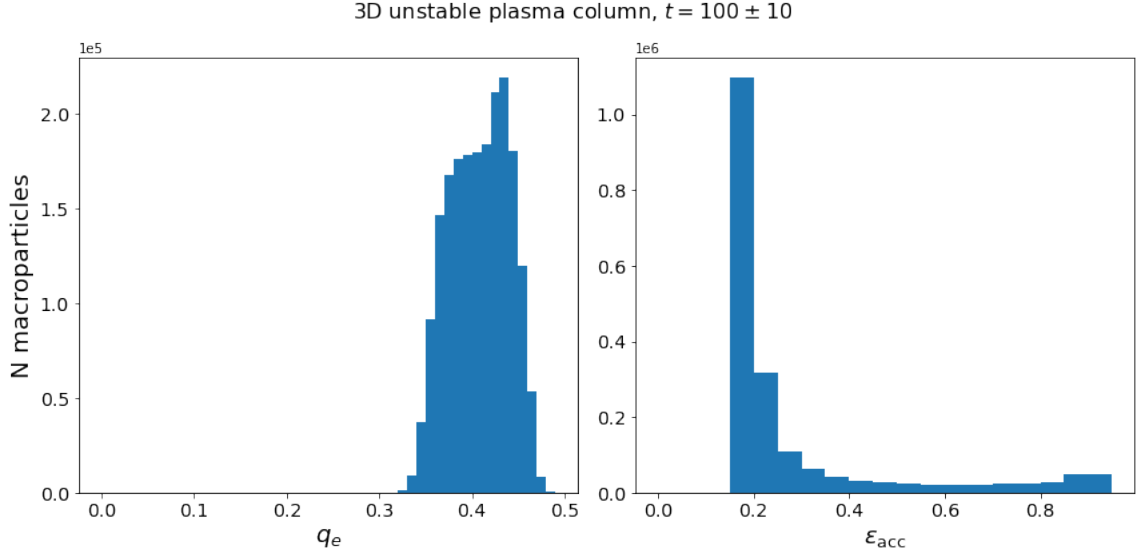
Figure 6.5: Same distributions as in Fig. 6.4 for $t = 100 \pm 10$

lower and β_p are higher). This is reflected in the q_e and ϵ_{acc} distributions. While q_e shifts towards only slightly lower values, with the majority of the values around $q_e \sim 0.4$, ϵ_{acc} is greatly sensitive when the values of β_p increase over $\beta_p \gg 3 \times 10^{-3}$. With most of the sampled values $\beta_p \gg 3 \times 10^{-3}$ the peak of the distribution drastically shifts to lower value of acceleration efficiency, with the peak found at $\epsilon_{\mathrm{acc}} \sim 0.2$. For this second time, due to the higher values of β_p distribution, while the percentage of energy available for the electron population q_e does not drastically decrease, the energy goes mostly to the thermal component, determining as a result of a MR event mostly an increase of temperature and reducing the amount of energy that can form a power-law spectrum in the non-thermal population.

6.5.2.2 Reconnecting magnetic energy $E_{B,r}$

In order to better understand the behaviour of all the components that participate to the computation of the available energy for the macroparticles spectra update δ_ϵ I analyze how the evaluation of the magnetic field component locally parallel to the current sheet, described in Sec. 6.2, impacts the amount of magnetic energy available. I compute the percentage of magnetic field energy that is used in the evaluation of the available energy with respect to the magnetic energy evaluated with the magnetic field before the subtraction of the component perpendicular to the current sheet locally. The results for $t = 50 \pm 10$ and $t = 100 \pm 10$ are shown in Figs. 6.6 and 6.7 respectively. Both the distributions are similar. The peaks of the distributions are
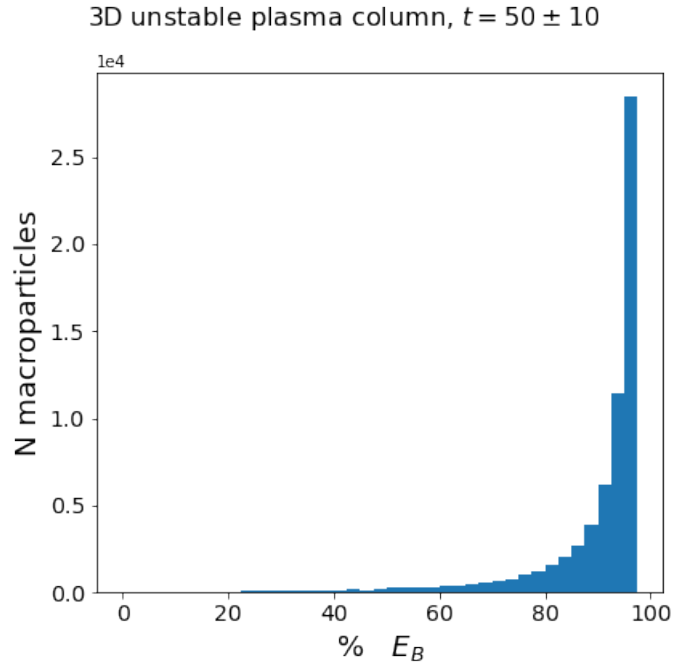
Figure 6.6: Distribution of the percentage E_B, magnetic energy evaluated with the magnetic field sampled by macroparticles (Sec. 6.2), with respect to $E_{B,r}$, estimated with only the component of the sampled magnetic field locally parallel to the current sheet. The distribution shows the results at $t = 50 \pm 10$
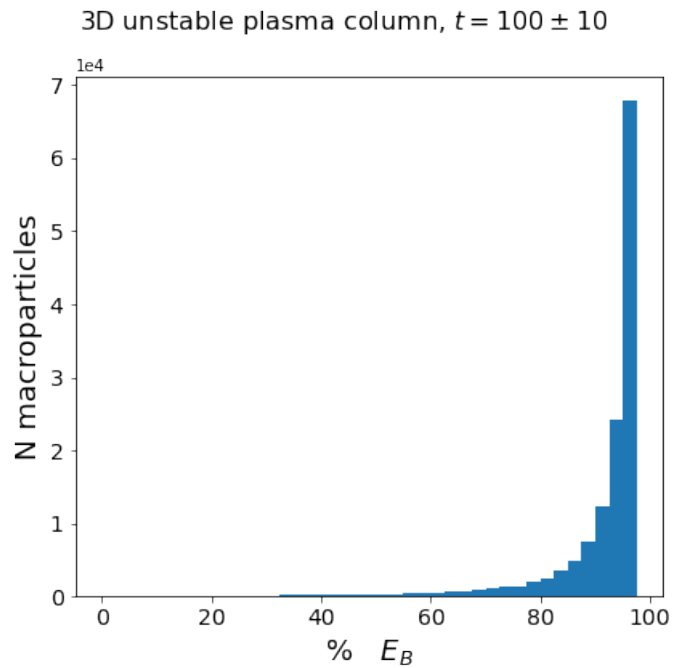

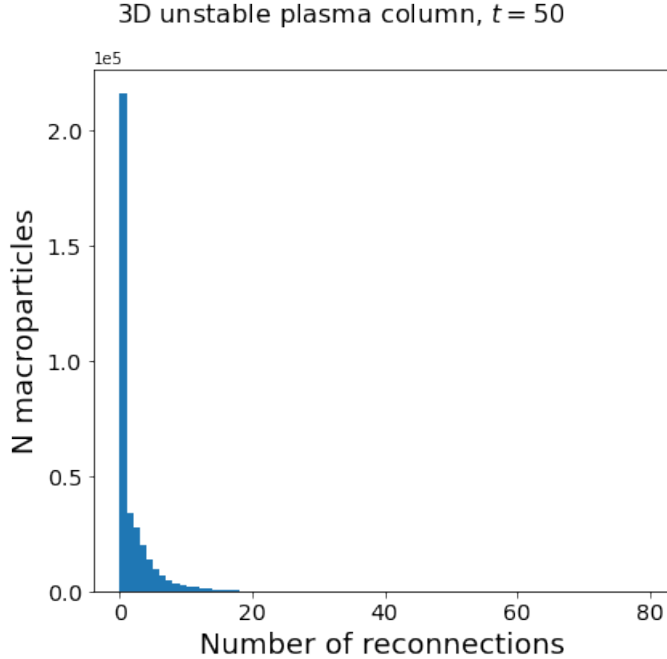Figure 6.7: Same distribution as in Fig. 6.6 for $t = 100 \pm 10$.

Figure 6.8: Distribution of the number of reconnection events experienced by the macroparticles in the 3D unstable plasma column simulation at $t = 50$.

close to 100%, meaning that in most of the cases the structure of the magnetic field around the reconnection regions is parallel to the current sheet and only a small fraction is subtracted from the sampled magnetic field. This behaviour appear the same for both times despite at $t = 100$ the structure of the plasma column is heavily disrupted by the development of the instabilities (see Fig. 5.6).

6.5.2.3 Number of reconnection events and energy comparison

I then analyze how many times the macroparticles experience an acceleration event due to magnetic reconnection and how are normalized the resulting spectra.

The results for the number of reconnection events, n_{rec}, are shown in Figs. 6.8 for $t = 50$ and 6.9 for $t = 100$.

At $t = 50$ most of the macroparticles did not experience any acceleration event and only a small fraction of them has been accelerated due to MR. The distribution has a peak at $n_{\mathrm{rec}} = 0$ and a long tail. Even if the macroparticles that experienced one or more acceleration events are a small fraction, a population of them that undergone to numerous reconnection events is present.

The situation drastically change at later times. At $t = 100$ the distribution shown in Fig. 6.9 has a peak at $n_{\mathrm{rec}} \sim 5$. A small fraction of particles did not enter any
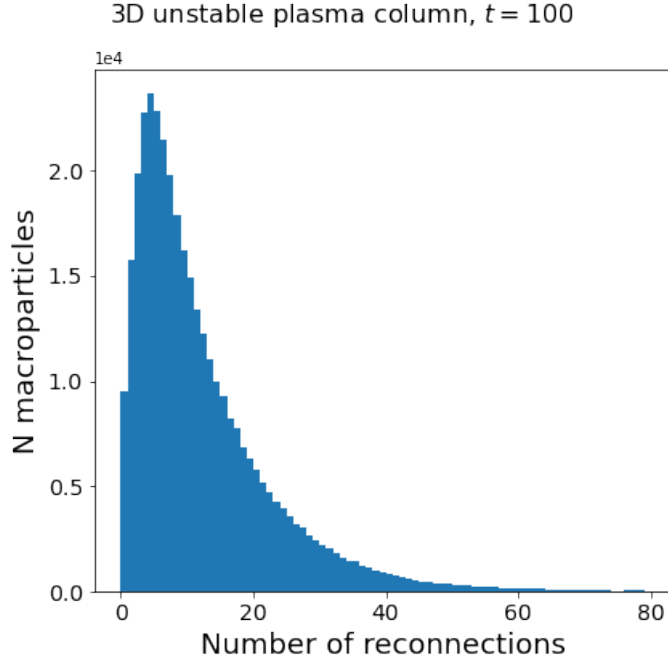
Figure 6.9: Same distribution as in Fig. 6.8 for $t = 100$.

reconnection region, but most of the macroparticles present in the system experienced multiple reconnection events. The long tail present in the distribution shows that a fraction of macroparticles has repetitively enter and exited a reconnection region.

I then compare the energy assigned to the macroparticles δ_ϵ (Eq. 6.12) with the fraction of the internal fluid energy determined by f_E. The comparison is useful to know in how many MR events the macroparticles have a significant fraction ($f_E > 0.1$) with respect to the thermal component represented by the fluid.

The results as function of time along the simulation are shown in Fig. 6.10. The blue line represents the number of events in which $\delta_\epsilon < f_E \rho \epsilon$, while the orange line the opposite case, $\delta_\epsilon \geq f_E \rho \epsilon$.

Around $t \simeq 40$ macroparticles start to experience the first reconnection events. The values of σ_p and β_p in the simulation are in the regime of ultra-relativistic reconnection and the magnetic energy available for the macroparticles is the highest one along the simulation. For this reason until $t \simeq 60$ all the events have $\delta_\epsilon \geq f_E \rho \epsilon$. While the instability evolves, the sampled values σ_p decrease going towards the equipartition of the system, as studied in detail in Sec. 5.2.2. From $t \simeq 60$ a fraction of the total reconnection events starts to have $\delta_\epsilon < f_E \rho \epsilon$. This fraction increases with time, caused by the diminution of σ_p during the development of the instability, but remains a small fraction for the entire simulation.
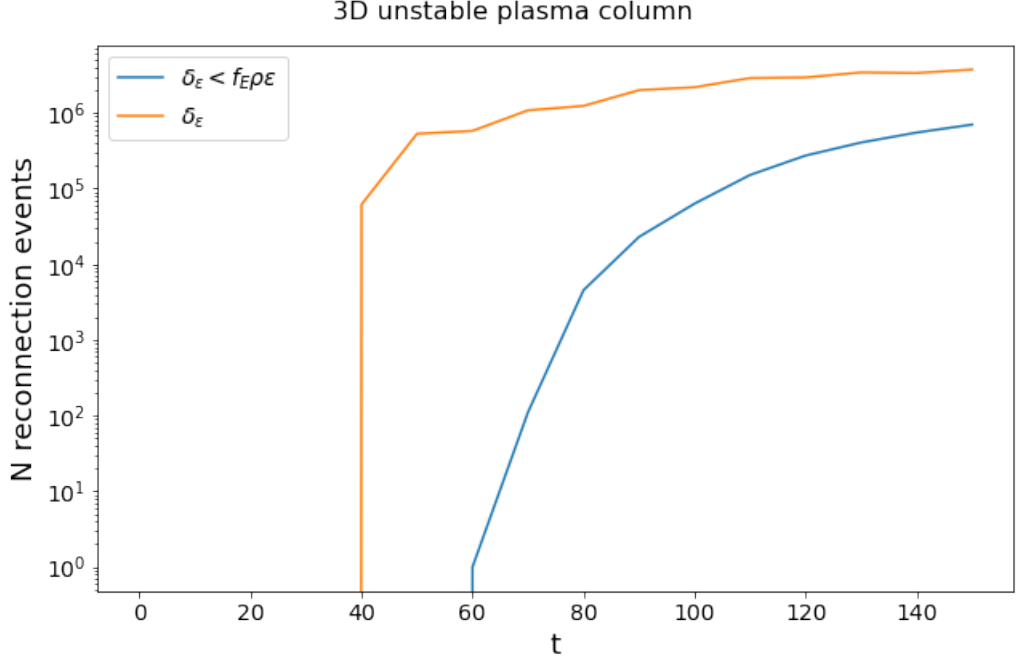
Figure 6.10: Comparison between the number of MR events in which $\delta_\epsilon < f_E \rho \epsilon$ (blue line) and $\delta_\epsilon \geq f_E \rho \epsilon$ (orange line) as a function of time in the 3D unstable plasma column simulation.

During all the simulation no event was normalized using the restriction on the fraction of particles number density with respect to the fluid one (Sec. 6.4.2.2). This would have been imposed a restriction on obtaining realistic normalizations for the final spectra.

6.5.2.4 Individual macroparticles properties

I then focus on how single macroparticles evolve during the entire simulation.
Fig. 6.11 shows the temporal evolution of the spectrum of a single macroparticle with $n_{\rm rec} = 2$, where $n_{\rm rec}$ represents the number of reconnection events that the macroparticles experienced at the end of the simulation at $t = 150$. The red line in the plot represents as a reference a power-law $f(\gamma) \propto \gamma^{-p}$ with $p = 2$. At $t \simeq 80$ the macroparticle undergoes the first strong reconnection event. The spectra reaches $\gamma_{\rm max} \sim 10^5$ and shows a power-law index $p \simeq 2$. At $t = 110$ it is possible to notice that the spectrum, of which the high energy component is decreased due to radiative losses that happened outside the current sheet, is expressed now as a broken power-law, with a clear break at $\gamma \simeq 10^4$. Due to the evolution of the σ_p and β_p distributions during the development of the instabilities, the second reconnection event produces

Figure 6.11: Temporal evolution of a single macroparticle spectrum with $n_{rec} = 2$ in the 3D unstable plasma column simulation. Different times during the simulation are labeled in the legend. As a reference a power-law $f(\gamma) \propto \gamma^{-p}$ with $p = 2$ is represented as red line.
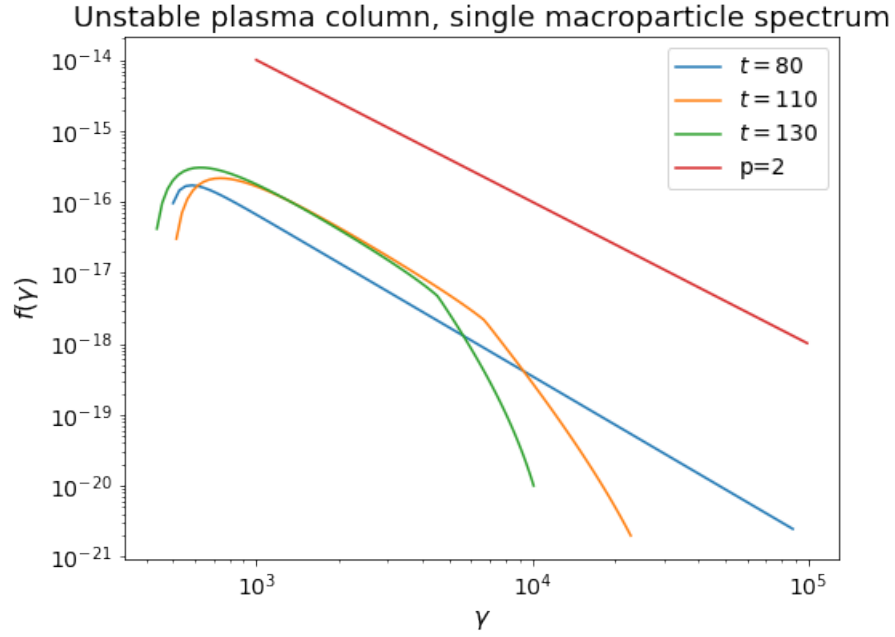

Figure 6.12: Temporal evolution of a single macroparticle spectrum with with $n_{rec} = 5$ in the 3D unstable plasma column simulation. Different times during the simulation are labeled in the legend. As a reference a power-law $f(\gamma) \propto \gamma^{-p}$ with $p = 2$ is represented as red line.
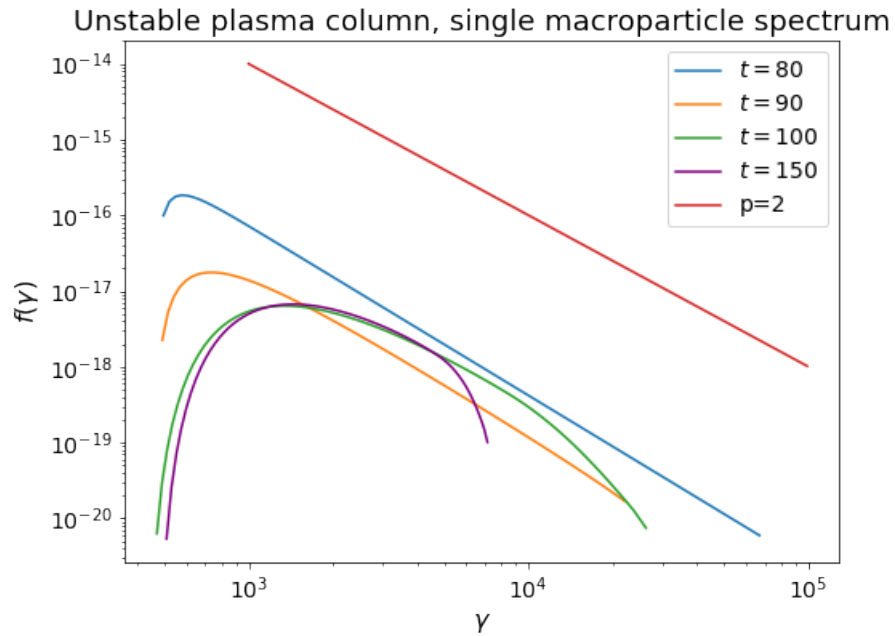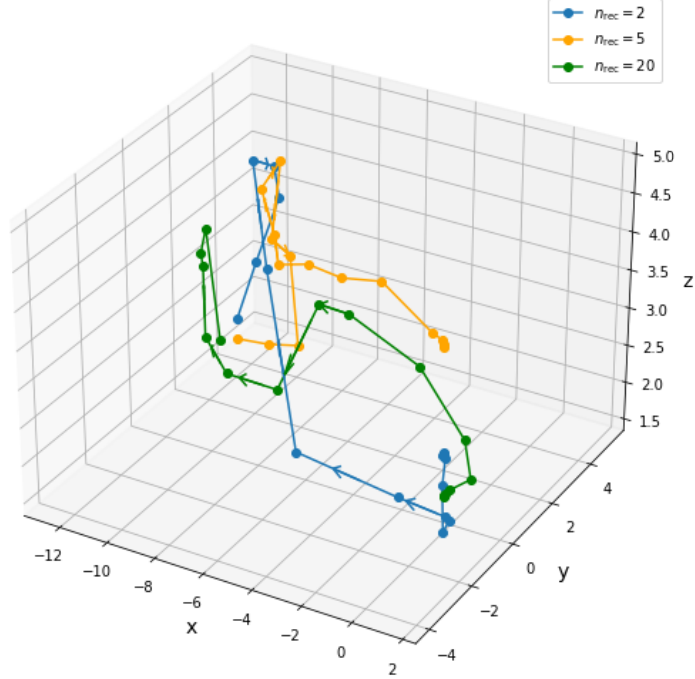
Figure 6.13: Trajectories of three representative macroparticles during the simulation, experiencing different number of reconnection events, as represented in the legend. Arrows in each different lines represent the direction of the temporal evolution of their trajectory. Points on the same trajectory represent the macroparticles position from $t = 0$ to $t = 150$, with time steps $\Delta t = 10$.

a much steeper power-law, reaching at the same time lower maximum energies with respect to the first acceleration. Finally at $t = 130$ the spectrum, without any further acceleration, keep decreasing its maximum energy through radiation processes.

In Fig. 6.11 another macroparticle with $n_{\text{rec}} = 5$ at $t = 150$, close to the peak of the n_{rec} distribution of Fig. 6.9, is represented. It is possible to observe that the spectrum after the first acceleration happened at $t \simeq 80$ is quite similar to the result obtained for the first macroparticle analyzed (Fig. 6.11), while a second subsequent acceleration at $t \simeq 90$ keeps a similar power-law behaviour, but the diminution of σ_p does not allow the macroparticle to reach the same maximum energy as the previous acceleration event. Similarly to the first case, the further accelerations are not as powerful as the first one and the maximum energy keep decreasing.

It is possible to follow also the position of the macroparticles during the temporal evolution of the unstable plasma column. This can be particularly interesting for macroparticles that experience the higher numbers of reconnection events at that eventually could have been trapped in some specific region of the column. To check if this is the case in Fig. 6.13 I present the trajectory for three representative macroparticles respectively with $n_{\mathrm{rec}} = 2$, 5 and 20. The macroparticles with $n_{\mathrm{rec}} = 2$ and 5 are the same for which the spectral evolution is represented respectively in Figs. 6.11 and 6.12. The points on the same trajectory represent the macroparticles position with time steps $\Delta t = 10$. The arrows in each trajectory represent the direction of the temporal evolution, from $t = 0$ to $t = 150$.

Despite of the different n_{rec} for the three macroparticles their trajectories follow a similar pattern. Despite of my initial concern, this constitutes an evidence that macroparticles experiencing more reconnection events do not remain trapped in the same region of the plasma column. In the first few points $t \lesssim 50$ the macroparticles are still located at small radii, due to the instabilities still not being able to strongly deform the plasma column. At $t \simeq 50$, due to the development of the instabilities, the macroparticles are moved towards higher radii along with the deformed column. This is the moment in which the macroparticles with $n_{\mathrm{rec}} = 2$ and 5 experiences their first reconnection event (see Figs. 6.11 and 6.12). Finally at the end of the simulation, while the plasma column is heavily deformed, the particles are scattered by these deformations and they can eventually incur on further reconnection events.

6.5.2.5 Collective macroparticles properties

I finally study the collective behaviour of macroparticles spectra at $t = 50$ and $t = 100$. I consider for both the cases all the macroparticles that are located in computational cells part of the plasma column. I use the tracer defined in the setup (Sec. 6.5) to select macroparticles that are located at values $\mathrm{tr} \geq 0.4$. The lower value of the tracer with respect to the initial one defined at $t = 0$, when for $r < r_{\mathrm{j}}$ the tracer value has been set as $\mathrm{tr} = 1$, is due to the development of instabilities. The values of the tracer lower while the plasma column is deformed, as shown in Bodo et al. (2021). I also excluded macroparticles that did not experience any reconnection event, in order to minimize the impact of the choice of their initial spectra at $t = 0$.

The cumulative spectrum of the selected macroparticles for $t = 50$ is shown in Fig. 6.14. Similarly to the behaviour of the individual macroparticles I have previously analyzed (Figs. 6.11 and 6.12) also in the cumulative spectrum a power-law with index $p \simeq 2$ is observed (the orange line in Fig. 6.14 represents as a reference a

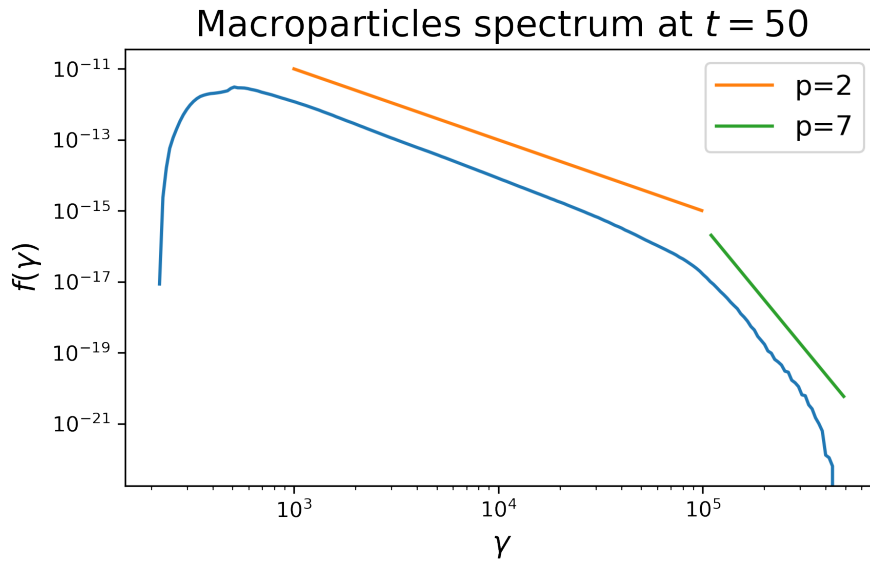Figure 6.14: Cumulative spectrum of macroparticles in computational cells with values of the column tracer $tr \geq 0.4$ (see description in Sec. 6.5) at $t = 50$. As a reference, power-laws with different indices are plot as shown in the legend.
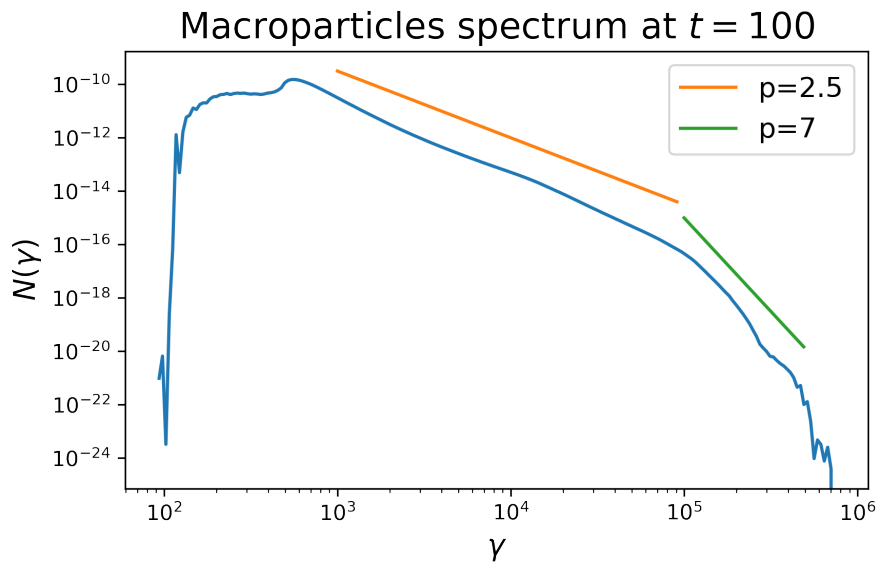

Figure 6.15: Cumulative spectrum of macroparticles selected as in Fig. 6.14 at $t = 100$. As a reference, power-laws with different indices are plot as shown in the legend.

power-law with $p = 2$). An high-energy cut-off is present at energies $\gamma \gtrsim 10^5$ that seems well represented by a power-law with index $p \simeq 7$ (green line as a reference for a power-law with $p = 7$).

The cumulative spectrum at $t = 100$ is shown in Fig. 6.15. With respect to $t = 50$ up to $\gamma \simeq 10^5$ the spectrum is steeper, with a power-law of $p \simeq 2.5$ (the orange line represents as a reference a power-law with $p = 2.5$), mainly due to the lower σ_p and higher β_p values sampled at this time.

6.6   Conclusions

In this Chapter two new strategies to update post-MR spectra in R(MHD) simulation are introduced. Based on the algorithms to identify current sheets of Chap. 4 and to sample of the chief parameters for MR of Chap. 5 it has been possible firstly to describe a simple model to evaluate the post-MR spectra based on the previous energy of the macroparticles, but insensitive to the previous shape of spectra. The update strategy has then been refined with a second algorithm able to take into account multiple macroparticles in the same cell at the time of the update and the previous shape of the spectra entering in the reconnection region.

The new algorithms have been tested in a steady state reconnection region to validate them and then applied to the case of a 3D unstable plasma column undergoing the development of Kink instabilities. Motivated by the promising results on the σ_p and β_p distributions found in Sec. 5.2.2, I found that during the development of the instabilities the macroparticles are able to be accelerated by ultra-relativistic episodes of MR and further acceleration can take place at later time, even with the development of broken power-law spectra. The spectra update allows to study individually how single macroparticles spectra evolves in astrophysical setups in which MR is present as well as their collective properties.

7
Conclusions

7.1 Summary

Understanding how particles are accelerated to non-thermal energies in astrophysical environments is an important challenge in modern astrophysics. Many progresses have been done in the studies of the acceleration processes with numerical simulations at the kinetic level (PIC simulations). In particular, due to the power-law spectra obtained as a result of the MR, it has been extensively investigated and it appears to be a promising phenomenon able to explain open problems coming from observations (Sec. 1.1.2).

After a general introduction presenting the main motivations to study MR in large scale simulations (Chap. 1) I summarized the main achievements of theoretical and numerical works on MR (Chap. 3), with particular focus on the results concerning the description of the non-thermal particle acceleration. The main plasma parameters required to model the post-MR electrons spectra have been introduced. With the prescriptions obtained from PIC results, it is possible to build a sub-grid model to overcome the multiscale problem. First I have presented a new method to identify current sheets in (R)MHD simulations (Chap. 4), implemented in the PLUTO code (Mignone et al. 2007). With respect to previous investigations, the novelty of the algorithm, for the identification of reconnection sites, is the improved computational efficiency in large scale simulations, and its capability of recognizing current sheets in complex 2D and 3D geometries. I have tested the method in the cases of a single

current sheet, a slab jet and a 3D unstable plasma column, demonstrating the effectiveness of the proposed method. With respect to the particle acceleration process, a limitation of the algorithm for the identification of current sheets is that, in this form, it does not directly provide a way to determine the spatial extension of the current sheets, contrary to the method proposed by Zhdankin et al. (2013). This could be particularly critical if the dimensions of the reconnection sites prove to be a relevant parameter for the acceleration process (see e.g. Sironi et al. 2016).

Then I have presented a new algorithm able to sample, for macroparticles that enter the MR sites identified with the previous method, the main parameters of the sub-grid model, the magnetization σ and the β plasma parameter (Chap. 5). Such a sampling has been performed in both the 2D and 3D simulations introduced before and the distributions of such parameters have been inferred. A limitation of the sampling algorithm presented is that the estimate of the magnetization does not take into account the possible presence of a guide field. A strong guide field can have a disrupting effect on the efficiency of the acceleration and the final spectrum of non-thermal particles (see e.g. Werner & Uzdensky 2017, and Sec. 3.2.2.3). It is possible to overcome this limitation by using the method that has been introduced in Sec. 4.1.1 to estimate the guide field. However a study of the dependence of the final spectra depending on both σ and β is needed, since a guide field can also affect the predicted power-law index (Werner & Uzdensky 2017).

Finally the complete sub-grid model for the spectra update due to acceleration in a current sheet has been presented (Chap. 6). Two different strategies for the update are introduced, with the second one, a convoluted method taking into account energy of the previous spectrum and the energy gained through MR, together with the shape of the pre-reconnection spectrum and the presence of multiple macroparticles in the same cell, promising to study the impact of MR and the energetic in (R)MHD simulations. The method has been applied to the simulation of a 3D unstable plasma column, studying the distributions of the main quantities derived from the sampled σ and β parameters and studying the individual and collective behaviour of macroparticles spectra.

7.2 Future work

Understanding the complex physics of high-energy astrophysics is one of the most compelling challenges in astrophysics.

I have developed a modular framework in (R)MHD simulations that is both versatile and expansible with new features. Such framework has been developed with an eye to the comparison between MR and DSA, made possible by the implementation, with a similar phylosophy of a sub-grid model also for DSA (Vaidya et al. 2018; Mukherjee et al. 2021). It can be applied to study MR impact in different (R)MHD simulations of extra-galactic sources. Furthermore, there is still space for expanding the functionalities and for optimizating the module.

Some of the foreseen directions in which the work can be extended are the following:

– Implementation of the feedback - Feedback between the thermal component described by MHD equations and the non-thermal population represented by the macroparticles can be added to the module, allowing a proper comparison between energy gained by the non-thermal population during DSA and MR acceleration processes. In Chap. 6 the energy gain associated to the macroparticles in the convoluted method is used to normalize the final spectra. A possible limitation on the energy injected in the post-MR spectra is given by the definition of a fraction f_N of the fluid number density at macroparticle's position that macroparticles spectra can not overcome. Additionally, with ultra-relativistic reconnection events, the amount of magnetic energy that is converted can have a significant impact on the subsequent plasma evolution when adding the feedback. The implementation of a feedback would require to understand, for each macroparticle undergoing MR, in which computational cell the energy injected in post-MR spectra has to be subtracted from the fluid magnetic energy. Furthermore the method described for the convoluted method estimates the magnetic energy available for all the macroparticles present in the same computational cell, careless of the possible different paths with which the macroparticles entered the reconnection region. The evaluation of the feedback would require a refinement of this strategy, requiring a more sophisticated treatment for the estimate of the available energy in presence of multiple macroparticles.

– Application to blazar variability - Using the module on MHD jet simulations it is possible to study the temporal evolution of MR, its generated spectra (as presented in Chap. 6), relevance and the appearance of powerful regions in simulations that may generate powerful fast flares observed in blazars. A possible limitation can be posed by the computational timestep considered in the simulations presented in this thesis, that can be comparable or even bigger with respect to the timescale of typical variability. The problem is more evident

when considering fast flares. A possible treatment for this problem is to let the setup develop up to a desired time (e.g. full development of instabilities for the unstable plasma column) as already done in this work and then to study with higher time resolution the plasma conditions in which fast flares may happen. The combination of time and spatial resolution may allow to investigate σ and β parameters during this phase and to focus on regions with conditions more favorable to ultra-relativistic reconnection where it is then possible to explore the possibility to have macroparticles populations freshly accelerated by this reconnection events.

— Comparison between shocks and magnetic reconnection - Comparison between DSA and MR acceleration can be performed with spatial and time resolution, comparing final spectra for the two acceleration methods. Making the comparison feasible requires to solve the problem of what happens when a computational cell is identified both as a reconnection site and as a shock. Shocks due to the interaction between a jet and the external medium, for example, may deform the magnetic field and generate reconnection region. Additionally large simulations focused on DSA and on MR consider often different initial condition more favorable to one of the two acceleration methods (e.g. high σ for MR).

— Magnetic reconnection applied to protons - In order to investigate the role of the most powerful MR regions in accelerating protons to non-thermal energies the implementation of macroparticles can be extended to protons population. For high-σ regions the differences on the details on the final spectra between electrons and protons become negligible and with the implementation of the transport equation for protons a similar approach to study proton spectra produced by MR can be applied. The algorithm implemented in order to identify the MR regions (Chap. 4) and to sample σ and β (Chap. 5) can be naturally extended to a second non-thermal population made of protons. The introduction of the non-thermal proton population would require to duplicate the structure describing the electron population and to adapt the coefficients regarding the radiative losses for protons. The spectral update can be achieved with a similar strategy and applied only for the most powerful reconnection region.

— Magnetic reconnection in GRBs - GRBs may have a Poyting-flux dominated jet, with high values of σ. MR in moderate to high σ regime may be in this case the mechanism that accelerate particles. Different models for MR production of

the prompt emission in GRBs are proposed (Beniamini & Giannios 2017; Zhang & Yan 2010). The GRB central engine launches an intermittent magnetically dominated wind. It is expected that in the GRB emission region the plasma is moderately magnetized, with σ values ($1 \lesssim \sigma \lesssim 100$) that could produce powerful MR events. Internal collision between different shells in the ejecta may distort the ordered magnetic field. MHD simulations of such a situation have been performed (Deng et al. 2015) and the Lagrangian particles module could study in details the spectra produced in such configuration.

Bibliography

Aartsen, M., Ackermann, M., Adams, J., et al. 2018, Science, 361

Aartsen, M. G., Ackermann, M., Adams, J., et al. 2020, Phys. Rev. Lett., 124, 051103

Abbasi, R., Ackermann, M., Adams, J., et al. 2022, Science, 378, 538

Abdollahi, S., Ackermann, M., Ajello, M., et al. 2017, Physical Review D, 95

Abeysekara, A. U., Alfaro, R., Alvarez, C., et al. 2019, The Astrophysical Journal, 871, 96

Achterberg, A., Gallant, Y. A., Kirk, J. G., & Guthmann, A. W. 2001, Monthly Notices of the Royal Astronomical Society, 328, 393

Ackermann, M., Ajello, M., Allafort, A., et al. 2013, Science, 339, 807

Adriani, O., Barbarino, G. C., Bazilevskaya, G. A., et al. 2011, Science, 332, 69

Aguilar, M., Aisa, D., Alpat, B., et al. 2015, Phys. Rev. Lett., 114, 171103

Aguilar, M., Cavasonza, L. A., Alpat, B., et al. 2019, Physical Review Letters, 122

Aharonian, F., Akhperjanian, A. G., Bazer-Bachi, A. R., et al. 2007a, The Astrophysical Journal, 664, L71

Aharonian, F., Akhperjanian, A. G., Bazer-Bachi, A. R., et al. 2007b, Phys. Rev. D, 75, 042004

Albert, A., Alves, S., André, M., et al. 2022, The Astrophysical Journal, 934, 164

Aloisio, R., Berezinsky, V., & Gazizov, A. 2012, Astroparticle Physics, 39-40, 129

Alves, E., Zrake, J., & Fiuza, F. 2018, Physical Review Letters, 121

Archer, A., Benbow, W., Bird, R., et al. 2018, Phys. Rev. D, 98, 022009

Atkins, R., Benbow, W., Berley, D., et al. 2004, The Astrophysical Journal, 608, 680

Axford, W. I., Leer, E., & Skadron, G. 1977, in International Cosmic Ray Conference, Vol. 11, International Cosmic Ray Conference, 132

Ball, D., Sironi, L., & Özel, F. 2018, The Astrophysical Journal, 862, 80

Ballard, K. R. & Heavens, A. F. 1991, Monthly Notices of the Royal Astronomical Society, 251, 438

Bárta, M., Büchner, J., Karlický, M., & Skála, J. 2011, The Astrophysical Journal, 737, 24

Bell, A. R. 1978, Monthly Notices of the Royal Astronomical Society, 182, 147

Beniamini, P. & Giannios, D. 2017, Monthly Notices of the Royal Astronomical Society, 468, 3202

Blandford, R. D. & Ostriker, J. P. 1978, The Astrophysical Journal, 221, L29

Blandford, R. D. & Payne, D. G. 1982, Monthly Notices of the Royal Astronomical Society, 199, 883

Blandford, R. D. & Znajek, R. L. 1977, Monthly Notices of the Royal Astronomical Society, 179, 433

Bodo, G., Mamatsashvili, G., Rossi, P., & Mignone, A. 2013, MNRAS, 434, 3030

Bodo, G., Mamatsashvili, G., Rossi, P., & Mignone, A. 2021, Monthly Notices of the Royal Astronomical Society, 510, 2391

Bodo, G., Tavecchio, F., & Sironi, L. 2021, MNRAS, 501, 2836

Bromberg, O., Singh, C. B., Davelaar, J., & Philippov, A. A. 2019, The Astrophysical Journal, 884, 39

Cerutti, B., Philippov, A. A., & Dubus, G. 2020, Astronomy & Astrophysics, 642, A204

Cerutti, B., Werner, G. R., Uzdensky, D. A., & Begelman, M. C. 2014, Physics of Plasmas, 21, 056501

Chiuderi, C. & Velli, M. 2014, in UNITEXT for Physics (Springer Milan), 203–227

Coppi, B., Galvao, R., Pellat, R., Rosenbluth, M., & Rutherford, P. 1976, Soviet Journal of Plasma Physics, 2, 533

Davelaar, J., Philippov, A. A., Bromberg, O., & Singh, C. B. 2020, The Astrophysical Journal, 896, L31

Deng, W., Li, H., Zhang, B., & Li, S. 2015, The Astrophysical Journal, 805, 163

Dere, K. P. 1996, ApJ, 472, 864

Drury, L. O. 1983, Reports on Progress in Physics, 46, 973

Egedal, J., Katz, N., Bonde, J., et al. 2011, Physics of Plasmas, 18, 111203

Fermi, E. 1949, Physical Review, 75, 1169

Fermi, E. 1954, The Astrophysical Journal, 119, 1

Furth, H. P., Killeen, J., & Rosenbluth, M. N. 1963, Physics of Fluids, 6, 459

Gary, D. E., Chen, B., Dennis, B. R., et al. 2018, The Astrophysical Journal, 863, 83

Giannios, D. 2013, Monthly Notices of the Royal Astronomical Society, 431, 355

Giannios, D., Uzdensky, D. A., & Begelman, M. C. 2009, Monthly Notices of the Royal Astronomical Society: Letters, 395, L29

Greisen, K. 1966, Physical Review Letters, 16, 748

Guo, F., Li, H., Daughton, W., & Liu, Y.-H. 2014, Physical Review Letters, 113

Guo, F., Li, X., Daughton, W., et al. 2019, The Astrophysical Journal, 879, L23

Guo, F., Li, X., Li, H., et al. 2016, The Astrophysical Journal, 818, L9

Guo, F., Liu, Y.-H., Daughton, W., & Li, H. 2015, The Astrophysical Journal, 806, 167

Hess, V. F. 1912, Phys. Z., 13, 1084

Hoyle, F. 1960, Monthly Notices of the Royal Astronomical Society, 120, 338

Isobe, H., Morimoto, T., Eto, S., Narukage, N., & Shibata, K. 2002, in Multi-wavelength Observations of Coronal Structure and Dynamics, Yohkoh 10th Anniversary Meeting (Elsevier), 171–172

Jaroschek, C. H., Treumann, R. A., Lesch, H., & Scholer, M. 2004, Physics of Plasmas, 11, 1151

Ji, H., Yamada, M., Hsu, S., & Kulsrud, R. 1998, Physical Review Letters, 80, 3256

Jokipii, J. 1987, The Astrophysical Journal, 313, 842

Kadowaki, L. H. S., Pino, E. M. D. G. D., & Stone, J. M. 2018, The Astrophysical Journal, 864, 52

Kennel, C. F. & Coroniti, F. V. 1984, The Astrophysical Journal, 283, 710

Keshet, U. & Waxman, E. 2005, Phys. Rev. Lett., 94, 111102

Kilian, P., Li, X., Guo, F., & Li, H. 2020, The Astrophysical Journal, 899, 151

Kirk, J. G., Guthmann, A. W., Gallant, Y. A., & Achterberg, A. 2000, The Astrophysical Journal, 542, 235

Kirk, J. G. & Skjæraasen, O. 2003, ApJ, 591, 366

Komissarov, S. S., Barkov, M. V., Vlahakis, N., & Königl, A. 2007, Monthly Notices of the Royal Astronomical Society, 380, 51

Kormendy, J. & Richstone, D. 1995, ARA&A, 33, 581

Krucker, S. & Battaglia, M. 2013, The Astrophysical Journal, 780, 107

Krymskii, G. F. 1977, Akademiia Nauk SSSR Doklady, 234, 1306

Kumar, P. & Zhang, B. 2015, Physics Reports, 561, 1

Li, X., Guo, F., Li, H., Stanier, A., & Kilian, P. 2019, The Astrophysical Journal, 884, 118

Loureiro, N. F., Cowley, S. C., Dorland, W. D., Haines, M. G., & Schekochihin, A. A. 2005, Physical Review Letters, 95

Lyubarsky, Y. E. 2009, Monthly Notices of the Royal Astronomical Society, 402, 353

MacDonald, N. R., Jorstad, S. G., & Marscher, A. P. 2017, The Astrophysical Journal, 850, 87

Marcowith, A., Ferrand, G., Grech, M., et al. 2020, Living Reviews in Computational Astrophysics, 6

Mbarek, R., Haggerty, C., Sironi, L., Shay, M., & Caprioli, D. 2022, Phys. Rev. Lett., 128, 145101

McKinney, J. C. & Uzdensky, D. A. 2011, Monthly Notices of the Royal Astronomical Society, 419, 573

Medina-Torrejón, T. E., de Gouveia Dal Pino, E. M., Kadowaki, L. H. S., et al. 2021, The Astrophysical Journal, 908, 193

Melzani, M., Walder, R., Folini, D., Winisdoerffer, C., & Favre, J. M. 2014, Astronomy & Astrophysics, 570, A111

Mignone, A., Bodo, G., Massaglia, S., et al. 2007, The Astrophysical Journal Supplement Series, 170, 228

Mignone, A. & McKinney, J. C. 2007, Monthly Notices of the Royal Astronomical Society, 378, 1118

Mignone, A., Zanni, C., Tzeferacos, P., et al. 2012, The Astrophysical Journal Supplement Series, 198, 7

Mukherjee, D., Bodo, G., Rossi, P., Mignone, A., & Vaidya, B. 2021, Monthly Notices of the Royal Astronomical Society, 505, 2267

Nalewajko, K., Giannios, D., Begelman, M. C., Uzdensky, D. A., & Sikora, M. 2011, Monthly Notices of the Royal Astronomical Society, 413, 333

Nishikawa, K., Mizuno, Y., Gómez, J. L., et al. 2020, Monthly Notices of the Royal Astronomical Society, 493, 2652

Ortuño-Macías, J., Nalewajko, K., Uzdensky, D. A., et al. 2022, The Astrophysical Journal, 931, 137

Padovani, P., Alexander, D. M., Assef, R. J., et al. 2017, The Astronomy and Astrophysics Review, 25

Parker, E. N. 1957, Journal of Geophysical Research, 62, 509

Petropoulou, M., Giannios, D., & Sironi, L. 2016, Monthly Notices of the Royal Astronomical Society, 462, 3325

Petropoulou, M. & Sironi, L. 2018, Monthly Notices of the Royal Astronomical Society, 481, 5687

Petropoulou, M., Sironi, L., Spitkovsky, A., & Giannios, D. 2019, The Astrophysical Journal, 880, 37

Plotnikov, I., Grassi, A., & Grech, M. 2018, Monthly Notices of the Royal Astronomical Society, 477, 5238

Pontin, D. I. & Priest, E. R. 2022, Living Reviews in Solar Physics, 19

Rutherford, P. H. 1973, Physics of Fluids, 16, 1903

Servidio, S., Matthaeus, W. H., Shay, M. A., et al. 2010, Physics of Plasmas, 17, 032315

Shakura, N. I. & Sunyaev, R. A. 1973, A&A, 24, 337

Singh, C. B., Mizuno, Y., & de Gouveia Dal Pino, E. M. 2016, The Astrophysical Journal, 824, 48

Sironi, L., Giannios, D., & Petropoulou, M. 2016, MNRAS, 462, 48

Sironi, L., Petropoulou, M., & Giannios, D. 2015, Monthly Notices of the Royal Astronomical Society, 450, 183

Sironi, L. & Spitkovsky, A. 2014, The Astrophysical Journal, 783, L21

Sobacchi, E., Nättilä, J., & Sironi, L. 2021, Monthly Notices of the Royal Astronomical Society, 503, 688

Striani, E., Mignone, A., Vaidya, B., Bodo, G., & Ferrari, A. 2016, Monthly Notices of the Royal Astronomical Society, 462, 2970

Summerlin, E. J. & Baring, M. G. 2011, The Astrophysical Journal, 745, 63

Sweet, P. A. 1958, The Observatory, 78, 30

Takamoto, M. & Kirk, J. G. 2015, The Astrophysical Journal, 809, 29

Taub, A. H. 1948, Physical Review, 74, 328

Ulrich, M.-H., Maraschi, L., & Urry, C. M. 1997, Annual Review of Astronomy and Astrophysics, 35, 445

Vaidya, B., Mignone, A., Bodo, G., Rossi, P., & Massaglia, S. 2018, The Astrophysical Journal, 865, 144

Wang, F., Yang, J., Fan, X., et al. 2021, The Astrophysical Journal Letters, 907, L1

Webb, G. M. 1989, The Astrophysical Journal, 340, 1112

Werner, G. R. & Uzdensky, D. A. 2017, The Astrophysical Journal, 843, L27

Werner, G. R. & Uzdensky, D. A. 2021, Journal of Plasma Physics, 87

Werner, G. R., Uzdensky, D. A., Begelman, M. C., Cerutti, B., & Nalewajko, K. 2017, Monthly Notices of the Royal Astronomical Society, 473, 4840

Werner, G. R., Uzdensky, D. A., Cerutti, B., Nalewajko, K., & Begelman, M. C. 2015, The Astrophysical Journal, 816, L8

Zenitani, S. & Hoshino, M. 2001, The Astrophysical Journal, 562, L63

Zenitani, S. & Hoshino, M. 2005, Physical Review Letters, 95

Zenitani, S. & Hoshino, M. 2008, The Astrophysical Journal, 677, 530

Zhang, B. & Yan, H. 2010, The Astrophysical Journal, 726, 90

Zhang, H., Sironi, L., & Giannios, D. 2021, The Astrophysical Journal, 922, 261

Zhdankin, V., Uzdensky, D. A., & Boldyrev, S. 2015, The Astrophysical Journal, 811, 6

Zhdankin, V., Uzdensky, D. A., Perez, J. C., & Boldyrev, S. 2013, The Astrophysical Journal, 771, 124